Environmental Sensing Applications of Zinc Oxide Based Film Bulk Acoustic Resonator

by

Xiaotun Qiu

A Dissertation Presented in Partial Fulfillment
of the Requirements for the Degree
Doctor of Philosophy

Approved April 2011 by the
Graduate Supervisory Committee:

Hongyu Yu, Chair
Jennifer Blain Christen
James Aberle
Hanqing Jiang

ARIZONA STATE UNIVERSITY

May 2011

ABSTRACT

Different environmental factors, such as ultraviolet radiation (UV), relative humidity (RH) and the presence of reducing gases (acetone and ethanol), play an important role in the daily life of human beings. UV is very important in a number of areas, such as astronomy, resin curing of polymeric materials, combustion engineering, water purification, flame detection and biological effects with more recent proposals like early missile plume detection, secure space-to-space communications and pollution monitoring. RH is a very common parameter in the environment. It is essential not only for human comfort, but also for a broad spectrum of industries and technologies. There is a substantial interest in the development of RH sensors for applications in monitoring moisture level at home, in clean rooms, cryogenic processes, medical and food science, and so on. The concentration of acetone and other ketone bodies in the exhaled air can serve as an express noninvasive diagnosis of ketosis. Meanwhile, driving under the influence of alcohol is a serious traffic violation and this kind of deviant behavior causes many accidents and deaths on the highway. Therefore, the detection of ethanol in breath is usually used as a quick and reliable screening method for the sobriety checkpoint.

Traditionally, semiconductor metal oxide sensors are the major candidates employed in the sensing applications mentioned above. However, they suffer from the low sensitivity, poor selectivity and huge power consumption. In this dissertation, Zinc Oxide (ZnO) based Film Bulk Acoustic Resonator (FBAR) was developed to monitor UV, RH, acetone and ethanol in the environment. FBAR

generally consists of a sputtered piezoelectric thin film (ZnO/AlN) sandwiched between two electrodes. It has been well developed both as filters and as high sensitivity mass sensors in recent years. FBAR offers high sensitivity and excellent selectivity for various environment monitoring applications. As the sensing signal is in the frequency domain, FABR has the potential to be incorporated in a wireless sensor network for remote sensing. This study extended our current knowledge of FBAR and pointed out feasible directions for future exploration.

DEDICATION

To My Mother and Father

ACKNOWLEDGMENTS

I would like to express my special appreciation to my academic advisor, Dr. Hongyu Yu for providing me a chance to work on such an innovative project, which paves the way to build my dissertation. It is such a great privilege to work with him. I am also thankful to my advisory committee members, Dr. Hanqing Jiang, Dr. James Aberle, and Dr. Jennifer Blain Christen for taking interest in my work and giving valuable advice to me.

I am also indebted to Dr. Eun Sok Kim and Shih-Jui Chen for helping me to prepare ZnO films at University of Southern California. I am sincerely thankful to Dr. Shengmin Guo and Ranran Liu for all the help they provided to deposit the reactive Ni/Al nanofilms at Louisiana State University.

I am grateful to members of our group: Dr. Hua Wang, Jon Oiler, Jie Zhu, Ziyu Wang, Rui Tang, Hai Huang, Teng Ma, and Cunjiang Yu. Their help and advice are the main resources for me to overcome any difficulties. From them, I am always inspired, motivated, and encouraged. I enjoy not only working together in the same group, but also the friendship in the daily life.

I am also grateful to my parents, who give me full support on whatever decision I make throughout my life and do their best to provide me a good education at home and an opportunity to study abroad.

Finally, I want to thank all my friends at Arizona State University, University of Southern California, Louisiana State University and Tsinghua University, for their moral and technical support, without which I would not have succeeded in finishing my study.

TABLE OF CONTENTS

Page

CHAPTER Page

LIST OF TABLES

LIST OF FIGURES

Figure Page

Figure Page

Figure Page

Chapter 1

INTRODUCTION

Piezoelectric thin films can convert electrical energy into mechanical energy and vice versa, depending on the applications of the device. The mechanical energy generated by an electric field is in the form of acoustic waves. For a particular orientation of the electric field, it can produce a longitudinal acoustic wave that travels in the direction of the film thickness (Fig.1.1). The acoustic wave is reflected at the film/air interface due to an impedance mismatch. An acoustic standing wave is formed when the thickness of the thin film (d) is equal to an integer multiple of a half of the acoustic wavelength (λ). The fundamental resonant frequency ($f = v_a / \lambda$) is then inversely proportional to the thickness of the piezoelectric material used, and is equal to $v_a/2d$, where v_a is the acoustic velocity at the resonant frequency. The acoustic standing wave in turn modifies the electric field distribution inside the piezoelectric film, which changes the electrical impedance of the device. Thus, the electrical impedance of the resonator varies with frequency.

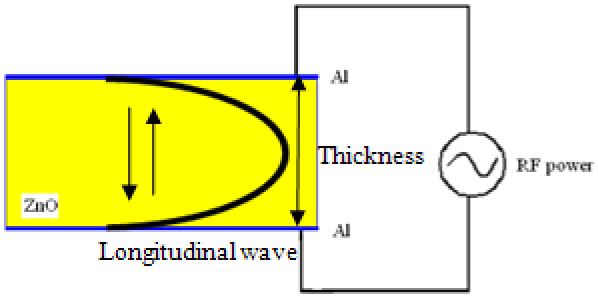

Figure 1.1 Schematic of longitudinal wave generation and propagation in an acoustic resonator by an electric field in the thickness direction.

For GHz resonance applications, the piezoelectric material must be thinner than a few µm thick. This kind of device is typically called Film Bulk Acoustic Resonator (FBAR). FBAR was first demonstrated by Grudkowski et al. (1980) and Nakamura et al. (1980) independently in 1980. Since then, research has been conducted in universities and industries all around the world.

Zinc oxide (ZnO) was used as the piezoelectric material in the early years of FBAR development, owing to the fact that it can be deposited by radio frequency (RF) sputtering and is easy to achieve reasonable piezoelectric properties. Sputtered aluminum nitride (AlN) was introduced as an alternative by Wang and Lakin (1981) in 1981. Compared with ZnO, AlN is difficult to sputter and usually resulted in films with poor piezoelectricity. In despite of such disadvantages, the attractive aspect of AlN is its compatibility with the existing IC facilities. ZnO has issues with volatility and contamination, which can cause damages to the IC processes.

As for the structures of FBAR, the following two approaches have been commonly employed (Fig.1.2). The first one consists of membrane structures formed by surface or bulk micromachining on a semiconductor wafer (Ruby and Merchant 1994). The second approach utilizes solid mounted structures with multiple acoustic-impedance-transforming layers to acoustically isolate the piezoelectric layer from the substrate (Lakin et al. 1995). In the membrane structures, acoustic energy is confined in the piezoelectric film, metal layers and supporting diaphragm due to the impedance mismatch between solid and air. Such structures are mechanically weak, however, it traps energy so well that the quality factor (Q) of the resonator is relatively high, typically over 1,000 at GHz. In the second method, the resonator sits on alternately deposited low and high acoustic impedance quarter-wave layers (acoustic Bragg reflector) on a solid substrate. The acoustic energy is mostly restricted in the metal/piezoelectric/metal layers, though a little is contained in the first several layers of the acoustic reflector. Such resonators look simple and dependable. Furthermore, going this way keeps open the door for future integration of FBAR with CMOS (complementary metal–oxide–semiconductor) into a single IC. However, the concerns are that the ability of the solid mounted structures to get sufficient Q and coupling between electrical and acoustic fields.

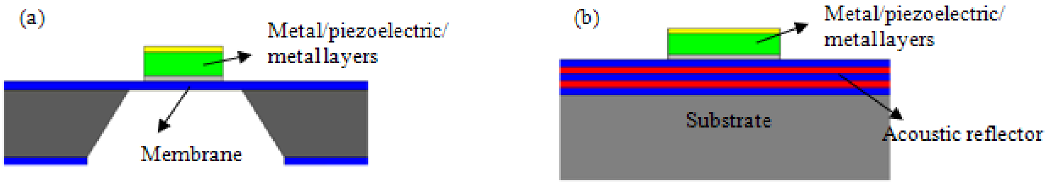

Figure 1.2 Two approaches to implement an FBAR: (a) membrane structures and (b) solid mounted structures.

FBAR had remained to be of research interest or for some very niche applications since its invention in the early 1980’s. In 1993, Hewlett Packard (HP) Laboratories launched their research effort on FBAR. However, without a strong value proposition, the project was constantly in danger of being shut down. In 1998, a value proposition was proposed for applying FBAR to cell phone duplexers. A duplexer is a device that allows bi-directional communication over a single channel. It is the “killer app” for FBAR, because this technology can eliminate the large ceramic devices used in cell phones. The dramatic size reduction has clear value to the handset manufactures. In late 1998, the FBAR team (now Avago) successfully fabricated a duplexer and wired it into a working phone, which they used to make a call to their upper management (Fig.1.3).

(a) (b)

Figure1.3 (a) Image of the first FBAR duplexer and cell phone. A ceramic duplexer is shown in front for size comparison. (b) Members of the FBAR team in 1998 were making the phone call with FBAR duplexer (Ruby 2009).

Early HP FBAR duplexer consisted of a printed circuit board the size of a piece of gum with three connections, including Tx, Rx and antenna ports. Because FBAR was a bulk device, it can withstand the high powers, meet the isolation specifications, and most importantly because of its small size, FBAR was quickly adapted into cell phones. Figure 1.4 illustrates the phone board of the Samsung SPH-S100 including the 6 × 11mm^2 FBAR duplexer. This phone was voted as one of the top five innovative products at Comdex 2000. With the introduction of FBAR duplexers, a new generation of smaller and lighter cell phones appeared in the market, making the bulky cell phones history. One of the first FBAR phones made by Sanyo was featured in the movie Men in Black II (2002) with Will Smith and Tommy Lee Jones (Fig. 1.4).

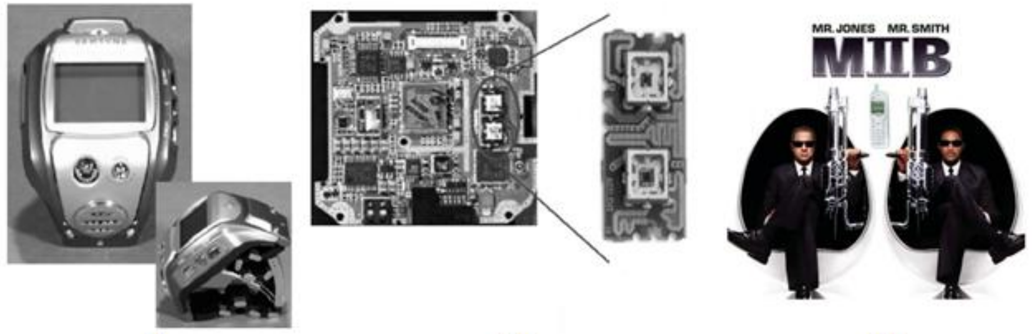

(a) (b) (c)

Figure1.4 (a) Picture of the Samsung SPH-S100. This phone was voted as one of the top five innovative products at Comdex 2000. (b) The phone board of the Samsung SPH-S100 including the $6 \times 11\text{mm}^2$ FBAR duplexer (Ruby 2009). (c) The first FBAR phone made by Sanyo (Sanyo 6200) was featured in the movie Men in Black II (2002).

Another active FBAR duplexer manufacturer is TriQuint, whose revenue in the consumer and mobile MEMS area expanded by 778.6 percent in 2010, amounting to $74.7 million, up from a negligible $8.5 million in 2009 (Pinelis 2011). The iPhone 4 and iPad 3G both integrated with TriQuint's TQM666092 transmit module, which consisted of a single-band power amplifier, a bulk acoustic wave (BAW) duplexer and a surface acoustic wave (SAW) interstage filter (Fig. 1.5). TriQuint has made a rapid rise to prominence in the BAW market. The company launched its BAW filter technology early in 2009 and by 2010 managed to grab 26% of the global BAW market from Avago.

Besides applications in cell phones, FBAR also drew a lot of attention as high sensitivity mass sensors in recent years. For an acoustic mass sensor, the fact that the resonant frequency of the acoustic resonator changes in response to the mass change on the resonator surface is employed. Surface acoustic wave sensor and bulk acoustic wave sensor have been the most common sensor types. In SAW sensors (Nomura et al. 1998), surface acoustic waves are generated by interdigital transducers (IDT). A standing wave (within a thin surface layer of the piezoelectric substrate) travels between two IDTs (one as the acoustic wave source, the other as the acoustic wave detector). Size of SAW sensor is usually large due to the length (between two IDTs) needed for acoustic wave delay. Bulk acoustic wave sensors, on the other hand, utilize longitudinal or shear waves that propagate in the bulk of the substrate. Quartz crystal microbalance (QCM) is a typical bulk acoustic wave type mass sensor (Zhang et al. 1998). QCM usually operates at a frequency of tens of MHz due to the limitation on how thin a quartz crystal can be manufactured. The relatively low operating frequency of QCM is the main reason for its low mass sensitivity compared with that of FBAR sensor, which usually operates in the GHz range.

Figure 1.5 Image of iPhone 4 with TriQuint transmit module.

The Butterworth-Van Dyke (BVD) equivalent circuit of an FBAR is shown in Figure 1.6(a), where C_0, L_m, C_m, and R_m are the clamped capacitance between the electrodes, motional inductance, motional capacitance, and motional resistance of the resonator, respectively. Series resonant frequency f_s and parallel resonant frequency f_p are determined by

$$f_s = \frac{1}{2\pi\sqrt{L_m C_m}} \tag{Eq. 1.1}$$

$$f_p = \frac{1}{2\pi\sqrt{L_m \frac{C_m C_0}{C_m + C_0}}} \tag{Eq. 1.2}$$

The modified BVD equivalent circuit of FBAR with mass loading is shown in Figure 1.6(b) (Martin et al. 1991). In the equivalent circuit, the elements are related to the physical parameters of the resonator and added mass by

$$C_0 = \frac{\varepsilon A}{d_0} \tag{Eq. 1.3}$$

$$C_m = \frac{8k_t^2 C_0}{\pi^2} \tag{Eq. 1.4}$$

$$L_m = \frac{1}{4\pi^2 f_s^2 C_m} \tag{Eq. 1.5}$$

$$R_m = \frac{\eta_0}{\rho_0 v_a^2 C_m}\left(\frac{f}{f_s}\right)^2 \tag{Eq. 1.6}$$

$$L_1 = \frac{4 f_s L_m \rho_1 d_1}{\rho_0 v_a} \tag{Eq. 1.7}$$

where A is the area of the resonator; d_0 is the thickness of the piezoelectric layer; ε is the permittivity of the piezoelectric layer; k_t^2 is the electromechanical coupling constant; η_0 is the acoustic viscosity in the piezoelectric layer; ρ_0 is the density of the piezoelectric layer; v_a is the acoustic velocity in the piezoelectric layer; ρ_1 is the density of the added mass; and d_1 is the thickness of the added mass; L_1 is the inductance induced by the added mass.

From Eq. 1.1 and 1.2 and the equivalent circuits, it is clear that the series and parallel resonant frequencies of FBAR will be lowered with mass loaded onto the surface of the resonator. The mass loading affects the resonant frequencies at the series and parallel resonances equally. The frequency shift of the resonator due to additional mass loading can be derived as follows. Take parallel resonant frequency f_p as an example, f'_p is the parallel resonant frequency with mass loading.

$$f'_p = \frac{1}{2\pi\sqrt{(L_m + \Delta L)\dfrac{C_m C_o}{C_m + C_o}}} \qquad \text{(Eq. 1.8)}$$

$$\Delta L = L_1 \qquad \text{(Eq. 1.9)}$$

$$C' = \frac{C_m C_o}{C_m + C_o} \qquad \text{(Eq. 1.10)}$$

$$L_m = \frac{1}{4\pi^2 f_p{}^2 C'} \qquad \text{(Eq. 1.11)}$$

$$L_1 = \frac{2L_m \rho_1 d_1}{\rho_0 d_0} \qquad \text{(Eq. 1.12)}$$

From the equations above,

$$\Delta L = \frac{1}{4\pi^2 C'}\frac{f_p^2 - f'^2_p}{f_p^2 f'^2_p} \approx \frac{1}{4\pi^2 C'}\frac{2\Delta f_p}{f_p f'^2_p} \qquad \text{(Eq. 1.13)}$$

$$\Delta f_p = f_p - f'_p \qquad \text{(Eq. 1.14)}$$

$$\frac{\Delta f_p}{f_p} = \frac{\Delta L}{2} \frac{1}{L_m + \Delta L} \approx \frac{\Delta L}{2L_m} = \frac{\rho_1 d_1}{\rho_0 d_0} \qquad \text{(Eq. 1.15)}$$

The Eq.1.15 is in a form of the classic Sauerbrey equation that indicates the resonant frequency of an acoustic resonator is linearly related to the mass of a material accumulated on the resonator. It is also important to note that the above equation is valid only when the ratio in either side is smaller than 2% (Benes 1984), because when the loading layer gets thicker, the mass loading effect is no longer solely responsible for the resonant frequency shift. Elastic modulus of the added layer also affects the resonant frequency, and its effect becomes comparable to that of mass loading as the added layer increases.

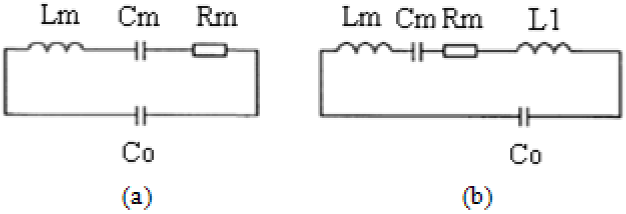

Figure 1.6 Butterworth-Van Dyke (BVD) equivalent circuits: (a) FBAR without mass loading and (b) FBAR with mass loading.

Mass sensitivity S_m of a piezoelectric mass sensor can be defined as (Wenzel and White 1989)

$$S_m = \lim_{\Delta m \to 0} \left(\frac{\Delta f}{f} \right) \left(\frac{1}{\Delta m} \right) \qquad \text{(Eq. 1.16)}$$

where Δm is the mass added to the sensor per unit area. Using Eq.1.15 in Eq.1.16,

$$S_m = \frac{1}{\rho_0 d_0} \qquad \text{(Eq.1.17)}$$

FBAR is a composite structure consisting of a piezoelectric layer, two metal layers and a supporting layer. Mass sensitivity of such a composite resonator can be calculated by a more generalized equation

$$S_m = \frac{1}{\sum_i \rho_i d_i} \qquad \text{(Eq.1.18)}$$

where ρ_i and d_i are density and thickness of the i^{th} layer in the composite resonator, respectively. If an FBAR has a structure of Al/ZnO/Al/SiN (0.1μm/1.2μm/0.1μm/0.6μm), the mass sensitivity of the FBAR is calculated to be 1095cm^2/g, more than 70 times that of a QCM operating at 6MHz (Lu and Lewis 1972).

Various FBAR sensors have been developed based on mass load effect. Lin and Kim (2009) investigated FBAR with antibody coating to detect TNT (Trinitrotoluene) in the environment without any pre-concentrator. The experimental results demonstrated the selectivity and long term reliability of the device. The anti-TNT antibody coated FBAR sensor was shown to produce a permanent frequency shift in response to TNT. Other chemicals can only produce some temporary frequency shifts due to adsorption (Fig. 1.7). The anti-TNT antibody can be functionally good for up to 30 days at room temperature.

Yan et al. (2007) employed FBAR as a biosensor through incorporating biospecies on the resonator surface. The electrical measurements revealed that the FBAR consisting of a 750nm thick ZnO layer had a high resonant frequency of 3.94GHz. A large shift of the resonant frequency was observed as different biospecies were adsorbed on the device (Fig. 1.8). The sensitivity of the FBAR sensor was found out to be 8970Hzcm^2/ng.

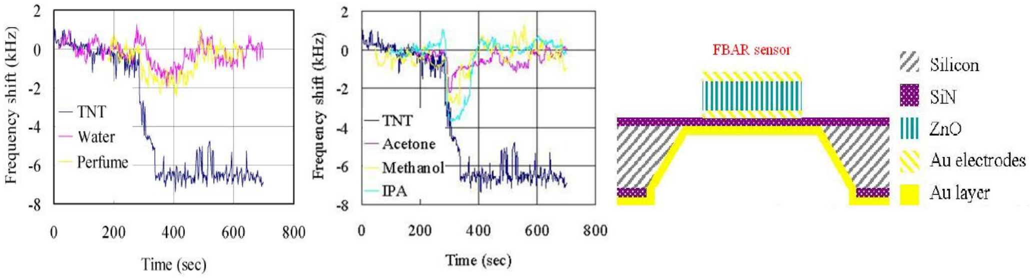

Figure 1.7 The response of the FBAR sensor to different chemicals. Permanent frequency shifts were observed only with TNT (Lin and Kim 2009).

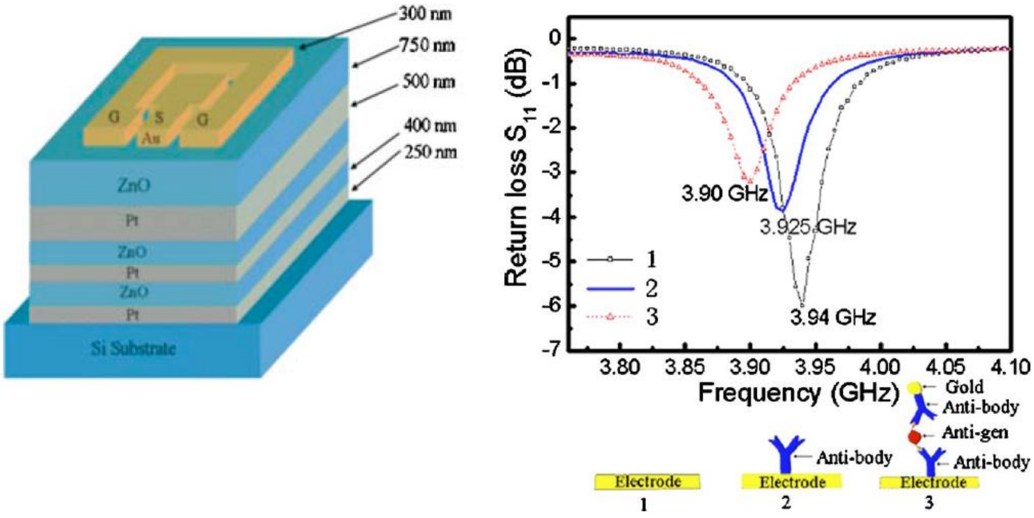

Figure 1.8 The return loss of ZnO FBAR: (1) bare device, (2) after bioimmobilization, and (3) after protein coupling (Yan et al. 2007).

Ashley et al. (2010) applied the hygroscopic polymer poly[vinylpyrrolidone] (PVP) to the surface of FBAR to monitor relative humidity (RH). PVP coated and uncoated FBARs were demonstrated to be useful as humidity sensors within the RH range of 20% to 70% and were able to continuously monitor real time RH changes (Fig. 1.9). Increasing PVP film thickness or polymer chain length (molecular weight) enhanced the RH response.

FBAR had the ability to function as a sensor even when the polymeric film thickness on its surface was greater than the thickness of the entire device.

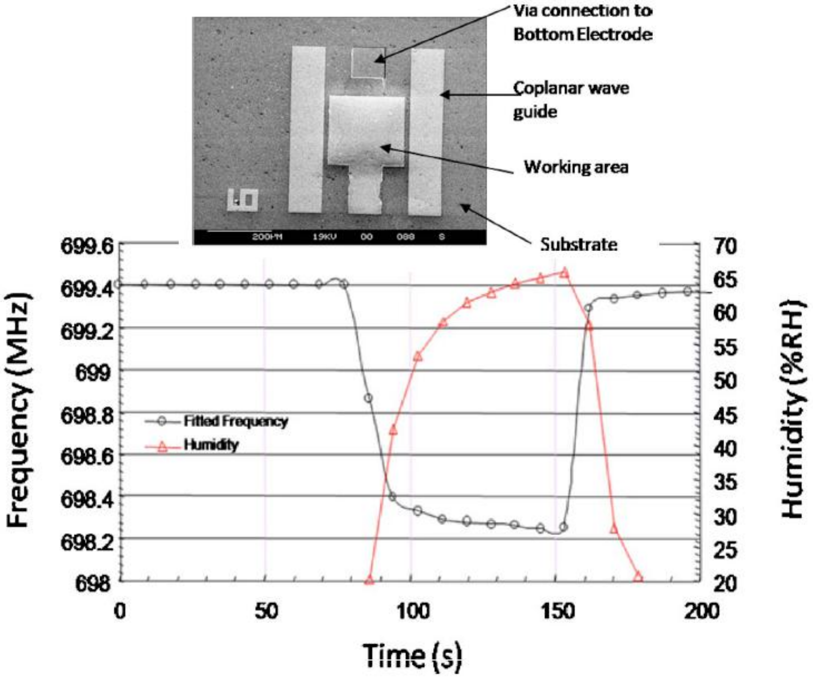

Figure 1.9 The response of the PVP coated FBAR to relative humidity (Ashley et al. 2010).

Johnston et al. (2010) built a FBAR oscillator array for mass sensing applications. It exhibited a mass sensitivity of 3.28Hzcm^2/g, while oscillating around 870MHz. This implementation can overcome the spatial and parasitic limitations imposed by package level FBAR integrations to enable a dense sensor array.

In a FBAR mass sensor, generally a sensing layer is employed to attract the sensing target. On the other hand, one of the building blocks of the FBAR, ZnO, can be used as a sensing platform for a variety of applications. This approach can eliminate the additional structures, reduce the fabrication cost and simplify the fabrication process.

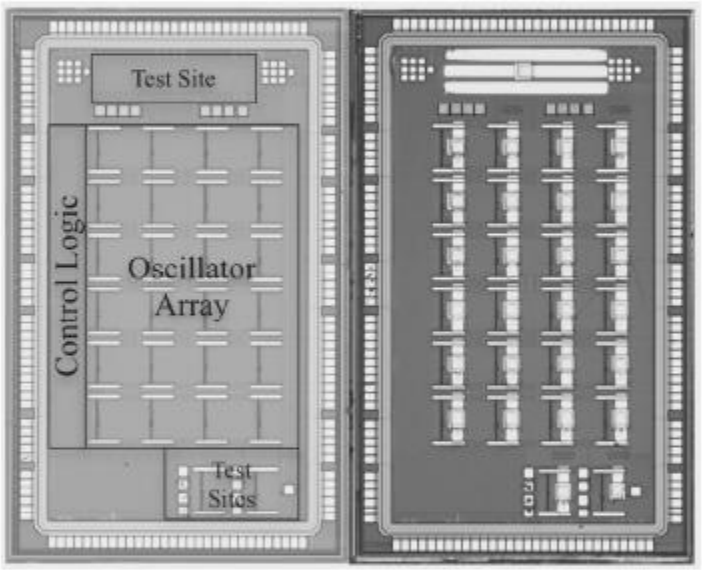

Figure 1.10 The image of the FBAR oscillator mass sensor array (Johnston et al. 2010).

ZnO, both in thin film and nanostructure forms, have been used as sensing materials in many occasions, including ultraviolet detectors (Law and Thong 2006), gas sensors (Chatterjee et al. 1999), and biosensors (Fulati et al. 2010). In this study, novel sensing applications using ZnO based FBAR were developed. FBAR was employed to monitor ultraviolet (UV), relative humidity (RH) and reducing gases, such as acetone and ethanol. Different from the mass loading effect, a sensing mechanism based on the density change induced by adsorption/desorption of oxygen on the ZnO surface was proposed.

The dissertation is arranged in the following manners. In Chapter 1, an introduction to film bulk acoustic resonator was given. The various applications of FBAR were emphasized. In Chapter 2, FBAR was investigated as a low intensity ultraviolet (UV) sensor. The influence of different environmental factors on the UV response of FBAR was discussed.

Chapter 3 presented an FBAR RH sensor. The RH response was interpreted using an analytical model developed from the semiconductor gas sensor power law theory and the mass loading effect. Chapter 4 talked about the sensing properties of FBAR for acetone and ethanol. A theoretical model was investigated to address the effect of the properties of ZnO film on the gas sensing performance of FBAR combining the depletion theory of the semiconductor with the dynamics of adsorption and/or reactions of gases on the ZnO surface.

In Chapter 5, a novel wafer level packaging method using the localized heating approach was addressed. Ni/Al reactive multilayer nanofilms were employed as localized heaters to melt adhesive layers and thus bond different materials. Chapter 6 introduced a *p*H measurement device based on ZnO surface acoustic wave resonator. The response of the *p*H sensor was explained using the acoustoelectric effect. At last in Chapter 7, conclusion and future works of this dissertation were presented.

Chapter 2

FILM BULK ACOUSTIC RESONATOR BASED ULTRAVIOLET SENSOR

Detection of ultraviolet (UV) radiation is very important in a number of areas, such as astronomy, resin curing of polymeric materials, combustion engineering, water purification, flame detection and biological effects with more recent proposals like early missile plume detection, secure space-to-space communications and pollution monitoring. UV detectors with metal-semiconductor-metal (MSM) structures have been reported extensively. They can be realized either by ohmic contact photoconductive principle (Xu et al. 2006) or Schottky barrier photovoltage principle (Jiang et al. 2008) using ZnO films. ZnO nanostructures have also been explored for UV detecting devices, as they possess single crystal structure characteristics with high surface-to-volume ratio, and have the capability of operating in harsh environment, such as at high temperatures (Law and Thong 2006; Zhou et al. 2009). In all the detectors mentioned above, generally a change in the photogenerated current was measured in the presence and absence of UV illumination. As the UV intensity falling on the sensor decreased, the photogenerated current became comparable to the dark current, or noise level, and resulted in difficulties in measurement. Alternatively, surface acoustic wave (SAW) resonant UV sensors have also been developed with photoconductive ZnO film deposited on top of a SAW filter as a UV sensitive layer. The detection limits were 50 μW/cm^2 using insertion loss as the photoresponse signal (Huang and Ma 2008) and 10 μW/cm^2 by incorporating the

SAW filter in an electric oscillation loop (Sharma and Screenivas 2003). Table 2.1 compares different kinds of UV sensors using ZnO film as sensing layer.

2.1 Design and fabrication of FBAR UV sensor

The schematic structure of the FBAR UV sensor is shown in Figure 2.1. The FBAR was fabricated on top of a SiN diaphragm (0.6 µm thick). A sputtered ZnO film (1.2 µm thick) acted both as the UV sensitive layer and the piezoelectric actuation layer for the FBAR sensor. The top and bottom electrodes were made of Cr/Au (0.02 µm/0.2 µm thick) and Al (0.2 µm thick), respectively. The fabrication process of the FBAR UV sensor was as follows. In the first step, a SiN layer was deposited on a Si wafer (100) with low-pressure chemical vapor deposition (LPCVD). Then the Si wafer was etched from the backside anisotropically in potassium hydroxide (KOH) to form the cavity. Next, the bottom Al electrode was deposited by electron-beam (e-beam) evaporation and patterned on top of the SiN film using wet chemical etching. ZnO was radio-frequency (RF) sputtered and etched to form the desired pattern. The last step was the e-beam deposition and patterning of top Cr/Au electrode by lift-off (Fig. 2.2).

Table 2.1 Comparison between different kinds of ZnO film based UV sensors.

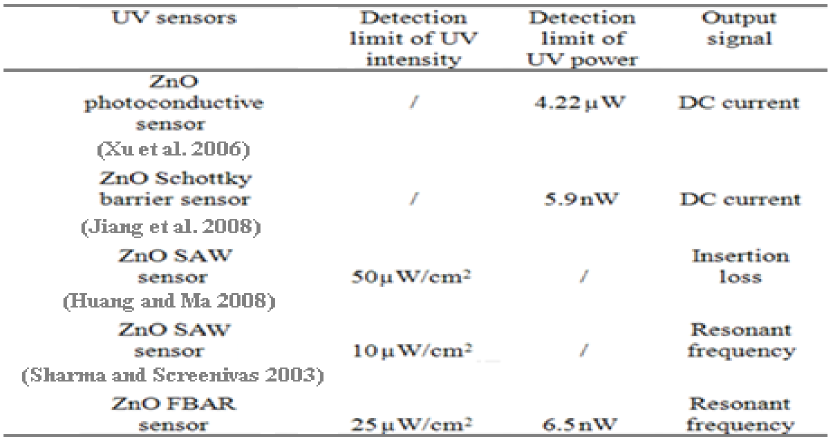

UV sensors	Detection limit of UV intensity	Detection limit of UV power	Output signal
ZnO photoconductive sensor (Xu et al. 2006)	/	4.22 µW	DC current
ZnO Schottky barrier sensor (Jiang et al. 2008)	/	5.9 nW	DC current
ZnO SAW sensor (Huang and Ma 2008)	50 µW/cm²	/	Insertion loss
ZnO SAW sensor (Sharma and Screenivas 2003)	10 µW/cm²	/	Resonant frequency
ZnO FBAR sensor	25 µW/cm²	6.5 nW	Resonant frequency

2.2 Experiment setup

The ZnO film was characterized by X-ray diffraction (XRD). A versatile hand-held ultraviolet lamp (365nm, Cole-Parmer, Vernon Hills, IL) was used as the UV source. A UVX digital ultraviolet intensity meter (Cole-Parmer, Vernon Hills, IL) was applied to calibrate the UV power received by the FBAR sensor. FBAR was tested on a probe station with Ground-Signal-Ground 150 micron pitch probes (Cascade Microtech Inc, Beaverton, OR). The calibration was carried out with an impedance standard substrate using a short-open-load (SOL) method. The resonant frequency of the FBAR was monitored with an Agilent E5071C network analyzer (Agilent, Santa Clara, CA) and recorded by a LabVIEW program (National Instruments, Austin, TX). The testing setup is shown in Figure 2.3.

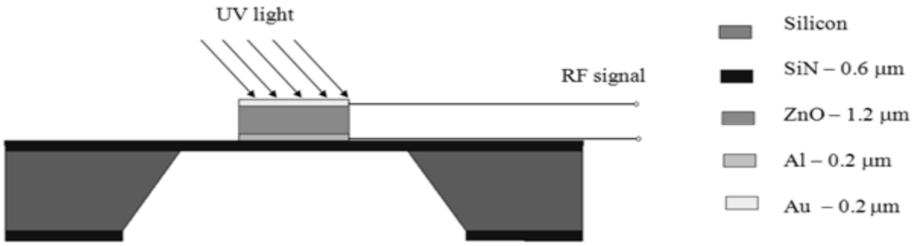

Figure 2.1 Schematic cross-sectional structure of FBAR UV sensor.

2.3 UV testing results

In the XRD trace of the ZnO film (Fig. 2.4), only the Bragg reflection corresponding to (002) planes was observed, indicating that the film had preferred orientation along the wurtzite C axis, normal to the silicon substrate. The full width at half maximum (FWHM) of the rocking curve was around 7.9 degree.

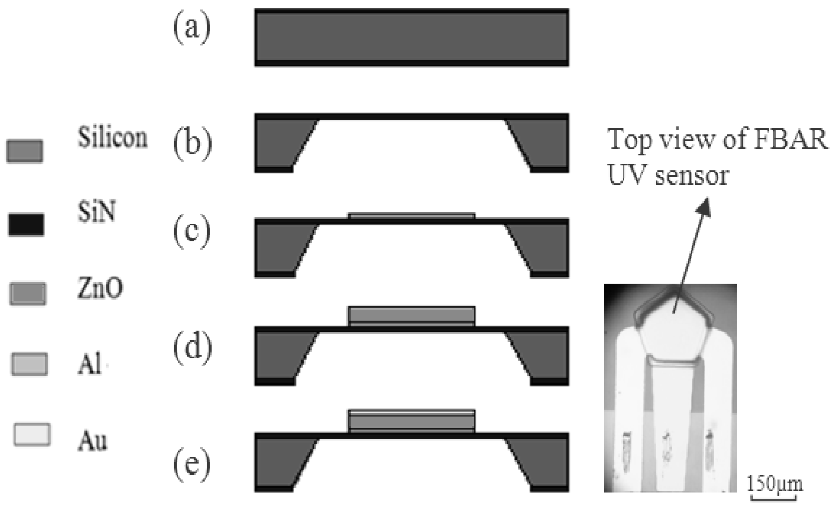

Figure 2.2 (left) Fabrication process of FBAR UV sensor: (a) deposit SiN on Si; (b) etch Si with KOH; (c) deposit and pattern bottom Al electrode; (d) sputter and pattern ZnO; (e) deposit and pattern top Cr/Au electrode. (right) Fabricated sensor.

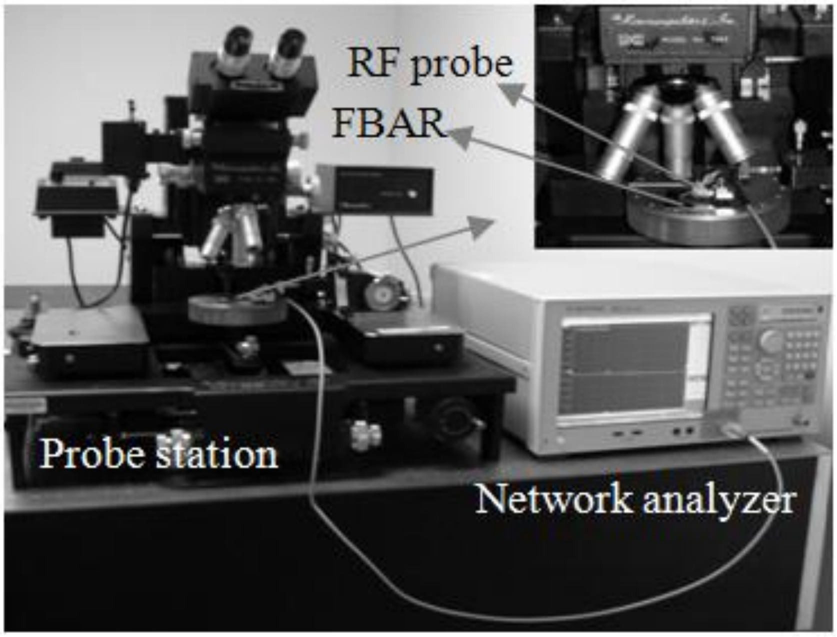

Figure 2.3 Photo of the testing setup: FBAR sensor with RF probe connected to Agilent E5071C network analyzer.

The quality factor (Q) of the FBAR was calculated to be between 400 and 420 using the following equation:

$$Q_{s/p} = \frac{f_{s/p}}{2} \left| \frac{d\phi_{zs/p}}{df} \right|_{f=f_{s/p}} \qquad \text{(Eq. 2.1)}$$

where $Q_{s/p}$ is the quality factor at series/parallel resonance; $f_{s/p}$ is the series/parallel resonant frequency; and $\O_{zs/p}$ is the impedance phase near series/parallel resonance (Pang et al. 2005). The frequency noise floor of the FBAR sensor was 1.5ppm at 1.4 - 1.5GHz. Figure 2.5 shows the frequency response of the FBAR sensor with a UV intensity of 600 μW/cm^2. An upshift of 9.8kHz was observed. This frequency upshift cannot be attributed to the temperature increase at the ZnO surface under UV illumination, since for ZnO FBAR without compensation layer, the temperature coefficient of resonant frequency (TCF) was negative, indicating a frequency downshift with increasing temperature (Lakin et al. 2001).

Different intensities of UV light were applied to monitor the photoresponse of the FBAR sensor. The results were shown in Figure 2.6. As the intensity increased, the frequency upshift also increased. At low intensity region (as shown in Figure 2.6), the relationship was almost linear, which made FBAR UV sensor suitable to detect low intensity UV. The lowest detectable intensity was around 25 μW/cm^2, which was comparable to the SAW UV sensor mentioned above. With the current sensing area of 0.026mm^2, the minimum UV power detectable was calculated to be 6.5nW. Figure 2.7 shows four cycles (one cycle lasted 40s) of response of the FBAR sensor with a UV intensity of 290 μW/cm^2. The results demonstrated good repeatability and stability of the sensor. The slight decay of the frequency pedestal in Figure 2.7 can be attributed to the temperature rise due to the residual heating from the UV lamp.

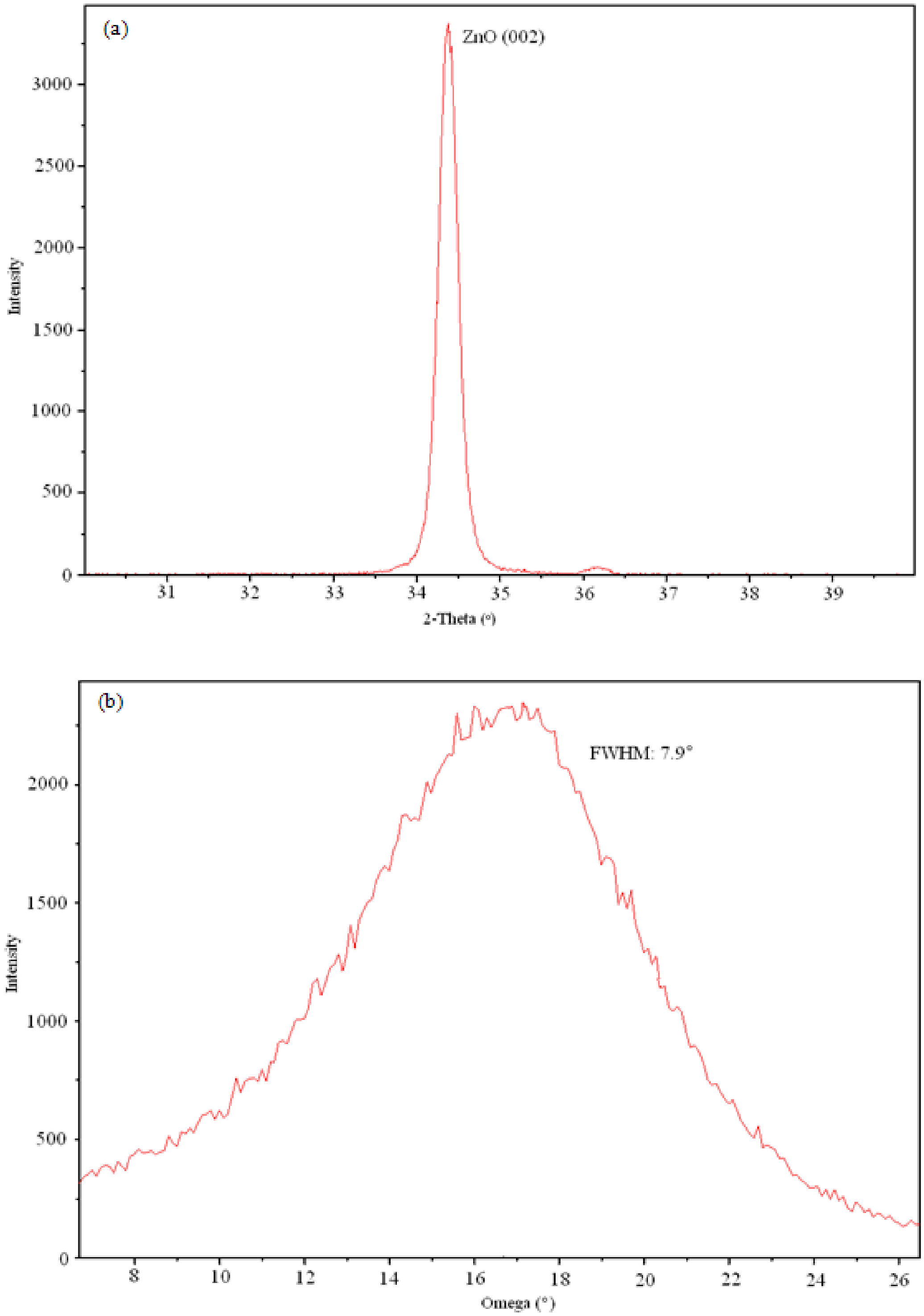

Figure 2.4 (a) XRD trace of the ZnO film illustrating that it had (002) crystal orientation. (b) Rocking curve of the ZnO film with a full width at half maximum (FWHM) of 7.9 degree.

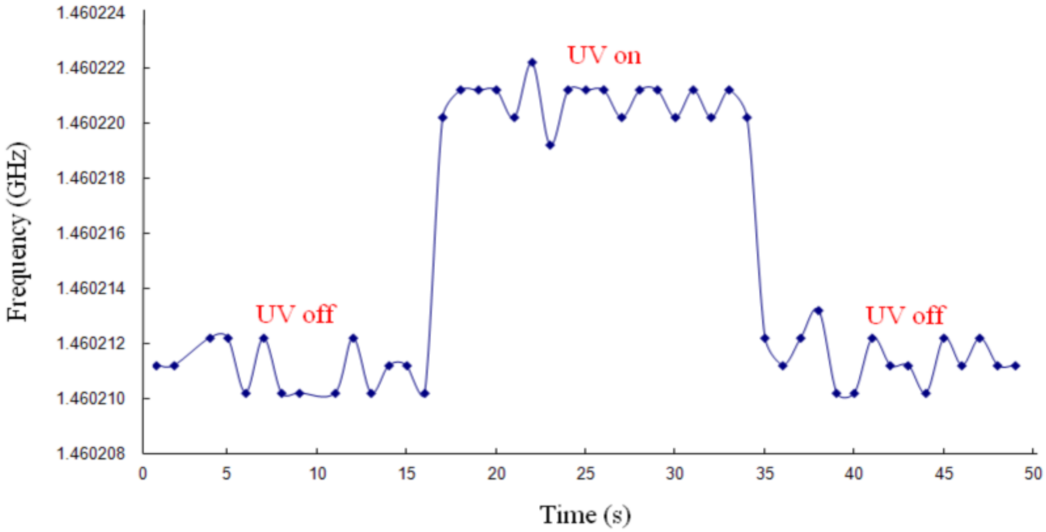

Figure 2.5 UV light sensing result with frequency upshift: when there was UV illumination (600 μW/cm^2), a frequency upshift of 9.8kHz was observed.

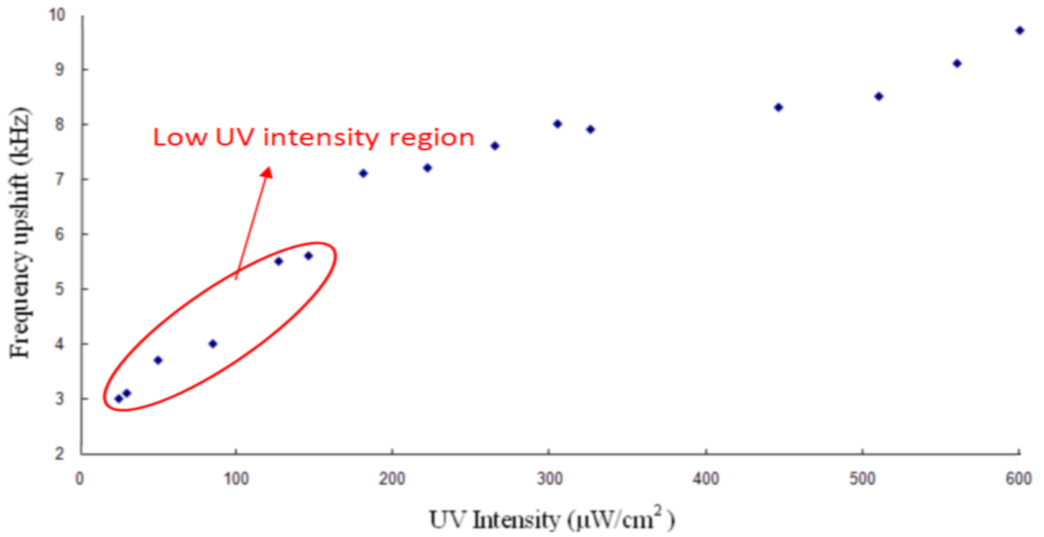

Figure 2.6 The resonant frequency upshift of FBAR vs. UV light intensity, which showed frequency upshift increased with increasing UV light intensity. In the low intensity region, the relationship was almost linear.

2.4 UV sensing mechanism

Frequency upshift was observed previously by Sharma et al. (2003) in their SAW UV sensor which utilized a ZnO/fused quartz SAW delay line. They proposed that the change of elastic constant of the ZnO film due to UV stiffening was the main reason for the frequency upshift. However, there was no experimental evidence for their explanation. For our FBAR UV sensor, an alternative interpretation for the frequency upshift was suggested as follows.

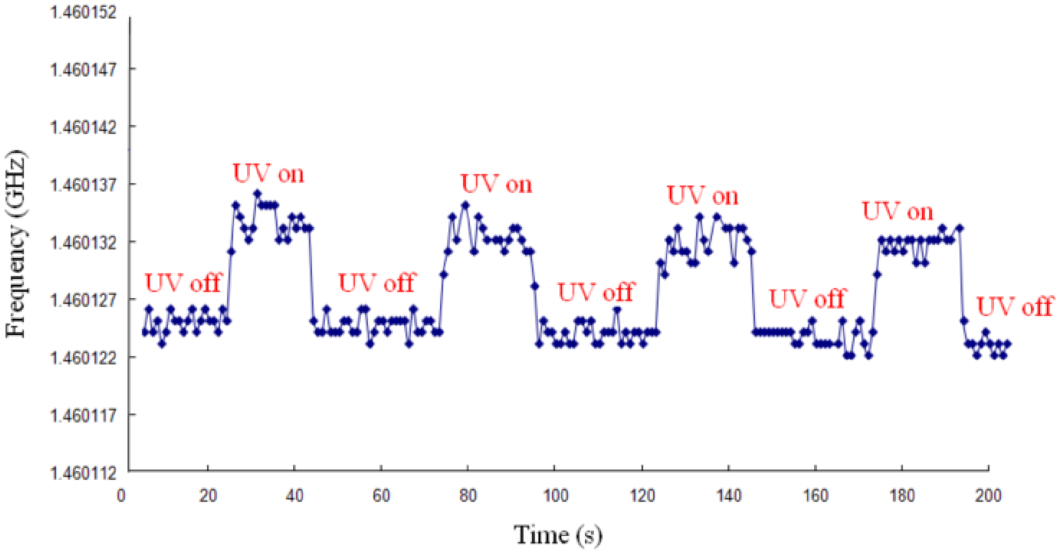

Figure 2.7 Four cycles (one cycle lasted 40s) of response of the FBAR sensor with a UV intensity of 290 μW/cm^2. A frequency upshift of 7.7kHz was observed.

The resonant frequency of the FBAR can be determined from the following two equations:

$$v = \sqrt{\frac{E}{\rho}} \qquad \text{(Eq. 2.2)}$$

$$f = \frac{v}{2d} \qquad \text{(Eq. 2.3)}$$

where E, ρ and d are the elastic constant, density and thickness of the ZnO film, respectively. v is the acoustic velocity inside the film and f is the resonant frequency of the FBAR. Therefore, the frequency upshift may be due to the density decrease of the ZnO film upon UV illumination. It is well established that when UV light is incident, electron-hole pairs are generated inside the ZnO film.

The holes produced by light absorption migrate to the surface and discharge the negatively charged adsorbed oxygen ions and surface lattice oxygen ions. When an oxygen ion is discharged by the capture of a hole, it will be thermally desorbed (Melnick 1957; Collins and Thomas 1958; Takahashi et al. 1994). In this way, the density of the ZnO film will decrease, resulting in the increase of acoustic velocity. Therefore, the resonant frequency of the FBAR sensor will increase. When UV light is absent, oxygen readsorption will occur. Consequently, the density of the ZnO film will increase and the resonant frequency of FBAR will decrease.

In order to support the above assumption, acetone vapor was applied to the sensor to monitor its response. It is known that oxygen is adsorbed on the ZnO film through capturing electrons from the film. When ZnO is exposed to acetone, the reducing gas molecules will react with the oxygen ions on the film, and release the adsorbed oxygen (Han et al. 2007). Thus, the density of the ZnO film will decrease and a frequency upshift of the FBAR can be expected. Figure 2.8 shows the response of the FBAR sensor to 100ppm acetone. A frequency upshift of 10.3kHz was observed. UV light with intensity of 600μW/cm^2 was applied subsequently, and caused a 6.0kHz frequency upshift (Fig. 2.8). This response was smaller compared to the frequency upshift without acetone (Fig. 2.5). It can be interpreted as following: acetone had already reacted with some surface oxygen ions in the ZnO film. Thus, when UV light was incident, there were fewer oxygen ions left on the film surface to be desorbed by UV. In this way, the frequency upshift became smaller with the same UV intensity. These results illustrated that UV light and acetone shared a similar mechanism to upshift the frequency of the FBAR sensor. Both of them can cause the density of the ZnO film to decrease and result in a frequency upshift. In Figure 2.8, it was obvious that acetone possessed a much longer frequency decay time compared to UV light. UV can penetrate only around 40nm into the ZnO film (Jeong et al. 2003). Therefore, the UV response of the sensor is a surface phenomenon with a short response time. However, acetone can react with the bulk of the ZnO film by diffusion. Therefore, the acetone response is a bulk process, which is characterized by a long response time. It took as long as 250s for the resonant frequency to drop back to the original value with 100ppm acetone and an exposure time of 25s.

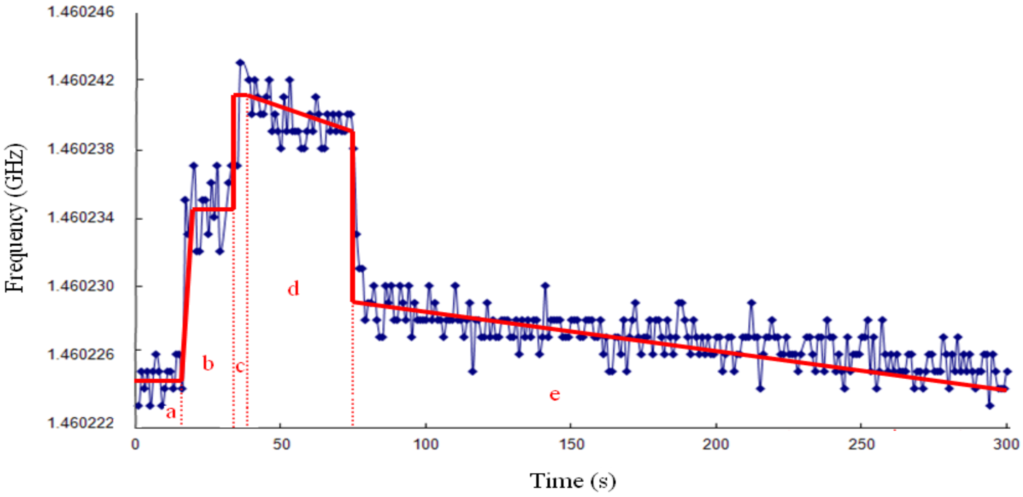

Figure 2.8 Acetone and UV exposure to the FBAR sensor. Frequency upshifted (10.3kHz) upon acetone (100ppm) exposure (stage b). It was followed by a subsequent upshift (6.0kHz) due to UV (600 μW/cm^2) illumination (stage c). When acetone was cut off, frequency began to decrease (stage d). After turning off UV light, there was a fast decay of frequency followed by a slow one (stage e). It took as long as 250s for the resonant frequency to drop back to the original value.

Ozone can capture free electrons from the ZnO film (Martines et al. 2004). When it is introduced to the FBAR sensor, it can increase the density of the ZnO, resulting in a frequency downshift according to the above assumption. Figure 2.9 shows the response of the FBAR sensor to 1400ppb ozone at room temperature. A frequency downshift of 131kHz was observed with a response time of 12s. Three testing cycles were recorded to demonstrate the repeatability and stability of the sensor. The increase of temperature may result in a frequency downshift due to the negative temperature coefficient of resonant frequency (TCF) of ZnO based FBAR (Qiu et al. 2010). The measured TCF for the ozone sensor was -72.7ppm/^{o}C. The temperature of the sensor was monitored during ozone testing, and a change of less than 0.1^{o}C was observed. Therefore, the frequency downshift cannot be explained by the TCF of the device and was in fact the result of interaction between ozone and the ZnO film on the FBAR. The experiment results were in agreement with the proposed sensing mechanism of the FBAR sensor.

2.5 The effects of environmental factors on the UV response of FBAR

For ZnO UV detectors, the surface adsorbed oxygen plays an important role in their response to UV illumination. Different environmental factors, such as temperature, relative humidity and the presence of reducing gases can influence the adsorption of oxygen on the ZnO surface. Therefore, they will affect the UV response of the ZnO based detectors. Liao et al. (2009) reported the temperature dependence of photoconductivity in single ZnO nanowires. The effects of humidity on the photoresponse of ZnO nanowires were explored by Li et al. (2009). In this study, the influence of temperature, relative humidity and reducing gases on the UV response of the FBAR was investigated. These environmental factors need to be taken into consideration during the design and packaging of the device to forward it to real life applications.

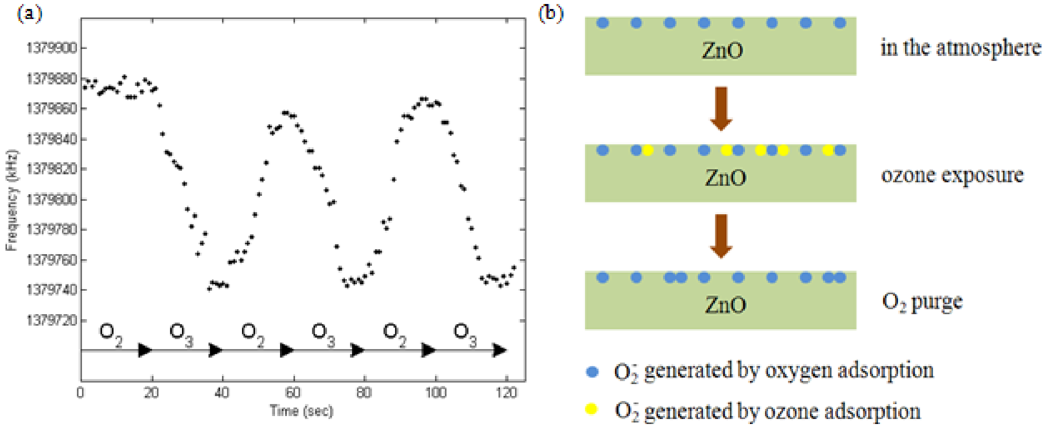

Figure 2.9 (a) The response of the FBAR sensor to 1400ppb ozone at room temperature. A frequency downshift of 131kHz was observed with a response time of 12s. Three testing cycles were recorded to demonstrate the repeatability and stability of the sensor. (b) The sensing mechanism of the FBAR ozone sensor. Ozone can capture free electrons from the ZnO film. It will be adsorbed on the ZnO surface as negative oxygen ions, resulting in an increase in film density. Because of the increased density, the acoustic velocity decreases, as does the resonant frequency of the FBAR. During the oxygen purge stage, oxygen ions generated by ozone will be desorbed due to the decreased ozone concentration. In this process, the density of the ZnO film decreases, resulting in an increase of resonant frequency. Due to the high oxygen concentration during oxygen purge compared to the atmospheric case, additional oxygen is adsorbed on the ZnO film, which prevents the resonant frequency recovering to the original value, as shown in (a).

The measured resonant frequency of the FBAR sensor was around 1.4GHz with a noise floor of 0.7ppm in this case, which was suitable for integration with a wireless sensor network. The quality factor of the FBAR was about 550-570. A HCC214S hot chuck system (INSTEC, Boulder, CO) was employed to adjust the temperature of the FBAR. And the humidity was measured by a HH314A humidity temperature meter (OMEGA, Stamford, CT).

Figure 2.10(a) shows the shift of resonant frequency with temperature for the FBAR sensor. A temperature coefficient of resonant frequency (TCF) of -63.2ppm/^{o}C was obtained. For the ZnO based FBAR, the variation of the resonant frequency with temperature is mainly due to the dependence of the acoustic velocity on temperature. For most materials (such as Al and ZnO), Young’s modulus decreases as temperature increases due to the material softening. Although the mass density also decreases with temperature, the acoustic velocity decreases as temperature increases, owing to the dominant effect of the Young’s modulus, resulting in a negative TCF.

In Figure 2.10(b), the UV response (600μW/cm^2) of the FBAR sensor under different temperatures is illustrated. As the temperature increased from 25^{o}C to 32^{o}C, the frequency upshift decreased from 18.2kHz to 17.4kHz. It further decreased to 16.6kHz and 15.8kHz when the temperature reached 39.6^{o}C and 44.9^{o}C. As mentioned before, ultraviolet radiation can generate electron-hole pairs in the ZnO film. The holes produced can migrate to the surface and discharge the negatively charged adsorbed oxygen ions, resulting in oxygen desorption from the ZnO film. With the same UV intensity, the amount of oxygen desorbed remains almost the same, which means the density decrease $\Delta\rho$ induced by UV is constant at different temperatures.

The shift of resonant frequency Δf due to UV illumination can be formulated as following.

$$\Delta f = \frac{1}{2d}\left(\sqrt{\frac{E}{\rho-\Delta\rho}}-\sqrt{\frac{E}{\rho}}\right)=\frac{\sqrt{E}}{2d}\frac{\left(1-\sqrt{1-\frac{\Delta\rho}{\rho}}\right)}{\sqrt{\rho-\Delta\rho}} \tag{Eq. 2.4}$$

In the equation above, $\rho \gg \Delta\rho$. In this way,

$$\Delta f \approx \frac{\sqrt{E}}{2d} \cdot \frac{\left(1 - 1 + \frac{1}{2}\frac{\Delta\rho}{\rho}\right)}{\sqrt{\rho}} = \frac{\sqrt{E}}{4d\rho\sqrt{\rho}}\Delta\rho \qquad \text{(Eq. 2.5)}$$

As temperature increases, the Young's modulus of ZnO decreases (Pang et al. 2005). Therefore, a smaller frequency upshift can be expected at high temperature if we assume the density of the ZnO film does not change in the experiment temperature range (from 25^{o}C to 45^{o}C).

Sharma et al. (2003) assumed that the change of the elastic modulus (ΔE) of the ZnO film due to UV stiffening was the main reason for the frequency upshift in their SAW UV sensor. However, UV stiffening cannot be used to explain the results shown in Figure 2.10(b).

The shift of resonant frequency Δf due to UV stiffening is as follows.

$$\Delta f = \frac{1}{2d}\left(\sqrt{\frac{E + \Delta E}{\rho}} - \sqrt{\frac{E}{\rho}}\right) = \frac{\sqrt{E}}{2d}\frac{\left(\sqrt{1 + \frac{\Delta E}{E}} - 1\right)}{\sqrt{\rho}} \qquad \text{(Eq. 2.6)}$$

In the equation above, $E \gg \Delta E$. In this way,

$$\Delta f \approx \frac{\sqrt{E}}{2d} \cdot \frac{\left(1 + \frac{1}{2}\frac{\Delta E}{E} - 1\right)}{\sqrt{\rho}} = \frac{\Delta E}{4d\sqrt{\rho E}} \qquad \text{(Eq. 2.7)}$$

With the same UV intensity, the stiffening effect is assumed to be the same in the experiment temperature range. However, a smaller E occurs at high temperature. If UV stiffening is the main reason for the frequency upshift, it will result in an enhanced UV response (assuming constant ZnO density in the experiment temperature range). In contrast, in our experiment, a lower UV response was observed. Thus, UV stiffening can be ruled out as the main reason for the frequency upshift obtained in the FBAR sensor.

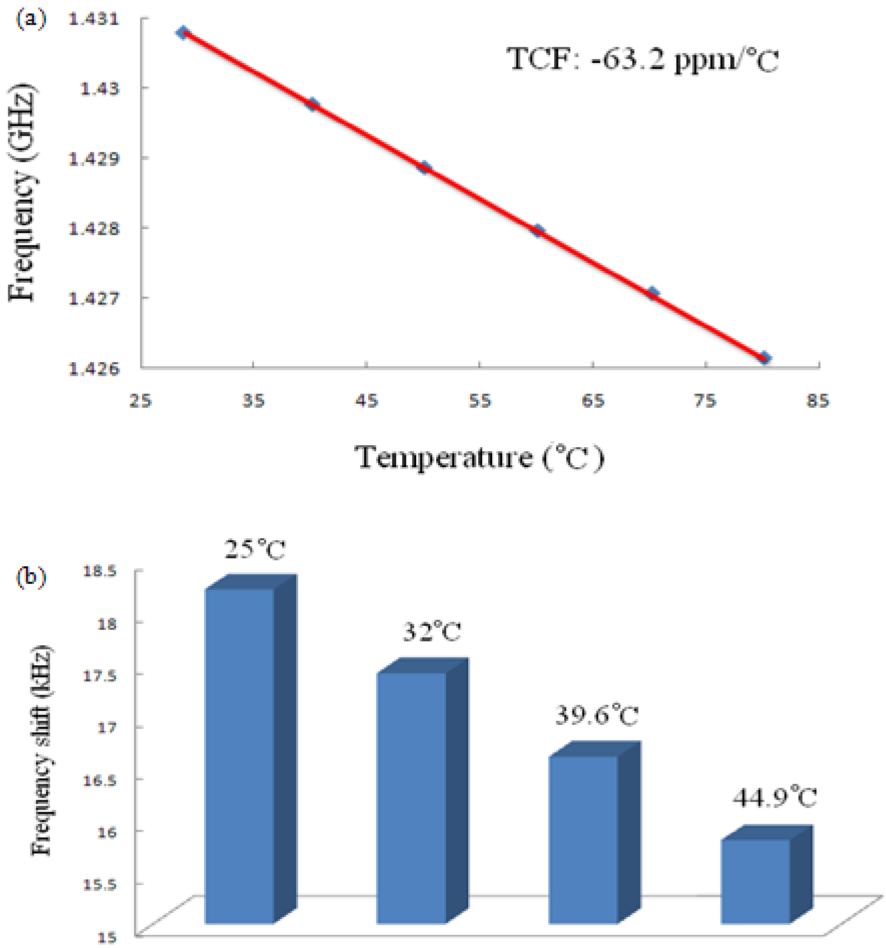

Figure 2.10 (a) The shift of resonant frequency with temperature for the FBAR sensor. A temperature coefficient of resonant frequency (TCF) of -63.2ppm/°C was obtained. (b) The UV response ($600 \mu W/cm^2$) of the FBAR sensor under different temperatures. At 25°C, the frequency upshift was 18.2kHz. At 32°C, the frequency upshift decreased to 17.4kHz. It further decreased to 16.6kHz and 15.8kHz when the temperature reached 39.6°C and 44.9°C. For higher temperatures, the noise floor of the FBAR increased, resulting in difficulties in measuring the exact UV response of the sensor.

Figure 2.11(a) shows the frequency response of the FBAR sensor to different relative humidity (RH). A two-stage process can be identified based on the different slope values (Qiu et al. 2010). At low RH (RH<50%), the resonant frequency decreased linearly with the RH and a frequency downshift of 2.2kHz per 1% RH change was observed. The RH response in this range was due to the replacement of adsorbed oxygen with water molecules on the ZnO surface (Li et al. 2009). Therefore, the density of the ZnO film increased, resulting in the decrease of the resonant frequency. At high RH (RH>50%), the resonant frequency decreased linearly with the RH and a frequency downshift of 8.5kHz per 1% RH change was obtained. With increasing RH, a discrete water layer began to form on the ZnO surface, which acted as a mass loading on the FBAR. Thus, the resonant frequency of the FBAR decreased linearly with the mass of the water accumulated on top of the resonator (Zhang and Kim 2005).

The UV (600 μW/cm^2) response of the FBAR sensor in different RH is shown in Figure 2.11(b). With 23.2% RH, a frequency upshift of 19kHz was obtained. As RH increased, the frequency upshift decreased. With 35.8% RH, the frequency upshift was 18.4kHz and it further decreased to 16.6kHz as the RH increased to 54.5%. As the RH continued to rise, the discrete water layer formed on the ZnO surface degraded the Q of the FBAR (due to the attenuation of acoustic wave in the water layer) (Qiu et al. 2010), resulting in a large noise floor which prevented measuring the exact UV response of the sensor. As mentioned above, water molecules can take the place of adsorbed oxygen on the ZnO surface. Thus, the density of the ZnO film increases at high RH. At the same time, as adsorbed oxygen is replaced by water, there is less oxygen left on the ZnO surface to be desorbed by UV. In this way, the density change induced by UV illumination decreases, resulting in a lower UV response at high RH.

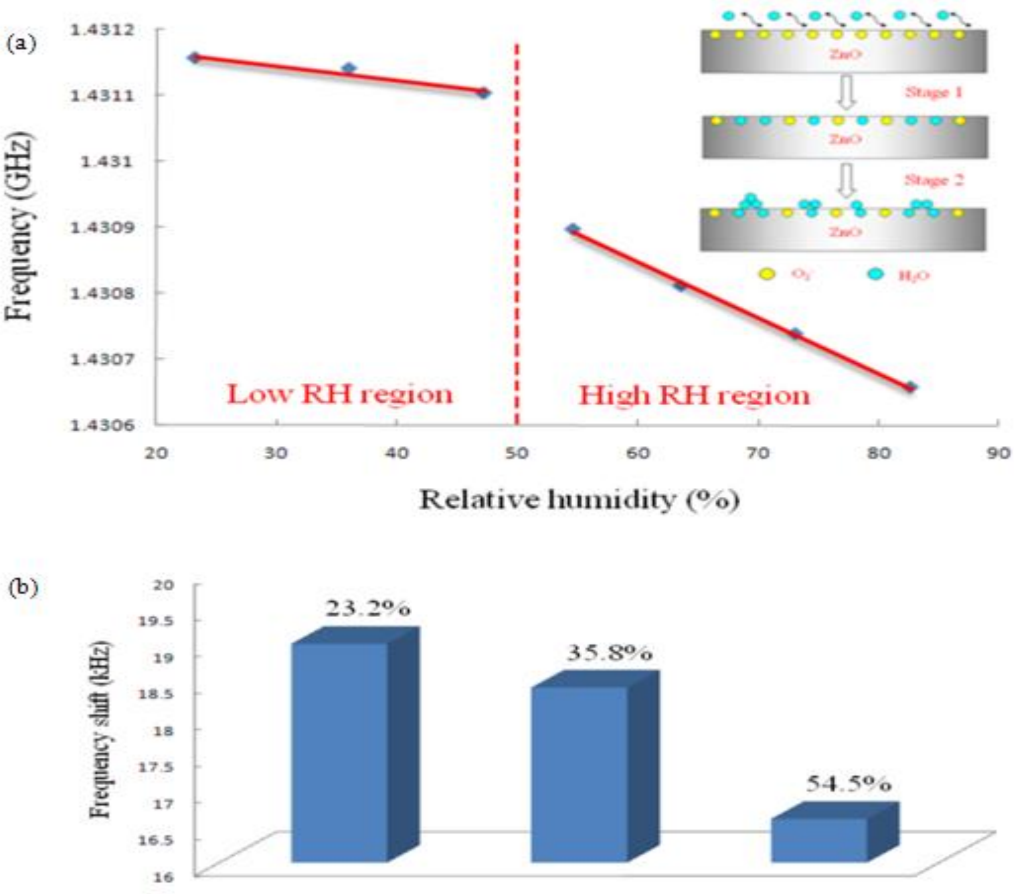

Figure 2.11 (a) The RH response of the FBAR at room temperature. Two stages can be identified. At low RH (RH<50%), a frequency downshift of 2.2kHz per 1% RH change was observed. At high RH (RH>50%), a frequency downshift of 8.5kHz per 1% RH change was obtained. The inset illustrated the mechanism of the two-stage response of the FBAR. At low RH (stage 1), the response was due to the replacement of adsorbed oxygen with water molecules on the ZnO surface. At high RH (stage 2), a discrete water layer began to form on the ZnO surface, which acted as a mass loading on the FBAR. (b) The UV (600 μW/cm^2) response of the FBAR sensor under different RH. With 23.2% RH, a frequency upshift of 19kHz was obtained. As RH increased, the frequency upshift decreased. With 35.8% RH, the frequency upshift was 18.4kHz and it further decreased to 16.6kHz as RH increased to 54.5%.

Reducing gases, such as acetone, can react with the oxygen ions on the ZnO film, and release the adsorbed oxygen (Han et al. 2007). Thus, they can affect the UV response of the FBAR.

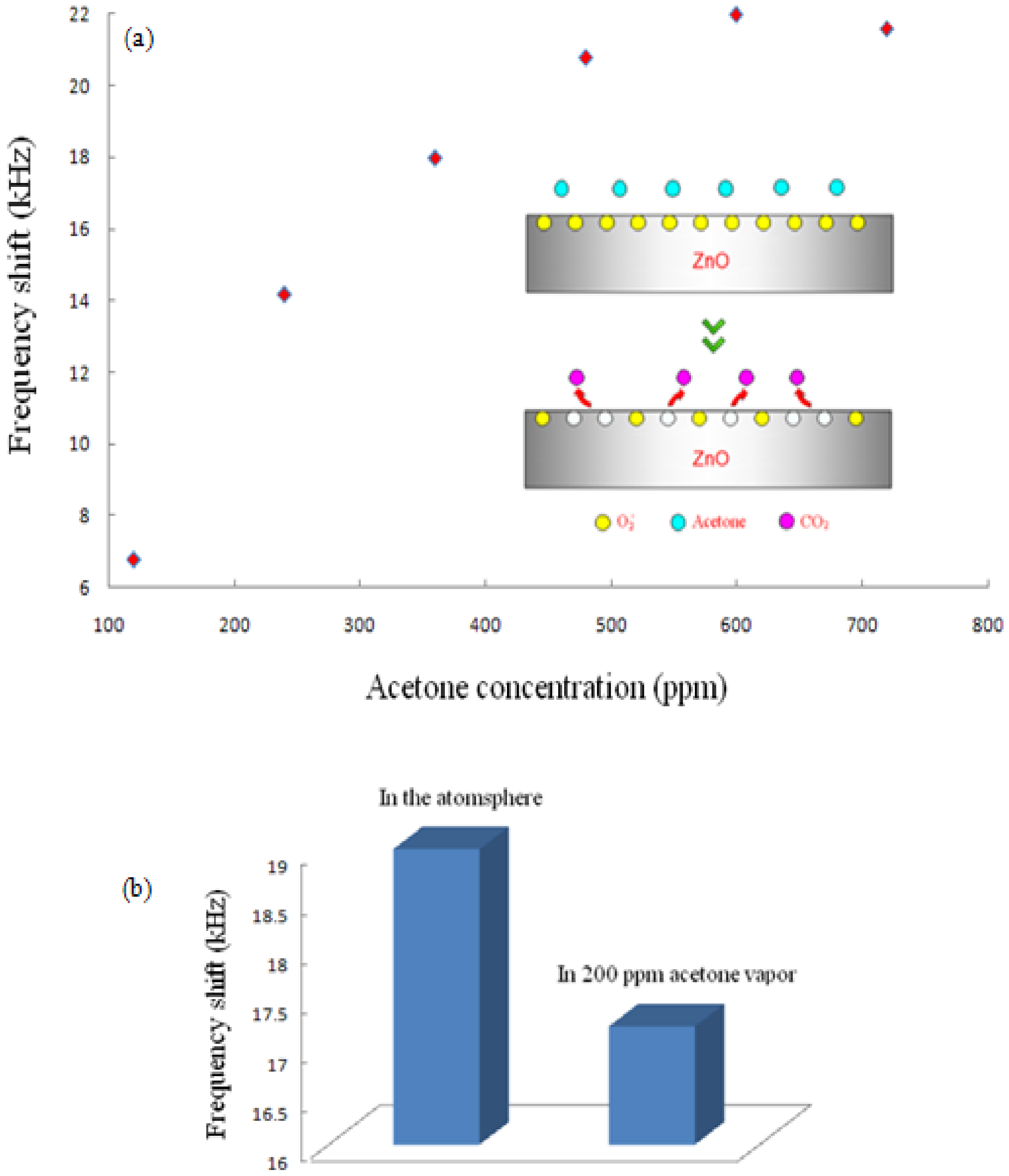

Figure 2.12 (a) FBAR's response to acetone: the resonant frequency of the FBAR increased with the acetone concentration. With 120ppm acetone, the frequency upshift was 6.8kHz. As the concentration increased to 720ppm, the frequency upshift rose to 21.6kHz, researching saturation. The inset illustrated the sensing mechanism: acetone reacts with the surface adsorbed oxygen ions on the ZnO film and releases CO_2 as a reaction product. Thus, the density of the film decreases, resulting in an increase of resonant frequency. (b) The frequency upshift of the UV illuminated FBAR sensor in the atmosphere and in 200ppm acetone vapor. It showed that in an acetone filled environment, the UV (600 μW/cm^2) response was degraded (17.2kHz compared to 19kHz in the atmosphere).

Figure 2.12(a) shows the response of the FBAR to acetone vapor. The resonant frequency of the FBAR increased with the acetone concentration. With 120ppm acetone, the frequency upshift was 6.8kHz. As the concentration increased to 720ppm, the frequency upshift rose to 21.6kHz, reaching saturation. Acetone and UV light shared a similar mechanism to upshift the frequency of the FBAR sensor (Qiu et al. 2009). It reacts with the adsorbed oxygen ions on the ZnO film surface and releases CO_2 as a reaction product (Sahay 2005). Thus, acetone can cause the density of the ZnO film to decrease and result in an increase of resonant frequency. In the presence of acetone, it reacted with some surface adsorbed oxygen ions on the ZnO film. Therefore, when UV light was incident, there was less oxygen left on the surface to be desorbed by UV. Thus, the density change will become smaller with the same UV intensity, followed by a smaller frequency upshift. Figure 2.12(b) shows the UV response of the FBAR sensor in the atmosphere and in 200ppm acetone vapor. It illustrated that in an acetone filled environment, the UV (600 $\mu W/cm^2$) response was degraded (17.2kHz compared to 19kHz in the atmosphere). Similar effects can be expected with other reducing gases, such as carbon monoxide.

2.6 Summary

A low intensity UV sensor was developed using a ZnO based film bulk acoustic resonator. A frequency upshift was observed upon UV illumination on the ZnO film. The output of the sensor was a frequency change, which was suitable for integration with a wireless sensor network. The working principle of the FBAR UV sensor was attributed to the density decrease of ZnO with incident

UV light. Moreover, experiment results with acetone and ozone supported this mechanism and demonstrated the capability of FBAR to be applied as a potential gas sensor.

The effects of temperature, relative humidity and reducing gases on the UV response of ZnO based FBAR were investigated. As temperature and relative humidity increased, the UV response of the FBAR degraded. Reducing gases, such as acetone, were also able to degrade the UV sensitivity of the FBAR. The mechanisms behind these effects were discussed. In future applications, a vacuum package may need to be pursued for the FBAR UV sensor to eliminate the influence of these environmental factors.

Chapter 3

MONITORING RELATIVE HUMIDITY USING FILM BULK ACOUSTIC RESONATOR

Relative humidity (RH) is a very common parameter in our environment. It is essential not only for human comfort, but also for a broad spectrum of industries and technologies. There is a substantial interest in the development of RH sensors for applications in monitoring moisture level at home, in clean rooms, cryogenic processes, medical and food science, and so on. Table 3.1 summarizes the widespread applications of RH sensors.

Table 3.1 Applications of relative humidity sensors.

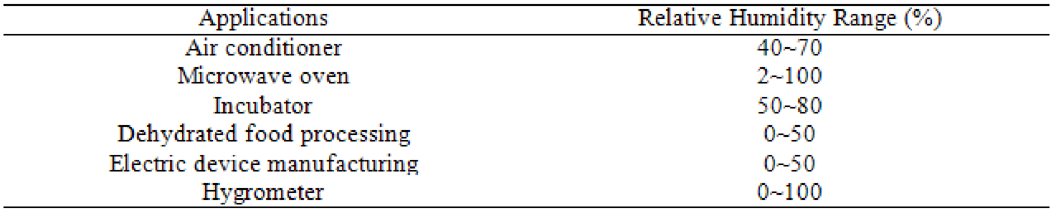

Applications	Relative Humidity Range (%)
Air conditioner	40~70
Microwave oven	2~100
Incubator	50~80
Dehydrated food processing	0~50
Electric device manufacturing	0~50
Hygrometer	0~100

The requirements that RH sensors need to meet for various applications are as follows: (1) a good sensitivity over a wide range of relative humidity and temperature, (2) a short response time, (3) good reproducibility and small hysteresis, (4) good durability and long life time, (5) resistance against contaminants, (6) negligible temperature dependence, and (7) low cost (Rittersma 2002). Today, roughly 75% of the RH sensors in the market are based on the capacitive principle (Scholz 1992). Meanwhile, there are plenty of other RH sensors, such as resistive sensors (Faia et al. 2004) and surface acoustic sensors (Penza and Cassano 2000). Capacitive sensors are based on dielectric parameter change of thin films upon moisture uptaking. The properties of these sensors depend on the film material and the electrode geometry. On the other hand, resistive sensors can transfer the RH variation into an impedance change, which can be measured by a simple circuit. Another alternative is monitoring RH with gravimetric effect using surface acoustic wave resonators (SAW). Thin plates of piezoelectric material were coated with a hygroscopic layer (usually a polymer layer). The resonant frequency of the SAW shifted as moisture was absorbed onto the surface. Thus, the RH can be measured via the frequency change.

3.1 Design and fabrication of FBAR RH sensor

The schematic structure of the FBAR RH sensor is shown in Figure 3.1. The FBAR was fabricated on top of a SiN diaphragm (0.6 µm thick). A sputtered ZnO film (1.2 µm) acted both as the RH sensitive layer and the piezoelectric actuation layer for the FBAR sensor. The ZnO film was characterized by X-ray diffraction (XRD) using Cu K_α radiation (Fig. 3.1). Only the Bragg reflection corresponding to (002) planes was observed, indicating that the film had preferred orientation along the wurtzite C axis, normal to the silicon substrate. The top and bottom electrodes were made of Cr/Au (0.02 µm/0.2 µm) and Al (0.2 µm), respectively. The fabrication process of the FBAR RH sensor was similar to that of the FBAR UV sensor.

3.2 Experiment setup

The sensor was encapsulated in a chamber, in which RH was controlled by an ultrasonic humidifier (Guardian Technologies, Mentor, OH) and measured by a HH314A humidity temperature meter. FBAR was tested on a probe station with Ground-Signal-Ground 150 micron pitch probes. The calibration was carried out with an impedance standard substrate using a short-open-load (SOL) method. The resonant frequency of the FBAR was monitored with an Agilent E5071C network analyzer and recorded by a LabVIEW program. It had a noise floor of 0.7ppm at 1.4 GHz, which was suitable for integration with a wireless sensor network. The quality factor (Q) of the FBAR was between 530 and 550. A versatile hand-held ultraviolet lamp (365nm) was used as the UV source. A UVX digital ultraviolet intensity meter was applied to calibrate the UV power received by the FBAR.

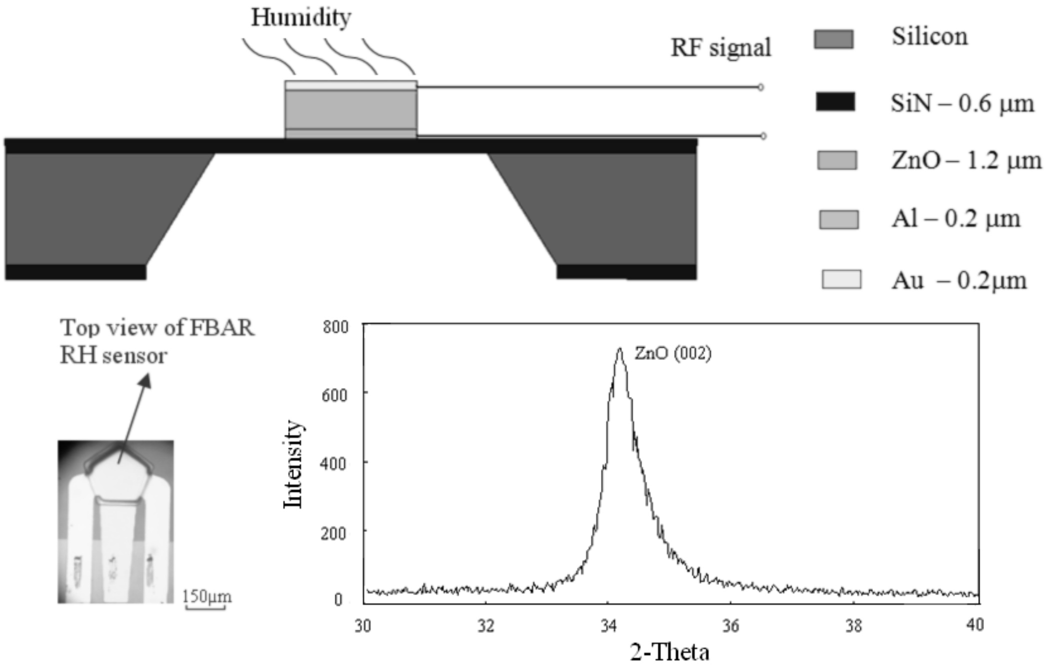

Figure 3.1 Schematic cross-sectional structure (not drawn to scale) of the FBAR RH sensor with a photograph of the top view of a fabricated device on the left and an XRD trace of the ZnO film illustrating that it had (002) crystal orientation on the right.

3.3 Testing results in the low RH region

The RH response of the FBAR sensor at room temperature is shown in Figure 3.2. A two-stage process can be identified based on the different slope values. At low RH (RH<50%), the resonant frequency decreased linearly with the

RH and a frequency downshift of 2.2kHz per 1% RH change was observed. With the current noise floor, the detection limit was around 0.45% RH. The RH response in this range was due to the replacement of adsorbed oxygen with water molecules on the ZnO surface (Li et al. 2009). Therefore, the density of the ZnO film increased. The resonant frequency of the FBAR can be determined from the following two equations: $v=(E/\rho)^{1/2}$ and $f=v/2d$, where E, ρ and d are the elastic constant, density and thickness of the ZnO film, respectively. v is the acoustic velocity within the ZnO film and f is the resonant frequency of the FBAR. As the density of the ZnO film increased with RH, the acoustic velocity decreased, resulting in the decrease of the resonant frequency.

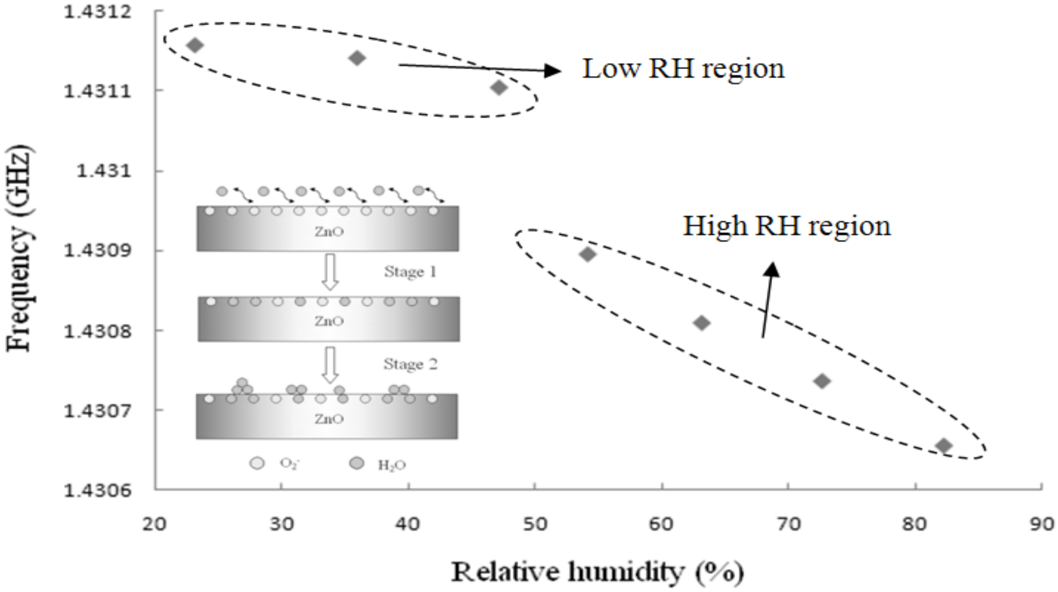

Figure 3.2 The RH response of the FBAR at room temperature. Two stages can be identified. At low RH (RH<50%), a frequency downshift of 2.2kHz per 1% RH change was observed. At high RH (RH>50%), a frequency downshift of 8.5kHz per 1% RH change was obtained. The inset illustrated the mechanism of the two-stage response of the FBAR. At low RH (stage 1), the response was due to the replacement of adsorbed oxygen with water molecules on the ZnO surface. At high RH (stage 2), a discrete water layer began to form on the ZnO surface, which acted as a mass loading on the FBAR.

3.4 Analytical model for the low RH region

It has been known that the electric resistance of a semiconductor gas sensor exposed to a target gas (partial pressure P) is proportional to P^n where n is a constant fairly specific to the kind of target gas (power law). Yamazoe and Shimanoe (2008) established a theoretical basis for the power law combining a depletion theory of the semiconductor, which deals with the distribution of electrons between surface state and bulk, with the dynamics of adsorption and/or reactions of gases on the surface, which is responsible for accumulation or reduction of surface charges. By extending their work to address the density change of the semiconductor gas sensor, a theoretical model for the RH response of the ZnO film based FBAR was developed for the low RH region (RH<50%).

According to Yamazoe and Shimanoe (2008), the density of conduction electrons at the surface $[e]$ can be expressed as:

$$[e] = N_d \exp(-\frac{m^2}{2}) \qquad \text{(Eq. 3.1)}$$

where N_d is the density of donors and m is the reduced depletion depth. Using the double Schottky barrier model, the amount of adsorption/desorption of oxygen at each grain-boundary is proportional to $[e]$. Thus the relative density change, $\Delta\rho$, induced by adsorption/desorption of oxygen is proportional to $[e]$.

Meanwhile, the frequency shift Δf can be formulated as:

$$\Delta f = \frac{1}{2d}(\sqrt{\frac{E}{\rho+\Delta\rho}} - \sqrt{\frac{E}{\rho}}) = \frac{\sqrt{E}}{2d}\frac{\left(1-\sqrt{1+\frac{\Delta\rho}{\rho}}\right)}{\sqrt{\rho+\Delta\rho}} \qquad \text{(Eq. 3.2)}$$

In the equation above, ρ » $\Delta\rho$. In this way,

$$\Delta f \approx \frac{\sqrt{E}}{2d}\cdot\frac{\left(1-1-\frac{1}{2}\frac{\Delta\rho}{\rho}\right)}{\sqrt{\rho}} = -\frac{\sqrt{E}}{4d\rho\sqrt{\rho}}\Delta\rho \qquad \text{(Eq. 3.3)}$$

Therefore the frequency shift Δf is proportional to $\Delta\rho$ and thus, it is also proportional to $[e]$.

At room temperature, oxygen is adsorbed as O^-_2 on the ZnO surface (Takata et al.1976).

$$O_2 + e \underset{k_{-1}}{\overset{k_1}{\rightleftarrows}} O_2^- \qquad \text{(Eq. 3.4)}$$

Here e stands for a conduction electron at the surface, and k_1 and k_{-1} are the rate constants of forward and reverse reactions, respectively. The rate of accumulation of O^-_2 is given by

$$\frac{d[O_2^-]}{dt} = k_1 PO_2[e] - k_{-1}[O_2^-] \qquad \text{(Eq. 3.5)}$$

Here the brackets mean the density of O^-_2 per unit area or that of electrons per unit volume, t is time, and PO_2 is the partial pressure of oxygen. At equilibrium, the rate is zero, thus,

$$k_{o1} PO_2[e] = [O_2^-] \qquad \text{(Eq. 3.6)}$$

$$k_{o1} = \frac{k_1}{k_{-1}} \qquad \text{(Eq. 3.7)}$$

where k_{o1} is the equilibrium constant of oxygen adsorption.

Assuming that there are no electron-trapping sites other than O^-_2 on the surface, then O^-_2 ions would be solely responsible for the surface charge density, that is,

$$[O_2^-] = N_d\omega \qquad \text{(Eq. 3.8)}$$

Here ω is the depletion depth and $\omega = mL_D$, where L_D is the Debye length (Yamazoe and Shimanoe 2008).

Insert Eq. 3.1 and 3.8 into 3.6 yields,

$$k_{o1}PO_2 \exp(-\frac{m^2}{2}) = \omega \qquad \text{(Eq. 3.9)}$$

As mentioned above, water molecules will take the place of the adsorbed oxygen on the ZnO surface (Li et al. 2009). Two water molecules can dissociate and become chemisorbed in the ZnO film (Li et al. 2009; Korotchenkov et al. 1999). At equilibrium,

$$k_{o1}PO_2[e] = [O_2^-] + k_{o2}PH_2O[O_2^-] \qquad \text{(Eq. 3.10)}$$

$$k_{o2} = \frac{k_2}{k_{-1}} \qquad \text{(Eq. 3.11)}$$

where k_2 is the rate constant of water absorption and PH_2O is the partial pressure of water vapor, which is proportional to RH at a certain temperature.

From the discussion above, the power law exponent n, defined as $d(\log\Delta f)/d(\log PH_2O)$, is obtained,

$$\frac{d(\log\Delta f)}{d(\log PH_2O)} = 1 - \frac{1}{1+m^2} \qquad \text{(Eq. 3.12)}$$

where m is sufficiently large under usual conditions (Yamazoe and Shimanoe 2008). Thus n is around 1, which can be used to explain the linear relationship between the resonant frequency and the RH in Figure 3.2 in the low RH region.

3.5 Testing results in the high RH region

In Figure 3.2, at high RH (RH>50%), the resonant frequency decreased linearly with the RH and a frequency downshift of 8.5kHz per 1% RH change was obtained, corresponding to a detection limit of around 0.12% RH. With increasing RH, a discrete water layer began to form on the ZnO surface, which acted as a mass loading on the FBAR. Thus the resonant frequency of the FBAR decreased linearly with the mass of the water accumulated on top of the resonator (Zhang and Kim 2005). This can also be observed from the Q response of the FBAR with increasing RH (Fig. 3.3(a)).

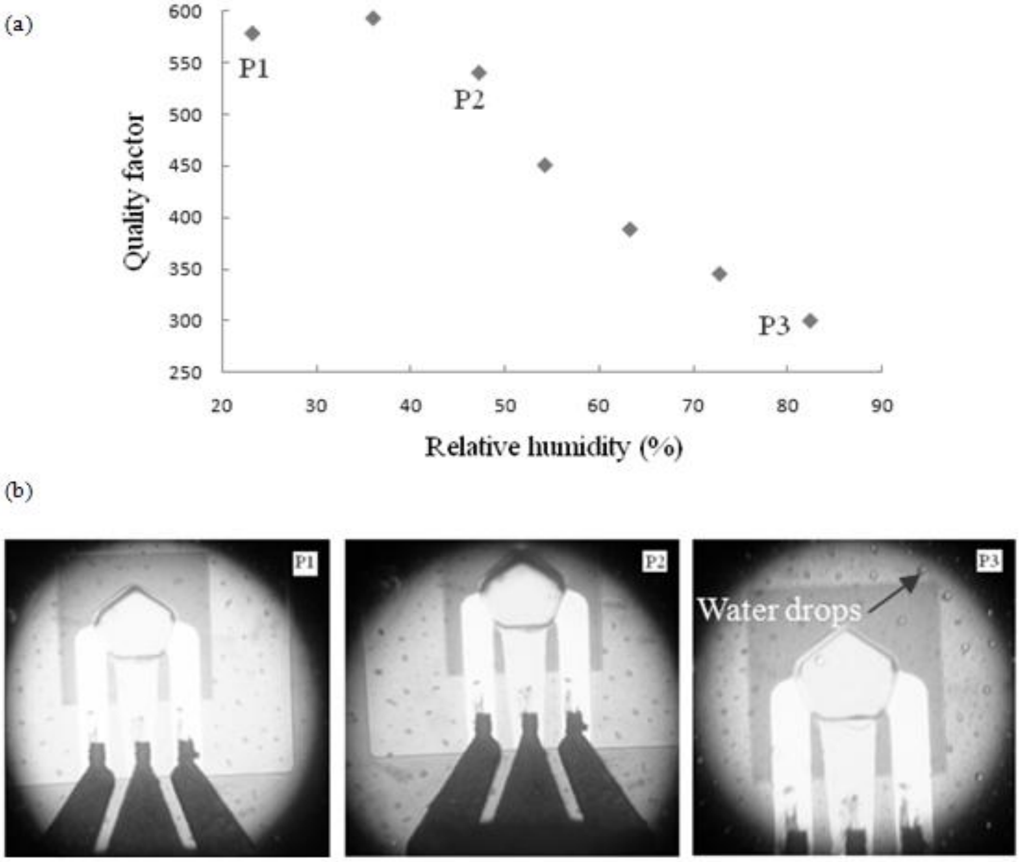

Figure 3.3 (a) The response of FBAR's Q vs. RH. Two different stages can be identified. At RH lower than 50%, Q changed less than 10%. However, at RH higher than 50%, Q decreased quickly with humidity. (b) The photographs of the FBAR under different RH. P1: 23.2%; P2: 47.2%; P3: 82.3%. The corresponding positions of these three humidity values are indicated in the figure of the Q response of the FBAR sensor shown in (a). It was clear that at RH around 82.3% there were small water drops condensed on the device.

At RH higher than 50%, Q decreased quickly with humidity, while at RH lower than 50%, Q changed less than 10%. These results indicated that water layer formed on the ZnO surface when RH was higher than 50%, thus attenuating acoustic wave, resulting in a lower Q. Figure 3.3(b) shows the photographs of the FBAR under different RH. It was clear that at RH higher than 50% (P3) there were small water drops formed on the device.

3.6 Analytical model for the high RH region

The Butterworth-Van Dyke (BVD) equivalent circuit of FBAR with and without liquid loading is shown in Figure 3.4, where C_o, L_m, C_m, and R_m are the clamped capacitance between the top and bottom electrodes, motional inductance, motional capacitance, and motional resistance of the resonator, respectively. R_2 and L_2 are associated with acoustic energy loss and mass loading by the liquid, respectively (Zhang and Kim 2005).

In the equivalent circuit, the circuit elements are related to the physical parameters of the resonator and the added liquid by

$$f_s = \frac{1}{2\pi\sqrt{L_m C_m}} \tag{Eq. 3.13}$$

$$f_p = \frac{1}{2\pi\sqrt{L_m \frac{C_m C_o}{C_m + C_o}}} \tag{Eq. 3.14}$$

$$L_m = \frac{1}{4\pi^2 f_p{}^2 C'} \tag{Eq. 3.15}$$

$$C' = \frac{C_m C_o}{C_m + C_o} \tag{Eq. 3.16}$$

$$f'_p = \frac{1}{2\pi\sqrt{(L_m + \Delta L)\frac{C_m C_o}{C_m + C_o}}} \tag{Eq. 3.17}$$

$$\Delta L = L_2 \tag{Eq. 3.18}$$

$$L_2 = \frac{2 L_m \rho_1 d_1}{\rho_0 d_0} \tag{Eq. 3.19}$$

where f_s and f_p are the series and parallel resonant frequency of the FBAR. f'_p is the parallel resonant frequency with the liquid loading. ρ_0, d_0, ρ_1, and d_1 are the density of the piezoelectric layer, the thickness of the piezoelectric layer, the density of the added liquid and the thickness of the added liquid, respectively (Zhang and Kim 2005).

From the equations above (similar results can be obtained for f_s),

$$\Delta L = \frac{1}{4\pi^2 C'} \frac{f_p^2 - f'^2_p}{f_p^2 f'^2_p} \approx \frac{1}{4\pi^2 C'} \frac{2\Delta f_p}{f_p f'^2_p} \qquad \text{(Eq. 3.20)}$$

$$\Delta f_p = f_p - f'_p \qquad \text{(Eq. 3.21)}$$

$$\frac{\Delta f_p}{f_p} = \frac{\Delta L}{2} \frac{1}{L_m + \Delta L} \approx \frac{\Delta L}{2L_m} = \frac{\rho_1 d_1}{\rho_0 d_0} \qquad \text{(Eq. 3.22)}$$

Eq. 3.22 indicates that the resonant frequency shift of an acoustic resonator is linearly related to the mass of a material added on the top of the resonator. Assuming the mass of the water accumulated on the FBAR is proportional to the RH, a linear response of the FBAR can be expected in the high RH region, which is in agreement with the experiment results.

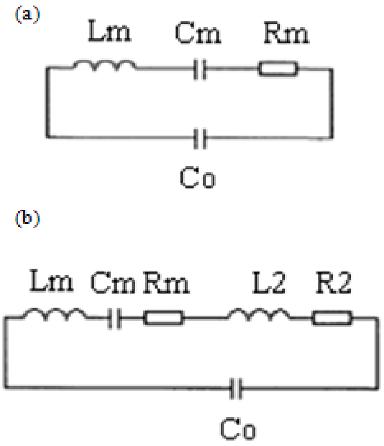

Figure 3.4 Butterworth-Van Dyke (BVD) equivalent circuits: (a) FBAR without liquid loading and (b) FBAR with liquid loading.

3.7 Influence of ultraviolet on the performance of FBAR RH sensor

Previous study showed that the absorption of water on the ZnO surface can be enhanced with ultraviolet illumination (Sun et al. 2001). Thus UV may improve the RH response of the ZnO based FBAR. The RH response of the FBAR under UV (600 μW/cm^2) is shown in Figure 3.5. It was also a two-stage response. At low RH (RH<50%), a frequency downshift of 3.4kHz per 1% RH change was observed with a detection limit of 0.3% RH. It was demonstrated that in this region UV can enhance the absorption of water on the ZnO surface, resulting in a higher sensitivity.

While at high RH (RH>50%), a frequency downshift of 5.7kHz per 1% RH change was obtained, corresponding to a detection limit of around 0.18% RH. This value was degraded compared with the detection limit in the UV absent case (around 0.12% RH). It can be explained as follows: when there is UV illumination on the ZnO film, the wettability of the surface will be enhanced, resulting in a more hydrophilic surface (Sun et al. 2001; Feng et al. 2004; Liu et al. 2004; Han and Gao 2009; Miyauchi et al. 2005). Therefore under UV illumination, due to the improved hydrophilicity, the water layer on the FBAR distributed more uniformly (Fig. 3.5) with smoother surface and less mass loading effect compared with the UV absent case, where the ZnO surface was less hydrophilic. The frequency shift of the FBAR due to additional mass loading can be estimated from Eq. 3.22. With a smoother surface, the effective thickness of the water layer on the ZnO film under UV illumination was smaller compared with the UV absent case, resulting in a reduced frequency shift. Thus, the RH response under UV was smaller in this region.

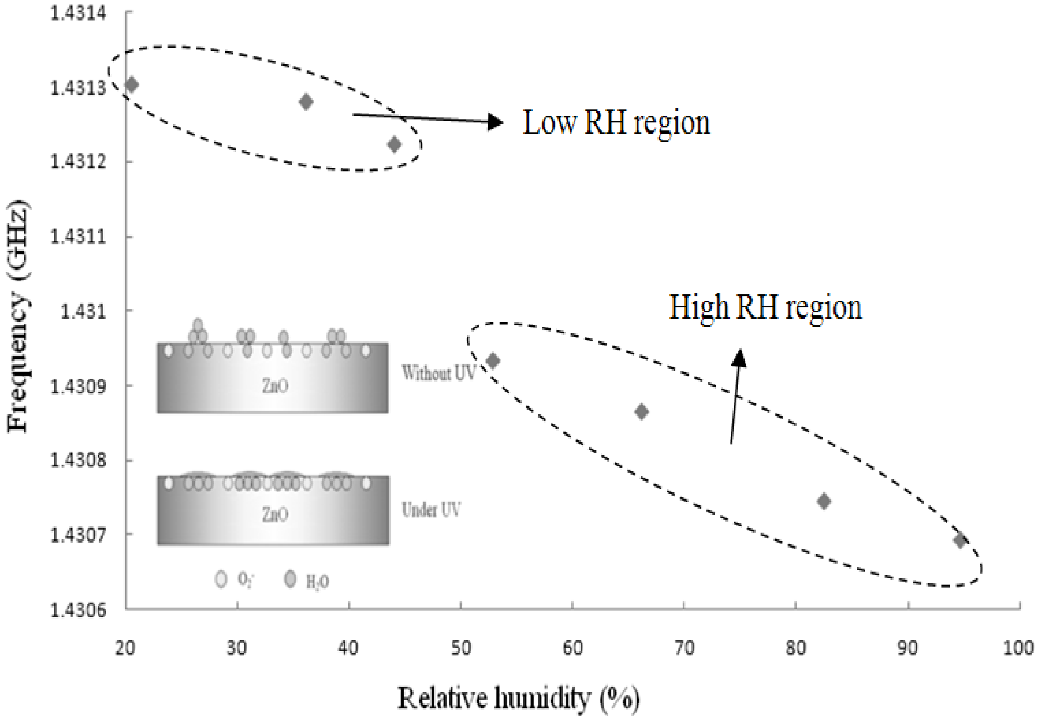

Figure 3.5 The RH response of the FBAR under UV (600 μW/cm^2) illumination. It was a two-stage response. At low RH (RH<50%), a frequency downshift of 3.4kHz per 1% RH change was observed. It was demonstrated that in this region UV can enhance the absorption of water on the ZnO surface, resulting in a higher sensitivity. While at high RH (RH>50%), a frequency downshift of 5.7kHz per 1% RH change was obtained. This value was smaller compared with the UV absent case. The inset illustrated the sensing mechanism of the FBAR sensor at high RH region in the presence and absence of UV illumination. When there is UV illumination on the ZnO film, the wettability of the surface will be enhanced, resulting in a more hydrophilic surface. Therefore under UV illumination, due to the improved hydrophilicity, the water layer on the FBAR distributed more uniformly with smoother surface and less mass loading effect compared with the UV absent case, where the ZnO surface was less hydrophilic.

This was in agreement with the measured Q response of RH under UV illumination (Fig. 3.6). Q decreased more slowly at high RH in this case, due to the reduced attenuation of acoustic wave with the smoother water layer.

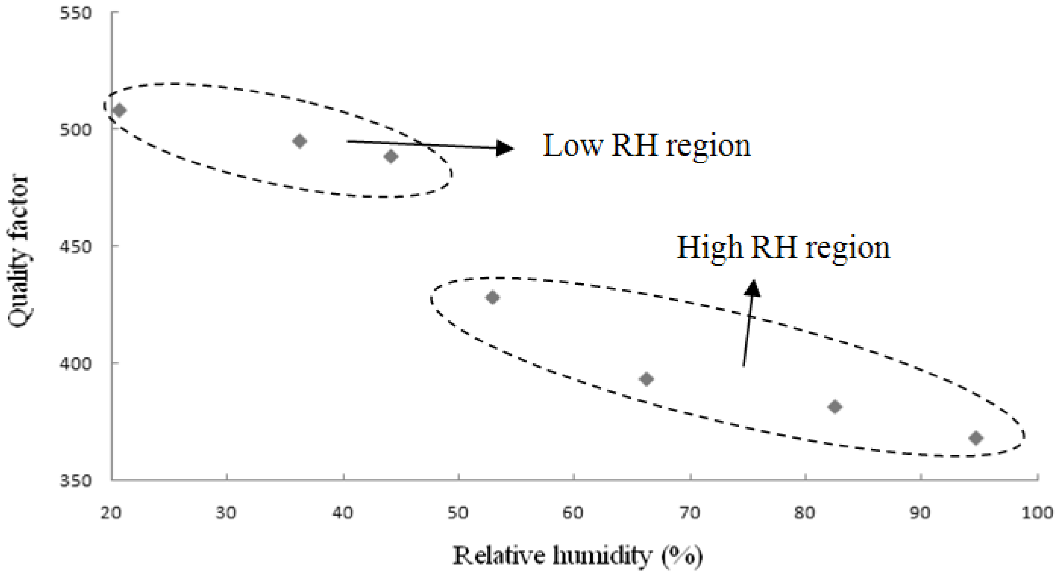

Figure 3.6 The response of FBAR's Q vs. relative humidity under UV (600 μW/cm^2) illumination. At RH higher than 50%, Q decreased more slowly compared with the UV absent case.

3.8 Summary

A RH sensor was developed using ZnO based FBAR. The resonant frequency of the FBAR decreased linearly in a two-stage manner as the RH increased in the environment. For low RH (RH<50%), a frequency downshift of 2.2kHz per 1% RH change was observed. This effect was attributed to water molecules replacing the adsorbed oxygen on the ZnO surface, thus increasing the density of the film. While for high RH (RH>50%), a frequency downshift of 8.5kHz per 1% RH change was obtained, which was due to the mass loading effect of the water layers formed on the ZnO surface. UV light was applied to study its effects on the humidity sensing performance of the FBAR. UV can enhance the sensitivity at low RH (frequency downshift increased to 3.4kHz per 1% RH change), while degrading the sensitivity at high RH (frequency downshift decreased to 5.7kHz per 1% RH change). The mechanisms of both the RH response and the influence of UV illumination were investigated. This study has proven the feasibility of monitoring RH with ZnO film based FBAR.

Chapter 4

ACETONE AND ETHANOL SENSOR BASED ON FILM BULK ACOUSTIC RESONATOR

4.1 FBAR acetone sensor

The analysis of exhaled air can provide information on the concentration of acetone and other ketone bodies in an organism and serve as an express noninvasive diagnosis of ketosis. Several methods have been utilized to analyze trace compounds in the human breath (Cao and Duan 2007). The most common ones are gas chromatography (Sanchez and Sacks 2003), mass spectrometry (Mukhopadhyay 2004), and ion mobility spectrometry (Lord et al. 2002). For the gas chromatography method, water vapor can damage its column, resulting in the requirement of pretreatment of the breath (Cheng and Lee 1999). Selected ion flow tube mass spectrometry (smith and Spanel 2005) has shown great potential in real-time concentration monitoring of acetone and ethanol in human breath. A major advantage is its high selectivity, sufficient sensitivity, and low limit of detection. However, its high cost and limited portability still hinder its application as standard diagnostic tools (Toda et al. 2006). Semiconductor sensors are another popular choice for acetone detectors nowadays. These simple devices have low fabrication cost, offer high miniaturization potential, sensitivity, and sufficient limit of detection (Eranna et al. 2004). However, they cannot distinguish acetone vapors from ethanol vapors effectively. Therefore, ketosis may be wrongly taken for drunkenness. Plenty of research has been conducted to solve the selectivity problem. Kim et al. (2007) used combinational solution deposition to prepare

SnO_2-ZnO thin film sensors which possessed different sensitivity for acetone and ethanol. Righettoni et al. (2010) developed a Si-doped WO_3 nanoparticle film based acetone sensor with minimum response to ethanol. However, as both gases can reduce the resistivity of the sensors, the selectivity was still not as high as desirable. At the same time, the sensors are generally operated at elevated temperatures, which results in large power consumption.

4.1.1 Design and fabrication of FBAR acetone sensor

The schematic structure of the FBAR acetone sensor is shown in Figure 4.1. The device was fabricated on top of a SiN (0.6 µm) diaphragm. A sputtered ZnO film (1.2 µm) was used both as the acetone sensitive layer and the piezoelectric actuation layer for the FBAR sensor. The top and bottom electrodes were made of Cr/Au (0.02 µm/0.2 µm) and Al (0.2 µm), respectively. The fabrication process of the FBAR acetone sensor was similar to that of the FBAR UV sensor. The resulting Cr/Au electrode cannot form a conformal coating on the ZnO due to the surface roughness of the film. Accordingly, there were discontinuities in the top electrode that can allow gases to reach the ZnO.

4.1.2 Experiment setup

The sensor was encapsulated in a chamber to control the gas concentration. It was tested on a probe station with Ground-Signal-Ground 150 micron pitch probes. The calibration was carried out with an impedance standard substrate using a short-open-load (SOL) method. The resonant frequency of the FBAR was monitored with an Agilent E5071C network analyzer and recorded using a LabVIEW program. The measured resonant frequency of the FBAR was around

1.4 GHz with a quality factor of about 550. The concentration of acetone was calibrated by gas detection pump and tubes (Draeger Safety Inc, Pittsburgh, PA).

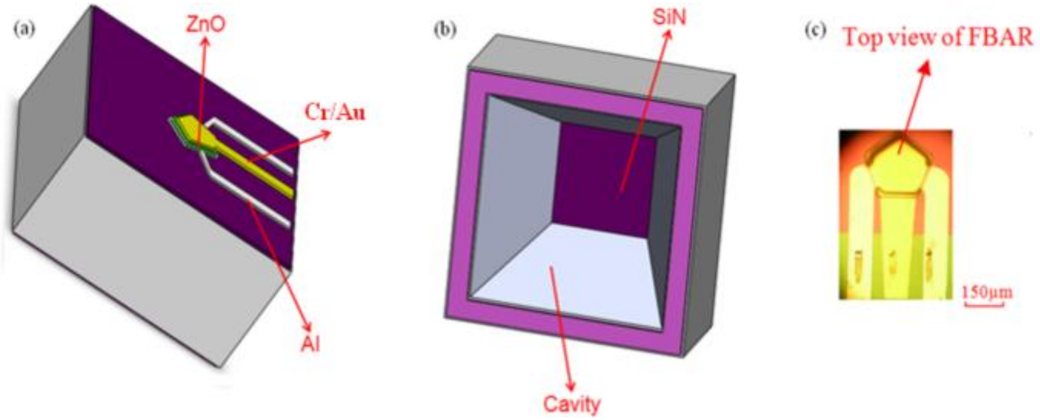

Figure 4.1 Schematic structure of the FBAR sensor: (a) top view, (b) bottom view and (c) a photograph of the top view of a fabricated device.

4.1.3 Acetone response of FBAR

Figure 4.2 illustrates the relationship between the shift of resonant frequency and the acetone concentration. The resonant frequency of the FBAR increased as the concentration of acetone increased. It consisted of a linear region and a saturation region. For 25ppm acetone, the frequency upshift was 7kHz. As the concentration increased to 220ppm, the frequency upshift rose to 30kHz, reaching saturation. With the current noise floor of the FBAR, the detection limit for acetone was about 4ppm.

4.1.4 Acetone sensing mechanism

The resonant frequency of the FBAR can be determined from the following two equations:

$$v = \sqrt{\frac{E}{\rho}} \qquad \text{(Eq. 4.1)}$$

$$f = \frac{v}{2d} \qquad \text{(Eq. 4.2)}$$

where E, ρ and d are the elastic modulus, density and thickness of the ZnO film, respectively. The variable v represents the acoustic velocity within the ZnO film and f is the resonant frequency of the FBAR.

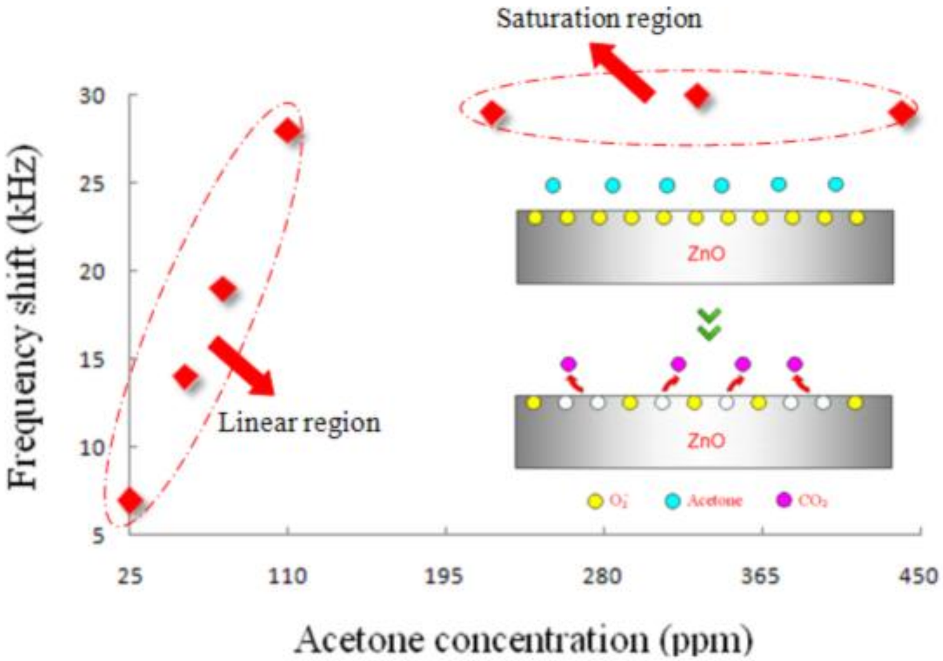

Figure 4.2 The relationship between the shift of resonant frequency and the acetone concentration. It consisted of a linear region and a saturation region. The inset illustrated the sensing mechanism: acetone reacts with the surface adsorbed oxygen ions on the ZnO film and releases CO_2 as a reaction product. Thus, the density of the film decreases, resulting in an increase of resonant frequency.

Acetone reacts with the adsorbed oxygen ions on the ZnO surface and releases CO_2 as a reaction product (Sahay 2005). Thus, it can cause the density of the ZnO film to decrease and result in an increase of the acoustic velocity (Qiu et al. 2009). Therefore, the resonant frequency will increase accordingly. The reaction between acetone and the adsorbed oxygen ions is as follow (Sahay 2005).

$$CH_3COCH_3 + O_2^- \rightarrow CH_3^+ + CH_3O^- + CO_2 + e^- \qquad \text{(Eq. 4.3)}$$

4.1.5 Analytical model for acetone response

It has been known that the electric resistance of a semiconductor gas sensor exposed to a target gas (partial pressure P) is proportional to P^n where n is a constant fairly specific to the kind of target gas (power law). Yamazoe and Shimanoe (2008) established a theoretical basis to the power law combining a depletion theory of semiconductor, which deals with the distribution of electrons between surface state and bulk, with the dynamics of adsorption and/or reactions of gases on the surface, which is responsible for accumulation or reduction of surface charges. By extending their work to address the density change of the semiconductor gas sensor, a theoretical model for the acetone response of the ZnO film based FBAR was developed.

According to Yamazoe and Shimanoe (2008), the density of conduction electrons at the surface $[e]$ can be expressed as:

$$[e] = N_d \exp(-\frac{m^2}{2}) \qquad \text{(Eq. 4.4)}$$

where N_d is the density of donors and m is the reduced depletion depth. Using the double Schottky barrier model, the amount of adsorption/desorption of oxygen at each grain-boundary is proportional to $[e]$. Thus the relative density change, $\Delta\rho$, induced by adsorption/desorption of oxygen is proportional to $[e]$.

Meanwhile, the frequency shift Δf can be formulated as:

$$\Delta f = \frac{1}{2d}\left(\sqrt{\frac{E}{\rho - \Delta\rho}} - \sqrt{\frac{E}{\rho}}\right) = \frac{\sqrt{E}}{2d}\frac{(1-\sqrt{1-\frac{\Delta\rho}{\rho}})}{\sqrt{\rho-\Delta\rho}} \qquad \text{(Eq. 4.5)}$$

In the equation above, *ρ » Δρ*. In this way,

$$\Delta f \approx \frac{\sqrt{E}}{2d}\cdot\frac{\left(1-1+\frac{1}{2}\frac{\Delta\rho}{\rho}\right)}{\sqrt{\rho}} = \frac{\sqrt{E}}{4d\rho\sqrt{\rho}}\Delta\rho \qquad \text{(Eq. 4.6)}$$

Therefore the frequency shift *Δf* is proportional to *Δρ* and thus, it is also proportional to [*e*].

At room temperature, oxygen is adsorbed as O^-_2on the ZnO surface (Takata et al. 1976).

$$O_2 + e \underset{k_{-1}}{\overset{k_1}{\rightleftarrows}} O_2^- \qquad \text{(Eq. 4.7)}$$

Here *e* stands for a conduction electron at the surface, and k_1 and k_{-1} are the rate constants of forward and reverse reactions, respectively. The rate of accumulation of O^-_2 is given by

$$\frac{d[O_2^-]}{dt} = k_1 PO_2[e] - k_{-1}[O_2^-] \qquad \text{(Eq. 4.8)}$$

Here the brackets mean the density of O^-_2 per unit area or that of electrons per unit volume, *t* is time, and PO_2 is the partial pressure of oxygen. At equilibrium, the rate is zero, thus,

$$k_{o1} PO_2[e] = [O_2^-] \qquad \text{(Eq. 4.9)}$$

$$k_{o1} = \frac{k_1}{k_{-1}} \qquad \text{(Eq. 4.10)}$$

where k_{o1} is the equilibrium constant of oxygen adsorption.

Assuming that there are no electron-trapping sites other than O^-_2 on the surface, then O^-_2 ions would be solely responsible for the surface charge density, that is,

$$[O_2^-] = N_d \omega \qquad \text{(Eq. 4.11)}$$

Here ω is the depletion depth and $\omega = mL_D$, where L_D is the Debye length (Yamazoe and Shimanoe 2008).

Insert Eq. 4.4 and 4.11 into 4.9 yields,

$$k_{o1} PO_2 \exp(-\frac{m^2}{2}) = \omega \qquad \text{(Eq. 4.12)}$$

For the reaction between O^-_2 and acetone, at equilibrium,

$$k_{o1} PO_2 [e] = [O_2^-] + k_{a1} Pacetone [O_2^-] \qquad \text{(Eq. 4.13)}$$

$$k_{a1} = \frac{k_2}{k_{-1}} \qquad \text{(Eq. 4.14)}$$

where k_2 is the rate constant of the reaction between O^-_2 and acetone and *Pacetone* is the partial pressure of acetone.

From the discussion above, the power law exponent *n*, defined as $d(\log\Delta f)/d(\log Pacetone)$, is obtained,

$$\frac{d(\log \Delta f)}{d(\log Pacetone)} = 1 - \frac{1}{1+m^2} \qquad \text{(Eq. 4.15)}$$

where *m* is sufficiently large under usual conditions (Yamazoe and Shimanoe 2008). Thus *n* is around 1, which can be used to explain the linear region of the acetone response (Fig. 4.3).

4.2 FBAR ethanol sensor

Driving under the influence of alcohol is a serious traffic violation and this kind of deviant behavior causes many accidents and deaths on the highway. The breath alcohol analyzers are usually used as a quick and reliable screening device for the sobriety checkpoint. Acetone has been generally considered the only endogenous volatile organic compound that could be considered a potential interfering substance in breath alcohol analysis (Gullberg and Logan 2006). It presents in the breath of normal person or in increased concentrations as the result of prolonged fasting, use of ketogenic diets, or diabetes.

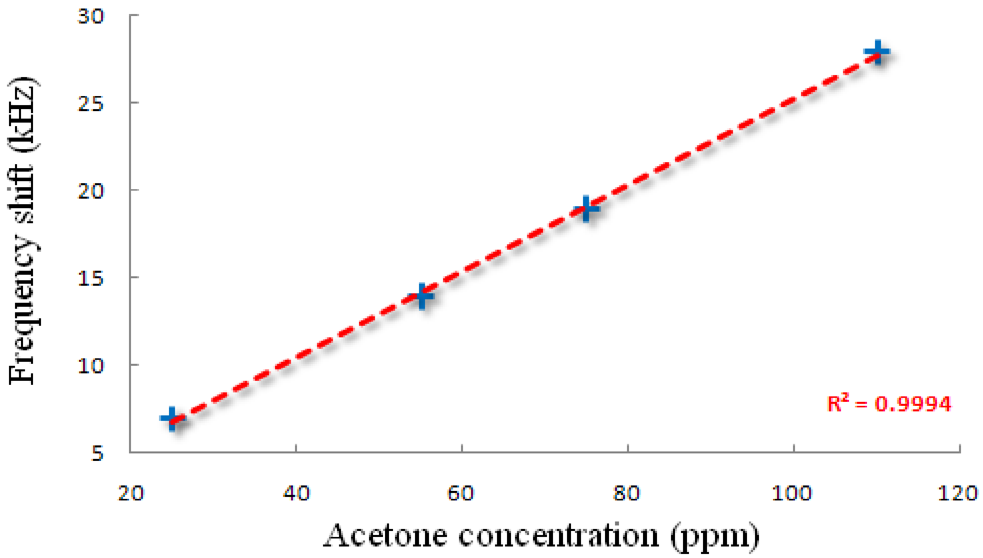

Figure 4.3 The linear region of the acetone response for FBAR. The experiment results were in agreement with the analysis model developed from the semiconductor gas sensor power law theory.

Ethanol and acetone can be distinguished using electrochemical or infrared instruments in commercial breath alcohol analyzers. However, they are complex and expensive. At the same time, specific training is required in order to become a fluent user. On the other hand, metal oxide sensors have simple structures. They are cost effective and easy to use. The main drawback is that they cannot effectively distinguish ethanol and acetone. Because they adopt the change of resistivity as the gas detecting signal, both ethanol and acetone will share a similar response: the decrease of the resistivity. Taking ZnO for example, it is a promising material for ethanol sensing applications. Ethanol sensors based on ZnO thin films (Sahay et al. 2005) have been extensively investigated. Special attention is given to discriminating between ethanol and acetone due to their similar chemical nature.

4.2.1 Ethanol response of FBAR

A similar FBAR as the one used in acetone sensing was adopted as an ethanol sensor. The room temperature response of the FBAR sensor to different ethanol concentration is shown in Figure 4.4. The resonant frequency decreased as the concentration of ethanol increased. A linear region and a saturation region were identified in the response curve. With 60ppm ethanol, the frequency shift was -21kHz. As the concentration increased to 720ppm, the frequency response reached saturation, with a shift of -34kHz. It is clear from the experiment results that FBAR has the ability to selectively detect ethanol and acetone.

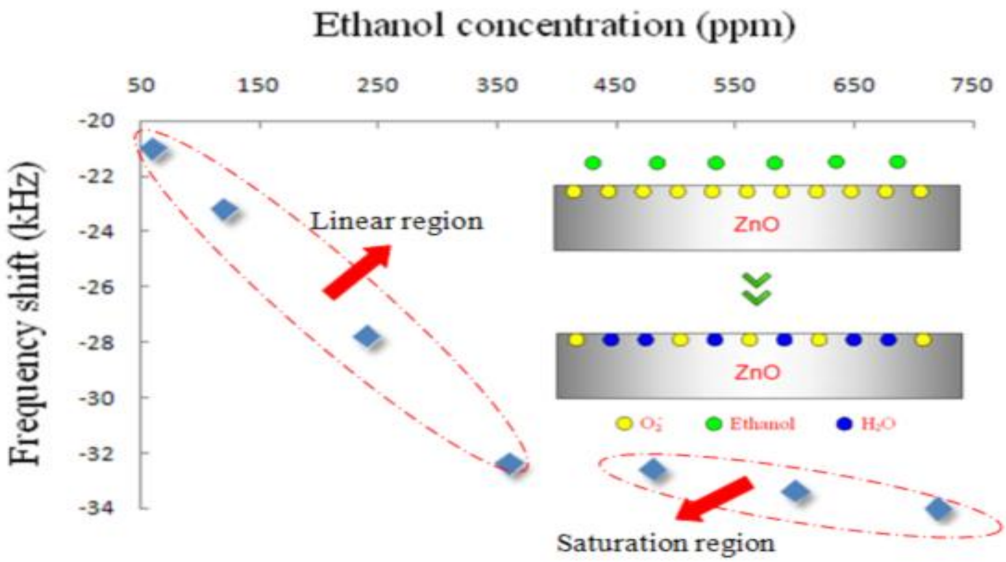

Figure 4.4 The ethanol response of the FBAR sensor: the resonant frequency of the FBAR decreased as the concentration of ethanol increased. A linear region and a saturation region can be identified. The inset illustrated the sensing mechanism: ethanol reacts with the adsorbed oxygen ions on the ZnO surface and generates water which is absorbed by the ZnO. Therefore, the density of the film increases, resulting in a frequency drop. It is clear from the experiment results that FBAR has the ability to selectively detect ethanol and acetone.

In most states in US, it is required by law that a driver is presumed to be under the influence of alcohol, if his breath alcohol content is found to be over 0.08 (grams of alcohol/210 liters breath), which corresponds to an ethanol concentration of 186ppm. This value is away from the saturation region of the FBAR sensor. Thus, FBAR has potential applications to be employed for breath alcohol analyzers.

Ethanol reacts with the adsorbed oxygen ions on the ZnO surface and generates water which is absorbed by the ZnO (Sahay et al. 2005). Therefore, the density of the film increases, resulting in a frequency decrease (Qiu et al. 2009). The reaction between ethanol and the adsorbed oxygen ions is as follow (Sahay et al. 2005).

$$C_2H_5OH + O_2^- \rightarrow CH_3COOH + H_2O + e^- \qquad \text{(Eq. 4.16)}$$

4.2.2 Analytical model for ethanol response

Similar as acetone, for ethanol, the frequency shift *Δf* can be formulated as:

$$\Delta f = \frac{1}{2d}\left(\sqrt{\frac{E}{\rho+\Delta\rho}} - \sqrt{\frac{E}{\rho}}\right) = \frac{\sqrt{E}}{2d}\frac{(1-\sqrt{1+\frac{\Delta\rho}{\rho}})}{\sqrt{\rho+\Delta\rho}} \qquad \text{(Eq. 4.17)}$$

In the equation above, ρ » $\Delta\rho$. In this way,

$$\Delta f \approx \frac{\sqrt{E}}{2d}\cdot\frac{\left(1-1-\frac{1}{2}\frac{\Delta\rho}{\rho}\right)}{\sqrt{\rho}} = -\frac{\sqrt{E}}{4d\rho\sqrt{\rho}}\Delta\rho \qquad \text{(Eq. 4.18)}$$

For the reaction between O^-_2 and ethanol, at equilibrium,

$$k_{o1}PO_2[e] = [O_2^-] + k_{e1}Pethanol[O_2^-] \qquad \text{(Eq. 4.19)}$$

$$k_{e1} = \frac{k_3}{k_{-1}} \qquad \text{(Eq. 4.20)}$$

where k_3 is the rate constant of the reaction between O^-_2 and ethanol and *Pethanol* is the partial pressure of ethanol.

Thus, the power law exponent *n*, defined as *d*(log*Δf*)/*d*(log*Pethanol*), is obtained,

$$\frac{d(\log \Delta f)}{d(\log Pethanol)} = 1 - \frac{1}{1+m^2} \qquad \text{(Eq. 4.21)}$$

where *m* is sufficiently large under usual conditions (Yamazoe and Shimanoe 2008). Thus *n* is around 1, which can be used to explain the linear region of the ethanol response (Fig. 4.5).

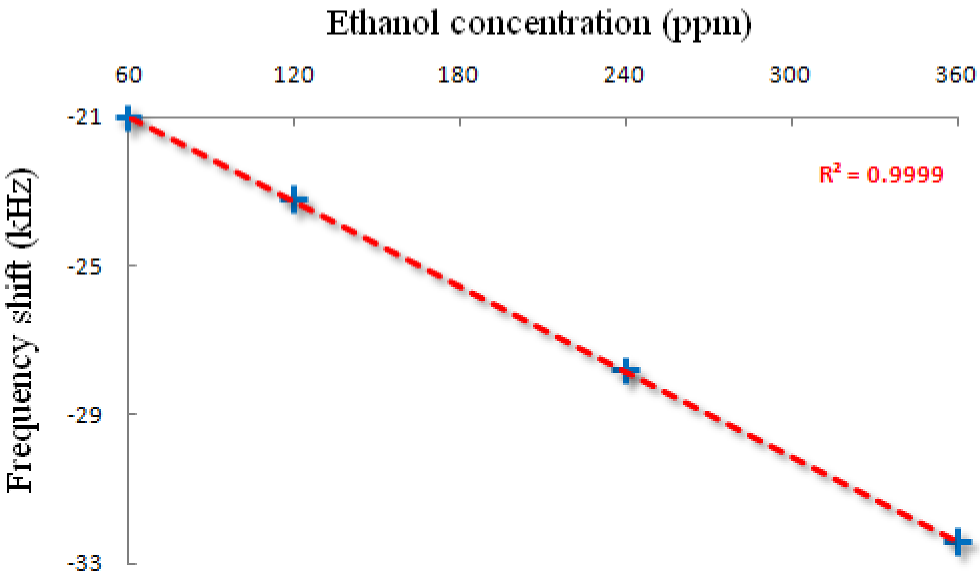

Figure 4.5 The linear region of the ethanol response for FBAR. The experiment results were in agreement with the analysis model developed from the semiconductor gas sensor power law theory.

4.3 Summary

This study investigated room temperature acetone and ethanol sensing using ZnO film based FBAR. The resonant frequency of the FBAR increased as the concentration of acetone increased, while the resonant frequency of the FBAR decreased as the ethanol concentration increased. The density decrease of the ZnO induced by releasing carbon dioxide generated from the reaction between acetone and the adsorbed oxygen ions on the ZnO surface was assumed to be responsible for the frequency upshift. On the other hand, the density of the ZnO increased by absorbing water generated from the reaction between ethanol and the adsorbed oxygen ions on the ZnO surface, resulting in a frequency drop. The results demonstrated that FBAR conquered the challenging issue of existing acetone/ethanol sensors. These two gases can be distinguished due to their opposite response on FBAR.

Chapter 5

REACTIVE MULTILAYER NANOFILMS FOR MICRO ELECTROMECHANICAL SYSTEMS PACKAGING

Micro-electromechanical Systems (MEMS) have been recognized as one of the next generation technologies that are of critical importance to the US economy. Applications for MEMS include pressure sensors, accelerometers, micromirrors, biosensors, microengines, and more. MEMS integrate individual functions (electrical, mechanical, optical, chemical, biological, and magnetic) into one complete structure, however, effective device packaging has been a significant bottleneck to making MEMS a commercial success. MEMS packaging has a number of critical functions: to protect the device in harsh environments, to prevent it from mechanical damage or chemical attack, to improve heat dissipation, and to enable device interaction with the environment. MEMS packaging has emerged from the integrated circuit (IC) packaging technologies, but the packaging issue is complicated by the unconventional nature of “micro mechanical structures”. Further complicating the process, MEMS packaging requirements are non-standard fully dependent on the functional performance and reliability requirements of the device. MEMS packaging costs can account for 50-80% of the manufacturing cost for initial commercialization, and the issue has become a major focus of both scientific research and industrial applications. Establishing an efficient packaging process would not only advance MEMS development but also speed up the product commercialization cycle.

Generally, there are two kinds of MEMS packaging processes: die level packaging and wafer level packaging. For die level packaging, multiple MEMS devices are fabricated on one wafer (usually silicon) and then diced and packaged individually. For wafer level packaging, all the MEMS devices on one wafer are packaged in parallel by bonding a cap wafer to the device wafer. Then dicing is performed on each packaged device.

5.1 MEMS wafer level packaging

In recent years, wafer level packaging has emerged as a popular route for MEMS packaging because it can reduce processing time and costs. Several bonding techniques have been reported in wafer level packaging applications, including anodic bonding, direct bonding, and intermediate layer bonding.

Anodic bonding (or electrostatic bonding) is commonly used in bonding silicon wafers. The technique was first introduced by Wallis and Pomerantz (1969), who sandwiched polished glass and metal parts together and heated them in air to a temperature well below the softening point of the glass. During heating, a power supply was connected to the glass-metal assembly. When a voltage in excess of several hundred volts was applied for several minutes, the glass and metal formed a strong bond. This anodic bonding technique has been further developed for Si to glass, Si to Si, and Si to thin film wafer bonding at moderate temperatures (573K – 723K) by applying a high DC voltage to the pair of materials (500V – 1000V). The advantage of anodic bonding is that two dissimilar materials can be bonded together to form a strong and hermetic seal. However, one disadvantage is that the bonding surfaces must be smoothed and thoroughly cleaned to achieve the strong bond. Another disadvantage is that the electrical field from the applied voltage and high temperature can affect the electrical properties and performance of the bonded structures.

Direct bonding (or fusion bonding) is an alternative joining process: two components with polished and pre-cleaned surfaces are stacked together and annealed at elevated temperatures to form a bond (Barth 1990). Direct bonding causes micro-deformations of surface features, leading to sufficient contact on an atomic scale to bond different materials. The temperature at which direct bonding will take place, is generally above one half the melting temperature of the bonding components. Direct bonding of Si wafers is commonly used in mass production, where initial bonding temperatures are between 573K and 1073K. The bonded pairs are annealed at 1073K -1373K to further strengthen the bonds. The high temperature required to achieve acceptable bond strength, however, has been a limitation for direct bonding. Another disadvantage is that to obtain a uniform bond, extremely smooth bonding surfaces are required. Surfaces can only have roughness of a few Angstroms, as compared to those undergoing anodic bonding, whose surface roughness can be within a few tens of nanometers (Harendt et al. 1991; Maszara et al. 1988).

There are alternatives to bonding silicon wafers, which include intermediate layer bonding methods, such as glass-frit bonding, thermocompression bonding, eutectic bonding, solder bonding, and adhesive bonding. All of them employ thin films on one or both component surfaces as the bonding media, and this helps lower the bonding temperature.

Glass-frit bonding involves glass as a bonding intermediary between surfaces: screen-printed or spun glass film (one with a low melting point) is melted on one or both of the surfaces to be bonded (Knechtel et al. 2006). The bonding temperature depends upon the type of glass film used, but generally ranges from 673K to 773K. It has been reported that Si anodic bonding can be refined using this method to achieve bonding at lower temperatures if sputtered borosilicate glass with a low melting temperature is used as a thin film layer on one of the Si surfaces (Choi et al. 1997; Weichel et al. 1998; Hanneborg et al. 1991). Thermocompression bonding uses a layer of soft metals on each surface: these surfaces are joined via solid state welding (Taklo et al. 2004). Gold is the most commonly used metal for silicon wafer bonding. Bonding is formed between two surfaces with thin gold pads by applying pressure at elevated temperature. The one drawback of this bonding method is the high pressure applied during the bonding process. Solder bonding works by reflowing low melting point metals to form a bond. Typical solders used in silicon wafer bonding are PbSn, AgSn, and AuSn (Goyal et al. 2004). The solder layer can be applied to wafers by screen-printing solder pastes. Processing temperatures for reflow soldering are normally lower than 823K. The problem with solder bonding, however, is that during reflow, the out-gassing of the flux and solvent in the solder paste can cause voiding in the bonding area (Sparks et al. 2001). Eutectic bonding uses Si-Ag, Si-Au, Si-Al, and Au-Sn alloys with eutectic composition as bonding media (Mei et al. 2002). Wafers targeted for bonding are first coated with two elements of the alloy, such as Si and Au, and then brought into contact. By heating the wafer pair, diffusion occurs at the interface and alloys are formed. The eutectic alloy at the interface has a lower melting point than the materials at both sides and therefore melting is restricted to a thin layer that forms a bond. The temperature used in the eutectic bonding, however, is still considered harmful for many heat sensitive MEMS devices. Adhesive bonding, by contrast, uses an intermediate adhesive layer such as epoxy to form bonds between different materials (Sarvar et al. 2002). This bonding process is a simple and inexpensive one with low requirements for surface smoothness. Bonding can be performed at room temperature or may require low temperature annealing, but disadvantages of this method include long-term instability, limited working temperature range, low bonding strength, and nonhermeticity of the package.

With the exception for the room temperature adhesive bonding, all the bonding methods described require elevated temperatures, and temperature sensitive components may be damaged or destroyed by global heating during the bonding processes. Dissimilar materials may also debond upon cooling due to mismatched coefficients of thermal expansion. New approaches with localized heating need to be developed to solve this bonding problem. In this way, high temperatures can be locally generated and hermetic and strong bonds can be achieved. At the same time, the temperature immediately away from the bonding area can be kept low.

There has been limited research on localized heating for wafer level packaging. Embedded microheaters can be used instead of global heating furnaces to prevent thermal problems during bonding (Cheng et al. 2002; Cheng et al.

2001; Cao et al. 2002; Cheng et al. 2000). These microheaters are constructed in a way that heating is restricted to a small region surrounded by thermal insulation materials, such as silicon dioxide. In this way, the bonding process can be conducted locally while the whole wafer is maintained at low temperature. The use of microheaters can, however, introduce complexity to the bonding design and in many cases, electrical wiring is not preferred. Another novel wafer level packaging method is localized induction heating solder bonding. According to literatures, electroplated magnetic Ni/Co film was heated using induction heating to cause the PbSn solder to flow and form a bond (Yang et al. 2005). Magnetic induction heated only the magnetic film during bonding, raising the film surface to high temperature within several seconds. Meanwhile, the rest of the wafer experienced an average temperature of only 383K. This localized heating method thus avoided thermal damage to the devices, but the method was not suitable to bond devices that were sensitive to magnetic fields. Localized heating can also be accomplished by laser (Luo and Lin 2002), microwave (Budraa et al. 1999) and ultrasound (Kim et al. 2009), however, these techniques require complicated equipment and bonding facility.

Bonding through localized heating is a promising method for wafer level packaging. It avoids thermal damage to the devices on the wafers caused by high temperature and/or extended heating and reduces the thermal stress on the package. Until recently, research in wafer level packaging with localized heating has been very limited, but reliable low temperature packaging strategies must be further researched to identify methods that are compatible with standard wafer processing techniques, and suitable for commercial use.

5.2 Reactive multilayer nanofilms

In this study, a novel room temperature packaging technique using reactive multilayer Ni/Al nanofilms as local heat sources to heat intermediate adhesive layers and thus bond two wafers together was proposed for wafer level packaging applications. No external heat sources such as furnace, microheater, or laser are required in this packaging approach. Reactive multilayer nanofilms contain thousands of nanoscale Al and Ni bilayers. With a small thermal pulse, these films can react exothermically and generate a self-propagating reaction. Self-propagating formation reactions in such films are driven by a reduction in chemical bond energy. This local reduction of chemical bond energy produces a large quantity of heat that is conducted down the foil and facilitates more atomic mixing and compound formation (Fig. 5.1). Such exothermic reactions in multilayer films can be used as local heat sources to melt solders or brazes and thus bond components in a variety of applications, such as bonding stainless steel, aluminum, titanium, metallic glass and silicon wafers (Wang et al. 2004; Wang et al. 2005; Duckham et al. 2004; Wang et al. 2003; Swisten et al. 2003; Wang et al. 2004; Qiu and Wang 2008). With localized heating, temperature sensitive components such as microelectronic devices can be joined without thermal damage. This bonding process can be performed in many environments, such as in vacuum, and can be completed in a second or less.

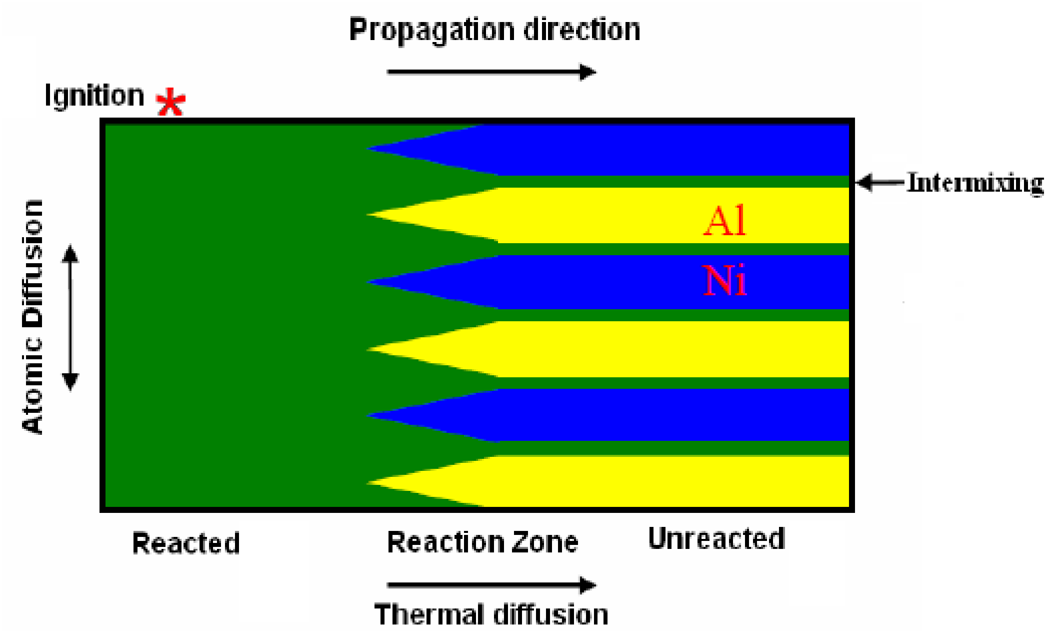

Figure 5.1 Schematic cross-sectional view of a self-propagating reaction in Ni/Al reactive multilayer nanofilms, showing both thermal and atomic diffusion that enable the propagation of the reaction.

5.3 Bonding Parylene C with Parylene C coated silicon wafers

Primary experiment for the reactive multilayer nanofilm packaging approach was conducted on bonding Parylene C with silicon wafers with a thin Parylene C coating. Parylene is the generic name for members of a unique polymer series. The most popular one is Parylene C (glass transition temperature: 382K), which can be used as a good alternative to the conventional adhesive materials. It can be directly vapor-deposited from a solid powder to a solid film at room temperature providing conformal coating regardless of surface morphology. Parylene C is also chemically inert and biocompatible. It has been extensively employed in MEMS (Suzuki and Tai 2006; Yu et al. 2008) and, recently, began to draw attention as a bonding agent. Kim and Najifi (2005) used parylene as an intermediate layer to bond silicon wafers at 503K for 30 minutes and achieved a bonding strength of 3.6MPa.

5.3.1 Experimental procedure

Ni/Al reactive multilayer films (Ni/Al atom ratio is 1:1) (Indium Corporation, Utica, NY) were fabricated by magnetron sputtering. The total thickness of the Ni/Al films used here was 40µm and 80µm respectively, with a bilayer thickness of 40nm (Ni: 16nm; Al: 24nm). These films were used as local heat sources to bond Parylene C layers to another Parylene C coating on silicon wafer. Two different thicknesses of films were used to bond Parylene C to investigate the impact of difference in heat generation on the bond quality. The crystallographic phases of the as-deposited Ni/Al multilayer films and the reaction products were investigated by X-ray diffractometer (XRD) using Cu Kα radiation. The heat of reaction was measured by a differential scanning calorimeter (DSC7). In each DSC run, about 10mg freestanding foils were heated from 323K to 998K at a rate of 40K/min in flowing N_2. A base line was obtained by repeating the heating cycle, which was then subtracted from the heat flow in the first run. By integrating the net heat flow with respect to time, the heat of reaction was obtained.

For Ni/Al films, the self-propagating reaction velocity decreased with increasing bilayer thickness. The heat of reaction increased as bilayer thickness increased, due to intermixing occurred during deposition (Wang et al. 2004). Therefore, Ni/Al films with bilayer thickness of 40nm were used to achieve a balance between high reaction velocity and high reaction heat.

The geometry for Parylene C bonding is shown schematically in Figure 5.2. A Parylene C layer (20 µm thick) was bonded to a silicon wafer (20mm by 20mm) with a thin Parylene C coating (20 µm). Ni/Al multilayer films were placed on top of the parylene layer as localized heaters. The width of the film was 2mm. An Al substrate (1cm thick) was used to apply pressure (about 1.1kPa) to the bonding assembly. The reactive film was ignited by a power supply with a voltage of 2V. After ignition, a self-propagating reaction occurred in the film and the heat released penetrated the top parylene layer and formed bond at the parylene/parylene interface. The bonding process was performed in atmosphere and it completed in less than one second.

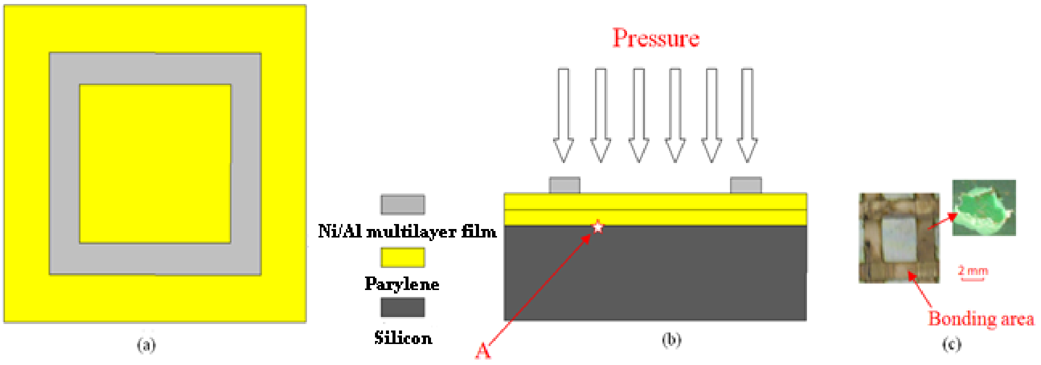

Figure 5.2 Schematic showing the reactive bonding geometry of Parylene C layers with silicon wafers with a thin Parylene C coating under an applied pressure: (a) top view, (b) cross-sectional view (not drawn to scale) and (c) a photograph of the bonding assembly. The inset shows the parylene layer was torn when the bond was forcefully broken, indicating a strong bond was achieved.

A numerical study was performed to predict the temperature evolution in the parylene layers and silicon wafers during the bonding process using commercial finite element analysis software, Fluent (Qiu 2009). The numerical model was based on a simplified description of the self-propagating reaction and the thermal transport occurring in the bonding assembly. The model assumed one-dimensional motion of the reaction front, which was described using experimentally determined heats of reaction and reaction velocities of the films (Wang et al. 2004). For the films with bilayer thickness of 40nm, the reaction velocity was 6m/s (Gavens et al. 2000). The simulation focused on heat flow into the parylene layers, and temperature evolution within the bonded components. The thermal resistance at the unbonded parylene/parylene interface was not considered. An ideal contact was assumed in the model. The simulation started when the reactive film was ignited. The physical properties of different materials used in the simulation are listed in Table 5.1.

Table 5.1 Thermophysical parameters for the reactive film, Parylene C, Al and silicon used in the simulation.

	Thermal conductivity (W/mK)	Heat capacity (J/kgK)	Density (kg/m^3)
Silicon	149	707	2330
Parylene-C	0.08	1000	1289
Al	202.4	871	2719
Film (as-deposited)	160	830	5500
Film (reacted)	25	610	5860

Leakage test was performed by immersing the bonded wafers in isopropanol alcohol (IPA). IPA has better wetability than water and it can more easily penetrate small openings, thus it is more suitable for leakage test. Red ink was pre-mixed in IPA as a marker for leakage. After testing, the bonded wafers were investigated under optical microscope to see whether red ink had penetrated into the enclosed area. The parylene/parylene bonding interface was examined by scanning electron microscopy (SEM).

5.3.2 Bonding results

XRD traces of the as-deposited Ni/Al multilayer films and the reaction products are shown in Figure 5.3(a). Before the reaction, all major peaks corresponded to Al and Ni. While after the reaction, all major peaks corresponded to the ordered B2 AlNi compound. Thus, the B2 AlNi compound was expected to be the dominant reaction product of the film during the bonding process.

In the DSC experiment of the Ni/Al reactive multilayer films, three exothermic peaks can be identified in the constant-heating-rate curve, as shown in Figure 5.3(b). By integrating the heat flow with respect to time, the heat of reaction was calculated to be -57.9kJ/mol. This result was used as input for the numerical study of the temperature distribution in the parylene layers and silicon wafers during the bonding process.

Figure 5.4 shows the numerical prediction of temperature evolution at the parylene/parylene bonding interface within 100ms after ignition for the 40 μm and 80 μm multilayer films. The highest temperature experienced at the bonding interface for these films were 419K and 545K, respectively. Both of them were below the melting temperature of Parylene C, which is around 563K. From previous research, in order to achieve a uniform bond between two parylene layers, a minimum temperature of 503K was applied (Kim and Najifi 2005), which indicated that in the current bonding approach, 80 μm multilayer films can be used to bond Parylene C.

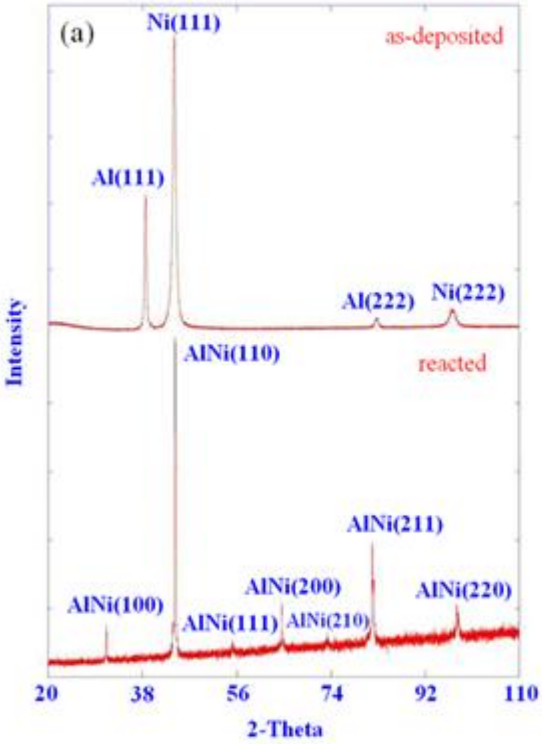

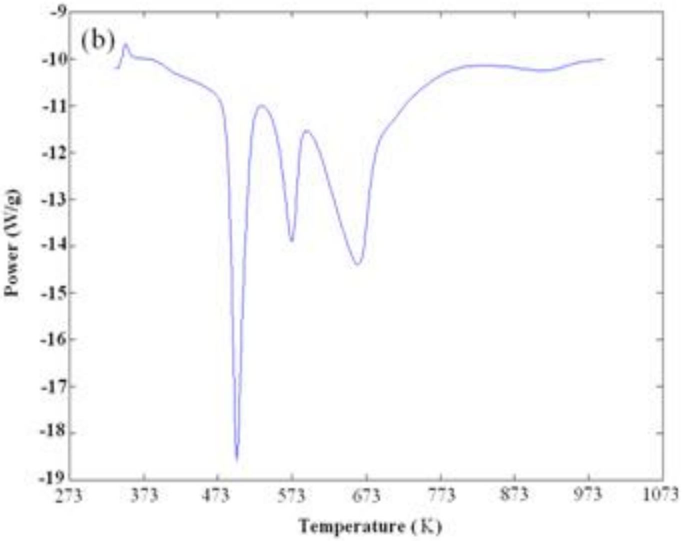

Figure 5.3 (a) XRD patterns for Ni/Al reactive multilayer films (both as-deposited and reacted). (b) DSC curve of Ni/Al reactive multilayer film. The heat of reaction was -57.9kJ/mol.

The temperature of the bonding interface returned to around room temperature in 100ms, demonstrating a high cooling rate can also be achieved in this bonding approach.

Leakage testing was performed by immersing the bonded package in IPA. For the packages formed by 40 µm film, they failed immediately after immersion, which showed that the 40 µm films cannot provide enough heat to form a hermetic bond between parylene layers. In contrast, a good resistance to liquid was shown for the package formed with 80 µm film by surviving IPA leakage test over one week. The quality of the parylene/parylene bonding interface was examined by SEM. Figure 5.5(a) shows the cross-sectional view of the bonding interface formed by 80 µm film. It was illustrated that the two parylene layers merged together as one layer without a distinguishable interface. The inset picture shows the bonding region with a higher magnification. Still, no interface in the parylene layer can be identified, indicating a good bond was achieved. The thickness of the new parylene layer was around 23 µm, which was much less than the total thickness of the two parylene layers before bonding (40 µm). This was due to the softening of parylene and the pressure applied during the bonding process. After reaction, the width of the bonded ring was larger than the width of the film used, indicating some parylene migrated out of the bonding area during the bonding process.

The cross section of the bonding interface formed by 40 µm film is shown in Figure 5.5(b). It was clear that there was an interface between the two parylene layers. At some locations, there were even cracks between these two layers (inset of Figure 5.5(b)), which indicated that 40 μm film cannot provide enough heat to soften the parylene layers and form a uniform bond between them. The SEM results were in agreement with the IPA leakage test. The thickness of the parylene layers in Figure 5.5(b) was around 34 μm, indicating only a small part of parylene was softened in the bonding process due to less heat generation of the 40 μm film compared to the 80 μm one. Therefore, the 80 μm film can be used in the present bonding application and the following experiments and simulations were only conducted for 80 μm films.

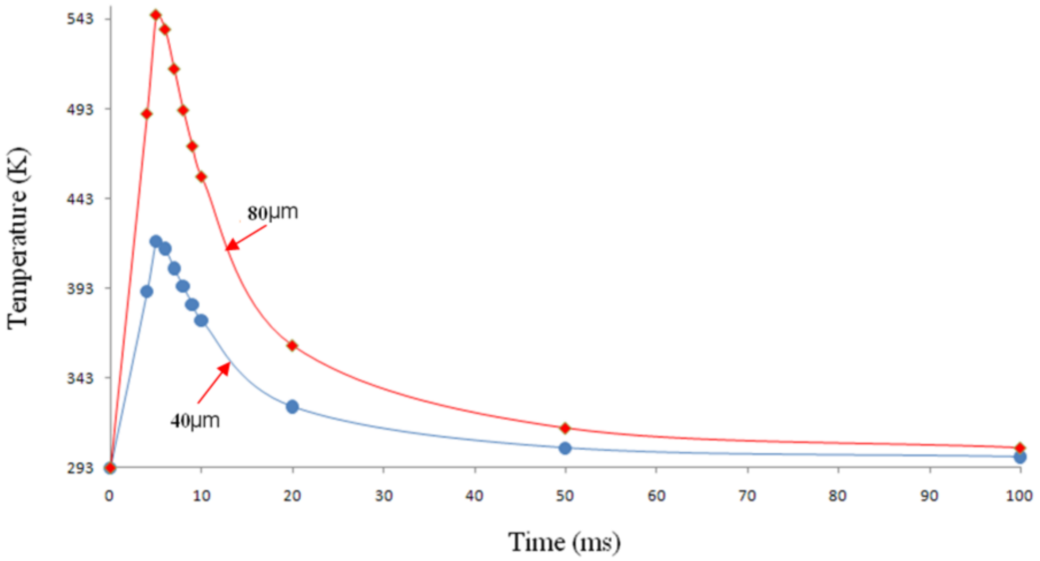

Figure 5.4 Temperature evolutions at the parylene/parylene bonding interface within 100ms after ignition for 40 μm and 80 μm multilayer films. The highest temperature experienced at the bonding interface for these films were 419K and 545K, respectively.

When the bond successfully formed by 80 μm film was forcefully broken, the Parylene C layer was torn, indicating a strong bond was achieved (inset in Figure 5.2(c)). Figure 5.6(a) shows the simulation results of temperature evolution at the silicon wafer surface within 100ms after ignition.

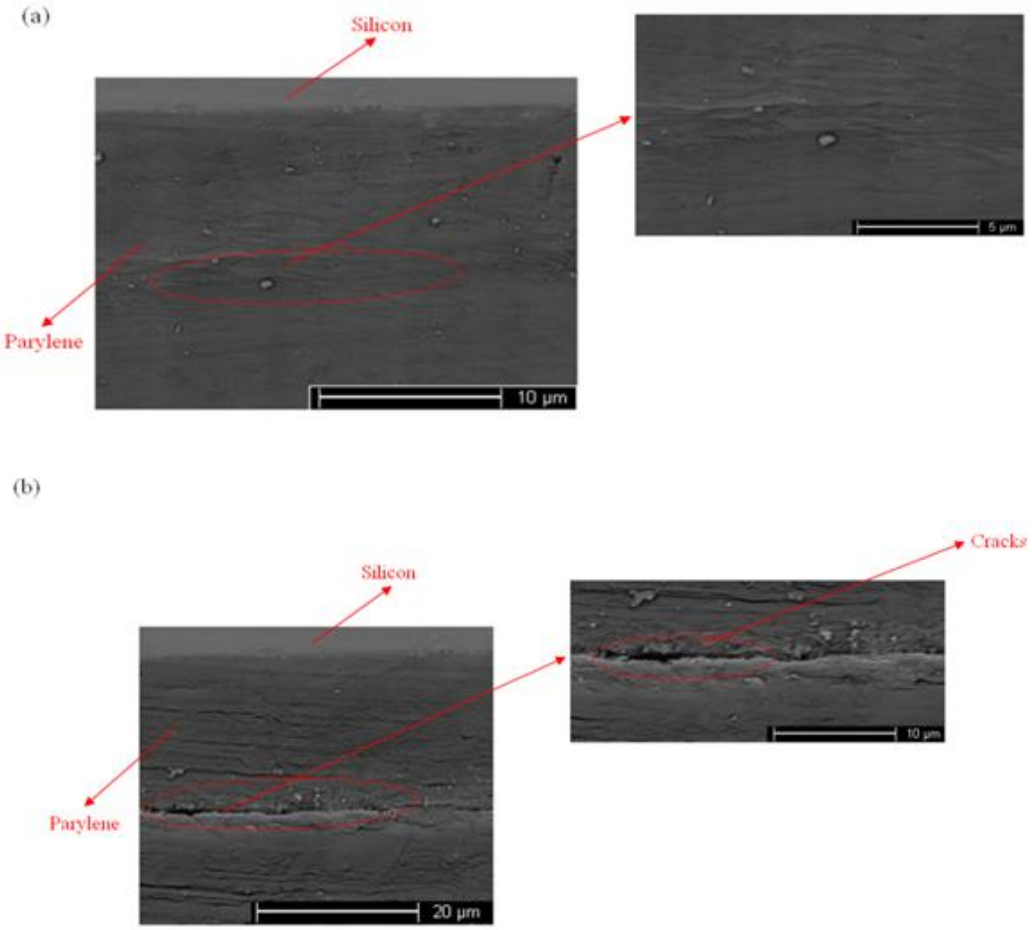

Figure 5.5 SEM pictures of the parylene/parylene bonding interface. (a) The cross-sectional view of the bonding interface formed by 80 µm films. It illustrates that the two parylene layers merged together as one layer without a distinguishable interface. The inset shows the bonding region with a higher magnification. Still, no interface in the parylene layer can be identified. (b) The cross section of the bonding interface formed by 40 µm films. It is clear that there was an interface between the two parylene layers. At some locations, there were even cracks between these two layers, indicating that 40 µm films cannot provide enough heat to soften the parylene layers and form a uniform bond between them. The particles in the pictures were due to the gold coating.

The highest temperature experienced at the silicon surface was 333K. Figure 5.6(b) and (c) show the contour graphs of the temperature distribution on the silicon surface at 9ms (when the silicon wafer experienced the highest temperature of 333K) and 100ms after ignition. The results illustrated that the high temperature region was well confined within the bonding area. Figure 5.6(d) shows the numerical prediction of temperature evolution within 100ms after ignition at a location 100 µm away from the bonding region on the silicon surface inside the package (point A in Figure 5.2(b)). The temperature profile demostrated that the highest temperature at location A was 301.2K and it decreased to 295.9K within 100ms. These results indicated that the heating area during the reactive bonding process was highly localized and the thermal exposure to the packaged components was very limited. This is a great advantage of the reactive film bonding process, especially for bonding structures with biological materials on them, since in general, such materials can only survive temperatures up to 318K for about two minutes (Craig 1993). These numerical results were in agreement with previous research on reactive bonding of stainless steel specimens showing that localized heating can be achieved by both numerical prediction and experimental observation (Wang et al. 2004; Wang et al. 2003).

5.4 Cell encapsulation

NIH 3T3 mouse fibroblast cells were encapsulated in the parylene formed package to verify the physiological compatibility of the reactive nanofilm bonding approach. The cells were cultured on the bottom surface of the cavity and left in an incubator to grow for twenty four hours before bonding was performed on the wafer. An optical microscope was used to inspect the cell adhesion and morphology inside the cavity. The geometry for Parylene C bonding with cell encapsulation is shown schematically in Figure 5.7.

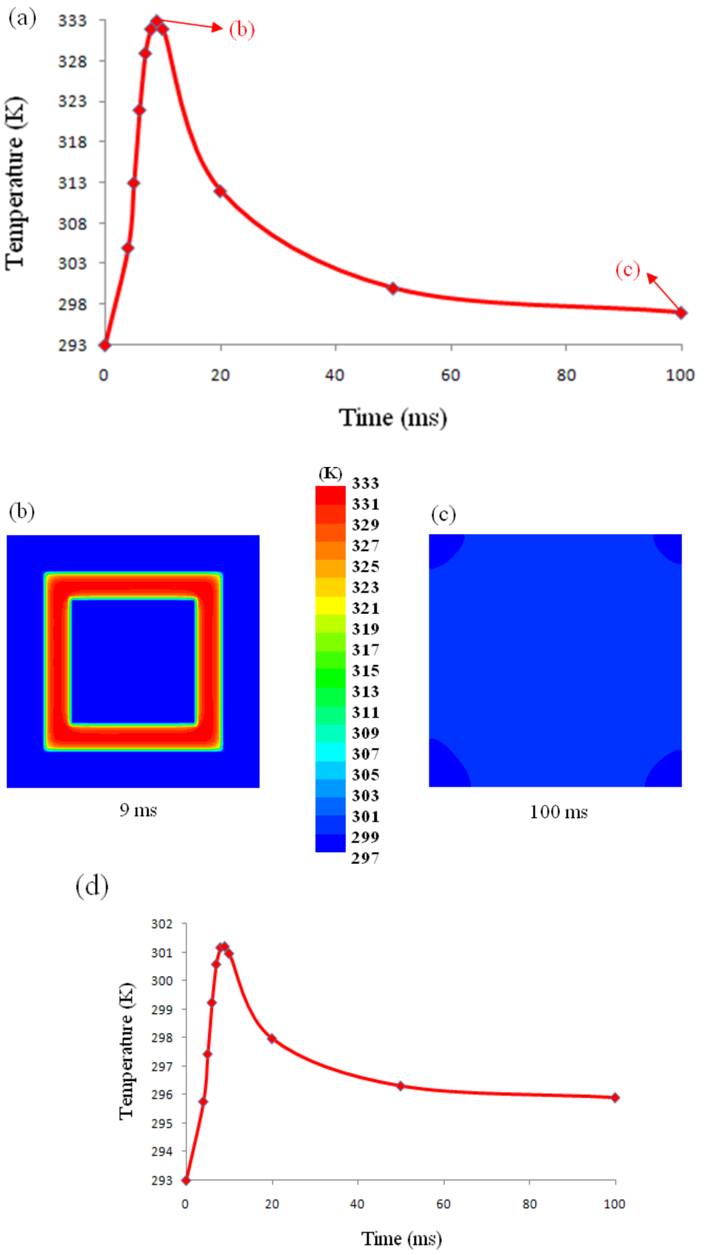

Figure 5.6 (a) The temperature evolution at the silicon wafer surface within 100ms after ignition. The highest temperature experienced was 333K. (b) and (c) The contour graphs of the temperature distribution on the silicon surface at 9ms and 100ms after ignition (the positions of (b) and (c) on curve (a) are pointed out by the arrows). The results illustrated that the high temperature region was well confined within the bonding area. (d) The numerical prediction of temperature evolution within 100ms after ignition at a location 100 µm away from the bonding region on the silicon surface inside the package. The temperature profile shows that the highest temperature at this location was 301.2K and it decreased to 295.9K within 100ms.

A similar numerical simulation was conducted to predict the temperature evolutions in the parylene layers, silicon wafer and the encapsulated liquid during the bonding process. Water was used in the simulation instead of culture media as the encapsulated liquid.

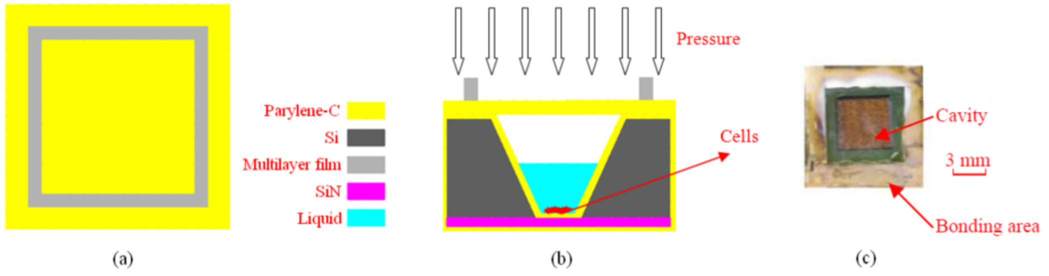

Figure 5.7 The schematic showing of the cell encapsulation package: (a) top view, (b) cross-sectional view (not drawn to scale) and (c) a photograph of the bonding assembly.

5.4.1 Experiment results

80 µm thick Ni/Al multilayer films with a bilayer thickness of 40nm were used here to bond the Parylene C layer to silicon wafers with a thin Parylene C coating and a cavity for cell encapsulation. As mentioned before, 80 µm thick films can generate enough heat to soften the parylene layers and form a uniform bond at the parylene/parylene interface (Qiu et al. 2009).

A successfully bonded cell encapsulation package is shown in Figure 5.7(c). In order to inspect the cell adhesion and morphology after bonding, the package was forcefully broken. Parylene C layer was torn in this process, while the bonding interface remained intact, indicating a strong bond was achieved. Figure 5.8 shows the microphotographs of NIH 3T3 cells before and after bonding. Visual inspection illustrated that there were no appreciable changes in the aspect of cell adhesion and morphology during the bonding process. The results demonstrated that the heat the cells exposed to in this bonding approach was negligible due to the localized heating nature of the reactive nanofilms. This was the first successful attempt to encapsulate live cells in microfabricated structures using wafer bonding techniques other than epoxy bonding.

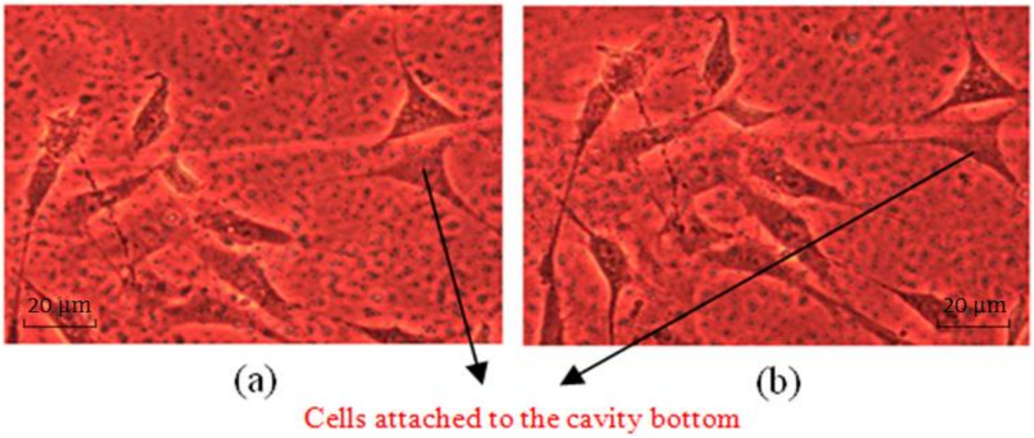

Figure 5.8 Microphotographs of NIH 3T3 cells: (a) cells encapsulated in the cavity before bonding and (b) cell adhesion and morphology showed no appreciable changes after packaging, indicating negligible heat exposure to the cells.

Figure 5.9 shows the numerical prediction of temperature evolution at the parylene/parylene bonding interface within 100ms after ignition. The highest temperature experienced at the bonding interface was 545K, which was below the melting temperature of Parylene C (563K). The temperature of the interface returned to around room temperature in 100ms, demonstrating a high cooling rate can also be achieved. Figure 5.10 shows the temperature distribution at the encapsulated liquid surface at the end of reaction (4ms after ignition) (a) and 100ms after ignition (b). The high temperature was well confined in the bonding region and the encapsulated liquid was almost undisturbed during the packaging process. Figure 5.10(d) shows the temperature evolution at a position 10 μm above the center of the cavity bottom inside the liquid (point A in Figure 5.10(c)). The highest temperature experienced was only 301.6K, which posed no harm to biological substances.

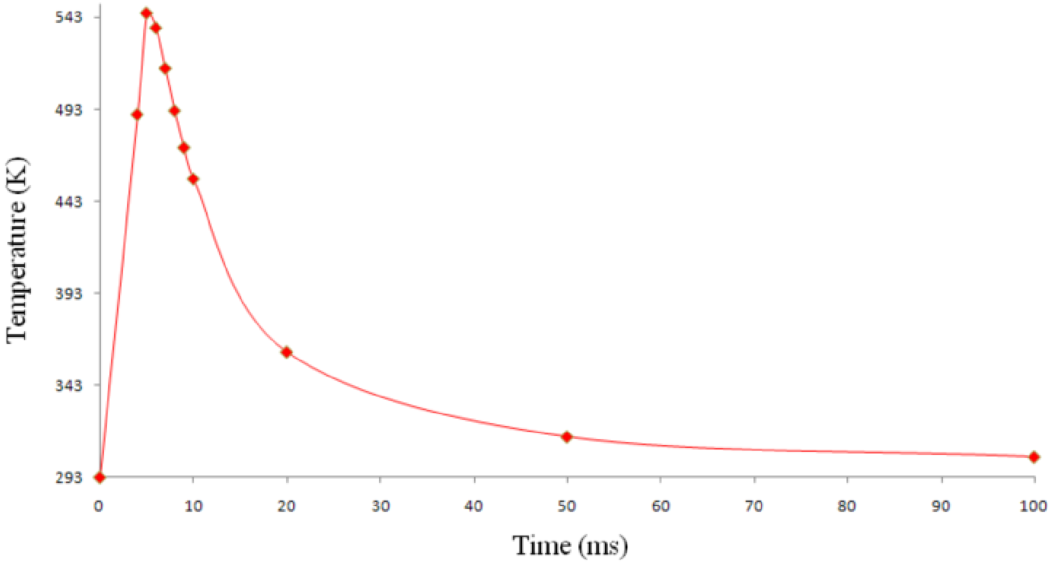

Figure 5.9 Temperature evolutions at the parylene/parylene bonding interface within 100ms after ignition. The highest temperature experienced at the bonding interface was 545K.

These results agreed with the cell encapsulation experiment, indicating that the heating during the reactive bonding process was highly localized and the thermal exposure to the packaging components was very limited. All the experiment mentioned above demonstrated the feasibility of reactive film joining for broad applications in bio-MEMS and microfluidic systems.

5.5 Micro initiator

Micro initiators can be found in numerous civilian and military applications such as triggering the inflation of airbags in automobiles (Baginski et al. 2001), micropropulsion systems for microsatellites (Zhang et al. 2005), and safe-and-arm devices used in missiles, rockets, and many other ordnance systems(Pezous et al. 2010).

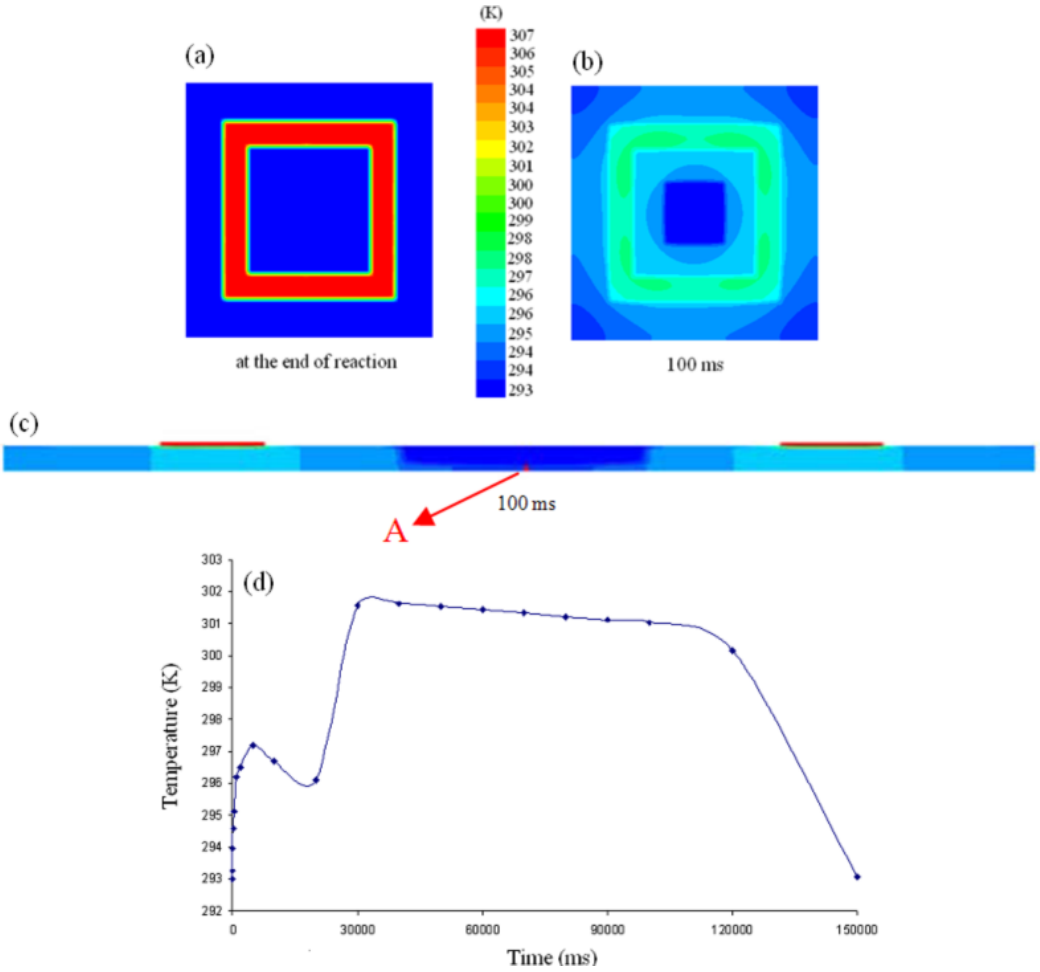

Figure 5.10 Simulation results: (a) temperature distribution at the encapsulated liquid surface at the end of reaction (4ms after ignition), (b) temperature distribution at the encapsulated liquid surface 100ms after ignition, (c) cross-sectional view of temperature distribution in the bonding assembly 100ms after ignition and (d) temperature evolution at point A (10μm above the center of the cavity bottom inside the liquid) within 150s after ignition. The highest temperature experienced was only 301.6K, which posed no harm to biological substances. The dip in the curve was due to the delay of the heat transferred to point A from the water above. Since A was close to the cavity bottom, it was heated up by the water beneath it first due to the much larger thermal conductivity of silicon compared to that of water.

Traditionally, a bridgewire was used to ignite the subsequent reactions. However, this kind of initiator suffers from weak contact between the wires and the reactive materials. Meanwhile, they are not suitable for batch fabrication and high level of integration due to the relatively large size. Nowadays, initiators usually employ micro resistive heaters, such as polysilicon heaters (Rossi et al. 2001) to initiate the explosives. However, an input voltage as high as 30 V is required. They also possess such disadvantages as low reliability and smaller output energy compared with input energy. Alternatively, a nano initiator has been developed by integrating Al/CuO based nanoenergetic materials with a thin film microheater (Zhang et al. 2008). However, the introduction of CuO nanowires complicates the fabrication process.

In this study, a micro initiator based on reactive Ni/Al films was investigated. The schematic structure of the micro initiator is shown in Figure 5.11. Ni/Al films (Ni/Al atom ratio is 1:1) were deposited layer by layer using magnetron sputtering and patterned by wet chemical etching (nitric acid and hydrochloric acid). The total thickness of the Ni/Al films used here was 10 μm with a bilayer thickness of 40nm. A SiO_2 layer was used under the Ni/Al film to provide thermal insulation from the silicon substrate. 1.5V DC voltage was applied to the film to initiate the self-propagating reaction. The voltage across the film was recorded by a NI USB-6289 Data Acquisition Card through a Labview program (National Instruments, Austin, TX). The data were used to calculate the ignition power and determine the ignition delay.

Numerical simulation was conducted to predict the temperature distribution on the initiator during ignition process. Thermal indicators (temperature indicating minilabel and temperature indicating liquid, OMEGA, Stamford, CT) were applied to the initiator to monitor the peak temperatures experienced at different locations on the device. The outcomes were compared with the simulation results.

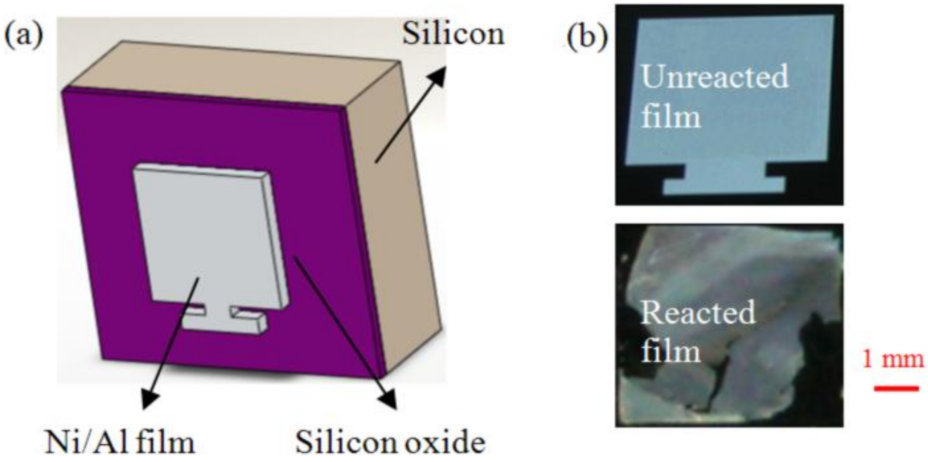

Figure 5.11 (a) The schematic structure of the micro initiator. (b) The photographs of the Ni/Al film before and after ignition. The film was bright and shiny before reaction. It turned out to be cracked after reaction due to the contraction from density change and cooling from high reaction temperatures.

5.5.1 Experiment results

Figure 5.12(a) shows the voltage variation with time during the initiation of the Ni/Al film. A 1.5V DC voltage was applied to the film (0.085s). The voltage drop across the film was 0.03V due to its small resistance (0.3Ω). At 0.715s, the voltage began to increase (Fig. 5.12(b)). Therefore, the ignition delay was around 0.63s and the ignition power was 3mW. In stage I (Fig. 5.12(b)), intermixing occurred between Al and Ni, which released heat and increased the film resistance gradually. As the heat accumulated, a self-propagating reaction was triggered, resulting in a sudden increase of the film resistance due to the generation of cracked AlNi (Fig. 5.11(b)). Thus, in stage II the voltage across the film reached the open circuit voltage of 1.5V in two milliseconds.

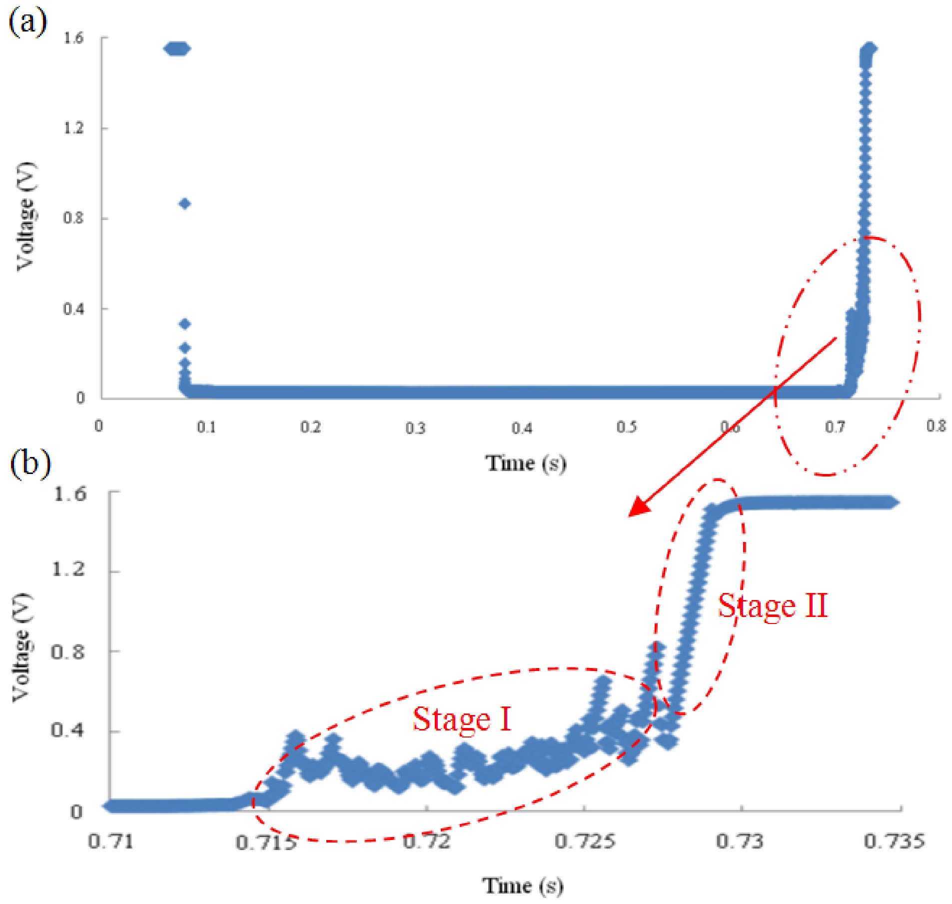

Figure 5.12 (a) The voltage variation with time during the ignition of the Ni/Al film. A 1.5V DC voltage was applied to the film (0.085s). The voltage drop across the film was 0.03V. (b) At 0.715s, the voltage began to increase. In stage I, intermixing occurred between Al and Ni, which released heat and increased the film resistance gradually. As the heat accumulated, a self-propagating reaction was triggered, resulting in a sudden increase of the film resistance due to the generation of cracked AlNi. Thus, in stage II the voltage across the film reached the open circuit voltage of 1.5V in two milliseconds.

Figure 5.13(a) and (b) illustrate the temperature distribution of the initiator 0.5ms after the ignition of the self-propagating reaction. High temperature (622K) can be achieved with 10μm thick film, while for 15μm thick one, it can reach

790K. Thus, the reactive film provided a simple way to control the working temperature of the initiator by alternating the film thickness.

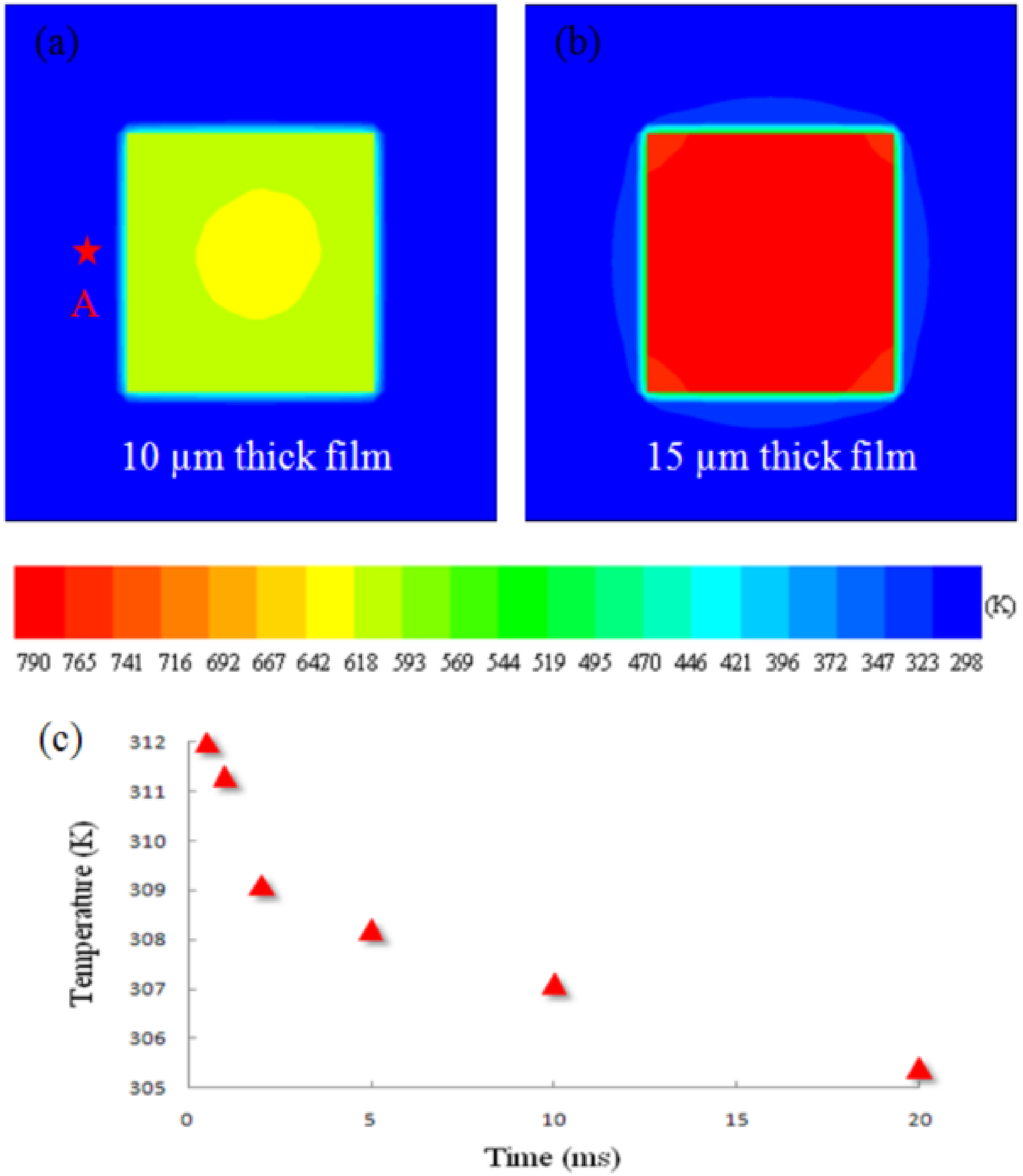

Figure 5.13 (a) and (b) show the temperature distribution of the initiator 0.5ms after the ignition of the self-propagating reaction. High temperature (622K) can be achieved with 10 μm thick film, while for 15 μm thick one, it can reach 790K. (c) shows the temperature evolution after the ignition of the self-propagating reaction at a position 100 μm away from the initiator (point A). The highest temperature was only 312K.

Another advantage was the localized heating nature of the Ni/Al film. Figure 5.13(c) shows the temperature evolution after the ignition of the self-propagating reaction at a position 100 µm away from the initiator (point A in Figure 5.13(a)). The highest temperature was only 312K. Thus, unintentional fire of adjacent initiators can be prevented and dense initiator array can be realized for such applications as in digital microthrusters.

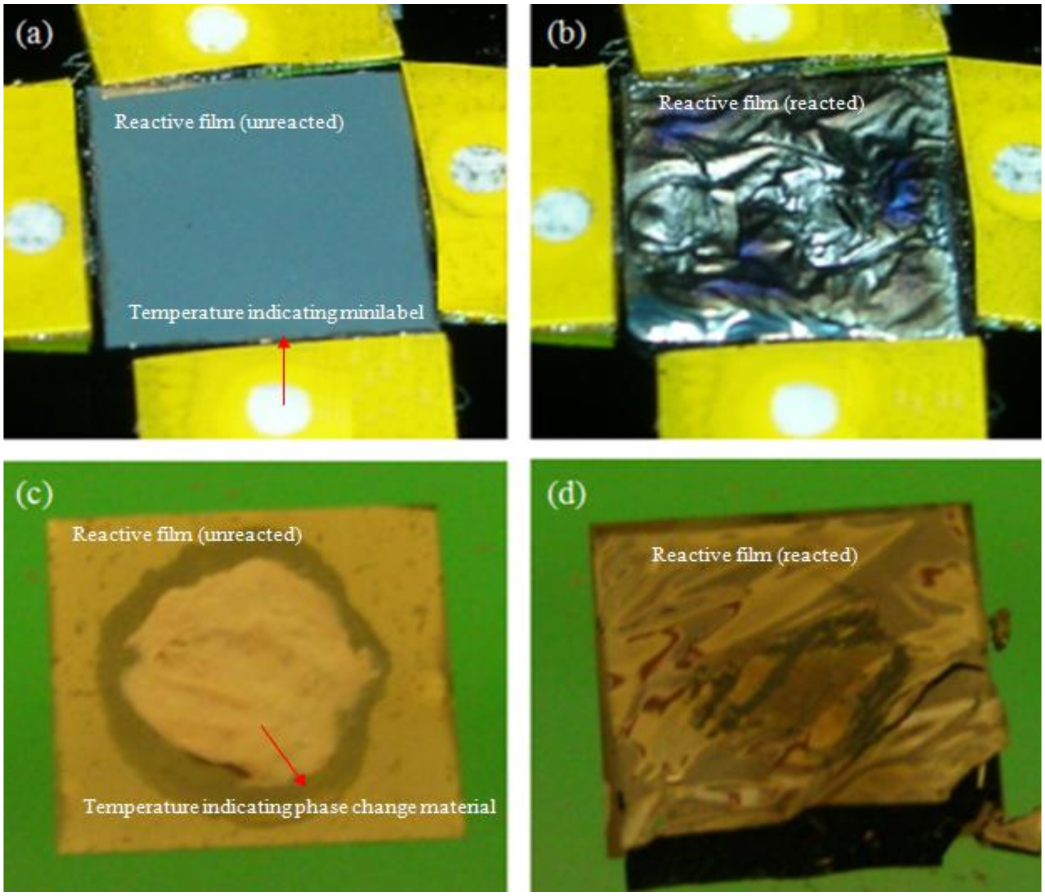

Figure 5.14 (a) and (b) illustrate that the color of the temperature indicating minilabels did not change during the ignition process of the initiator, which confirmed the localized heating nature of the Ni/Al film. (c) and (d) demonstrate that the surface temperature of the initiator exceeded 616K during the ignition process by using the temperature indicating liquid. The different appearance of the films was due to different background lighting conditions during the photo shoot.

Temperature indicating minilabels were placed next to the initiator before it was ignited (Fig. 5.14(a)). If the temperature exceeded 313K, the color of the label can change from white to black. Figure 5.14(b) illustrates the status of the labels after ignition. No appreciable changes were identified. Therefore, the localized heating nature of the Ni/Al film obtained from the simulation results was confirmed.

Temperature indicating liquid was used to evaluate the temperature of the initiator during the ignition process. When the initiator surface reached 616K, the indicator can transform from solid to liquid and evaporate. Figure 5.14(d) shows the experiment results. After ignition, there was no solid material left on the initiator surface, which demonstrated the surface temperature of the initiator exceeded 616K (a temperature high enough to ignite most common explosive materials). These results proved the feasibility of employing reactive Ni/Al films as potential micro initiators.

5.6 Summary

The Ni/Al reactive films were successfully used as local heat sources to bond Parylene C layers to a Parylene C coated silicon wafer. The parylene layer was torn when the bond was forcefully broken, indicating that a strong bond was achieved. Moreover, leakage testing in IPA showed that the bonds can withstand liquid exposure. Numerical simulation results demonstrated that localized heating occurred during the bonding process, which made reactive film joining an ideal method for parylene bonding applications.

Live NIH 3T3 cells were encapsulated in the reactive Ni/Al film formed package and they survived in the bonding process owing to the localization of heating. Numerical simulation results of the temperature evolutions in the bonding assembly were in agreement with the cell encapsulation experiment. They both revealed that localized heating occurred in this bonding approach. This study proved the feasibility of reactive nanofilm bonding technique for broad applications in packaging bio-MEMS and microfluidic systems.

A micro initiator was successfully realized by reactive Ni/Al nanofilms. With a DC voltage of 1.5V, a self-propagating reaction was triggered in the Ni/Al film. The ignition power of the film was 3mW with an ignition delay of around 0.63s. Simulation results showed that the initiator temperature can be altered easily by changing the Ni/Al film thickness. Localized high temperature can be generated on the initiator, which was confirmed by both the experiment and numerical modeling results. The micro initiator is supposed to have a variety of potential applications in both civilian and military areas.

Chapter 6

*P*H MEASUREMENTS WITH ZNO BASED SURFACE ACOUSTIC WAVE RESONATOR

The measurement of *p*H is very important in chemistry, biology, and environmental science. A number of different *p*H sensors are available nowadays. The classical method to determine *p*H values employed glass electrodes. They possessed good sensitivity, selectivity and long lifetime. However, the limitations, such as high impedance, high temperature instability and mechanical fragility restricted further applications in certain circumstances (Shuk and Ramanujachary 1996). As a result, non-glass *p*H electrodes, especially solid-state *p*H sensors using metal oxides, began to draw considerable attention, because they are mechanically robust, and less sensitive to cation interference (Fog and Buck 1984). Metal oxides, such as RuO_2 (Xu and Zhang 2010), TiO_2 (Zhao et al. 2010) and ZnO (Al-Hilli et al. 2007), have been used to fabricate *p*H value monitors. However, most of them require a reference electrode to operate, which leads to a bulky structure.

Surface acoustic wave travels along the surface of a material exhibiting elasticity, with amplitude that typically decays exponentially with depth into the substrate. Therefore in a surface acoustic wave resonator (SAW), the acoustic energy is confined in the near-surface region of a solid, resulting in high acoustic wave sensitivity to surface perturbations. Many sensing applications have been realized with SAW, such as UV (Sharma and Sreenivas 2003), gas (Wen et al. 2010) and bio-sensing (Sankaranarayanan et al. 2010). In this study, a novel *p*H sensor using ZnO based SAW was developed. No reference electrodes were employed. Meanwhile, the response signal of the sensor was in the frequency domain, which provided great potential for incorporating the sensor into a wireless sensing network (Huang et al. 2010).

6.1 SAW *p*H sensor design

The schematic structure of the SAW *p*H sensor is shown in Figure 6.1. The SAW was fabricated on top of a silicon substrate. A sputtered ZnO film (3.9 µm) was used both as the *p*H sensitive layer and the piezoelectric actuation layer for the SAW sensor. The top electrode was made of Cr/Au (0.02 µm/0.2 µm). The fabrication process of the SAW was as follows. First, ZnO was radio-frequency sputtered and etched (wet chemical etching) to form the desired pattern. Then the top Cr/Au electrode was deposited by electron-beam evaporation and patterned by lift-off. The electrodes consisted of 5 pairs of fingers, with an aperture of 480 µm and a spatial periodicity of 40 µm.

6.2 Experiment setup

The ZnO film was characterized by X-ray diffraction (XRD) using Cu K_α radiation. Solutions of various *p*H values were introduced to the active region of the SAW sensor using a mechanical pipette (Biohit, Helsinki, Finland). The *p*H values were calibrated by a commercial *p*H meter Exstik II (Extech Instruments, Waltham, MA). The SAW sensor was tested on a probe station with Ground-Signal-Ground 150 micron pitch probes from Cascade Microtech Inc. The calibration was carried out with an impedance standard substrate using a short-open-load (SOL) method. The resonant frequency of the SAW was monitored with an Agilent E5071C network analyzer and recorded by a LabVIEW program. Sodium chloride (NaCl) solutions with different concentrations were prepared as comparison samples. Their role was to demonstrate that the response of the SAW sensor was induced by the *p*H values not the conductivity of the solution.

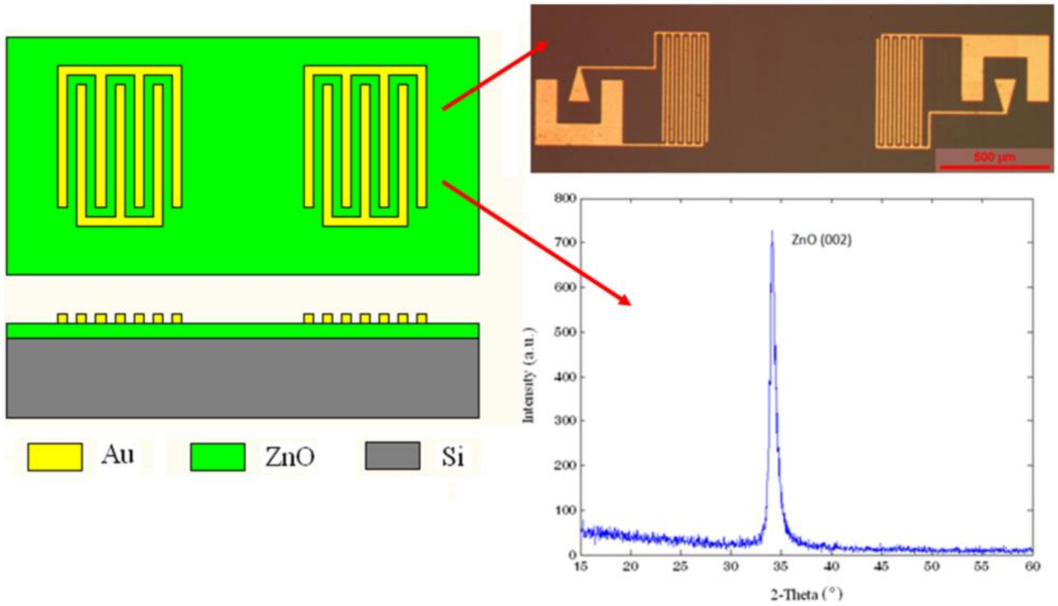

Figure 6.1 Schematic structure of the SAW *p*H sensor with a photograph of the top view of a fabricated device and an XRD trace of the ZnO film illustrating that it has (002) crystal orientation.

6.3 *p*H response of the SAW sensor

From the ZnO XRD trace, only the Bragg reflection corresponding to (002) planes was observed, indicating that the film had a preferred growth orientation along the wurtzite C axis, which was normal to the silicon substrate (Fig. 6.1).

The resonant frequency of the SAW sensor was 177MHz, which was suitable for integration with a wireless sensor network. The noise floor of the sensor was around 20kHz. Previous study showed that, for SAW with different thickness of ZnO films, the acoustic velocity was determined by the product of *hk* (*h*, ZnO thickness; $k=2\pi/\lambda$, wave factor; λ, acoustic wave length) (Du et al. 2008). At a certain wavelength, if *hk* is smaller than 0.3, no acoustic wave mode can be detected due to the low electromechanical coupling for a very thin ZnO film (Wu and Wang 2004). As the thickness increases, the Rayleigh (R) mode resonant peak starts to appear. Theoretical analysis shows that the acoustic velocity is close to that of the substrate at hk~0, and varies monotonically until it approaches the acoustic velocity of the surface material at $hk>>1$. The SAW *p*H sensor had an *hk* value of 0.61. Thus, the acoustic velocity of the sensor was between that of the ZnO film and the silicon substrate. The Rayleigh velocities of the SAW propagating in the ZnO and silicon are 2700m/s and 4680m/s, respectively (Du et al. 2008). Therefore, the resonant frequency of the R mode wave should be between 67.5MHz and 117MHz. In this case, the resonant peak observed in the *p*H sensor was not R mode. In layered structures, where the substrate has a higher acoustic velocity than the overlaying film, Sezawa (S) mode wave can be generated (Wu and Wang 2004). The S wave exhibits a higher phase velocity (higher resonant frequency) compared with the R wave for a certain thickness of ZnO film. Therefore, S wave was detected in the SAW sensor and used to monitor *p*H variations. The observation of S wave resonant frequency in the SAW *p*H sensor was in agreement with the results of previous study conducted by Du et al. (2008), which obtained S mode resonance in their ZnO based SAW with an *hk* value of 0.6. The appearance of S wave in a resonator with $hk<1$ implied good crystallinty of the ZnO, because only films with high crystal quality and large electromechanical coupling coefficient can generate S wave under such circumstances.

The response of the SAW sensor to different *p*H values is shown in Figure 6.2. In the acid region, the frequency decreased linearly as the *p*H value decreased with a detection limit of 0.03 *p*H change. In the atmosphere, oxygen is adsorbed on the surface of ZnO as negatively charged ions by capturing free electrons from the film, thereby creating a depletion layer with low conductivity near the surface. ZnO is an amphoteric oxide in which an electropositive metal atom gives the oxygen a sufficient negative charge to strip a proton from a neighboring hydronium (Al-Hilli et al. 2007). In this way, surface oxygen ions were neutralized and the conductivity of the ZnO film increased due to the shrinking of the surface depletion layer. In the alkaline region, a linear relationship between the resonant frequency and *p*H values can be identified with a detection limit of 0.02 *p*H change. The frequency, however, decreased as the *p*H value increased. The metal ions in the ZnO film are electropositive enough to serve as an electron acceptor from a neighboring hydroxide (Al-Hilli et al. 2007). Therefore, the conductivity of the ZnO film also increased in this case.

Surface acoustic waves in piezoelectric films are accompanied by a potential wave and electric fields originating from the polarization of the material under mechanical deformation. The electric fields interact with different carriers in a two-dimensional electron system (2DES) close to the surface. Consequently, the 2DES influences the propagation of the surface wave. It alters the wave velocity and produces an attenuation. The shift in SAW phase velocity v is given by

$$\frac{v-v_o}{v_o}=\frac{K^2}{2}\frac{1}{1+\left(\sigma/\sigma_m\right)^2} \qquad \text{(Eq. 6.1)}$$

where K^2 is the effective electromechanical coupling coefficient, σ is the sheet conductivity, and σ_m is a material constant. The velocity v_o is the phase velocity on a free surface (Wixforth et al. 1989). This velocity shift is accompanied by an attenuation of the wave intensity given by

$$\Gamma=\frac{\pi K^2}{\lambda}\frac{\sigma/\sigma_m}{1+\left(\sigma/\sigma_m\right)^2} \qquad \text{(Eq. 6.2)}$$

Since the SAW carries a flux of momentum equal to 1/v times the flux of energy, a loss of wave energy is accompanied by a loss of momentum. This loss of momentum appears as a force on the electron system. This phenomenon is generally known as the acoustoelectric effect (Wixforth et al. 1989). In the acid region, as *p*H value decreased, the interaction between hydronium and ZnO was enhanced, resulting in an increase of the film conductivity. From Eq. 6.1, a larger σ means a smaller v. Therefore, the phase velocity decreased as the conductivity of the film increased. The resonant frequency of the SAW is proportional to the phase velocity at certain wavelengths. Thus, a drop of resonant frequency can be expected. Similar analysis holds true in the alkaline region, as the interaction between hydroxide and ZnO also enhances the film conductivity. In Eq. 6.1, a higher K^2 is desirable in order to yield a higher sensitivity to *p*H changes. Sezawa mode usually possesses a higher K^2 (4%) compared with that (K^2~0.49%) of the Rayleigh mode (Du et al. 2008). Thus, as mentioned above, S wave was used in the *p*H sensing applications in this study.

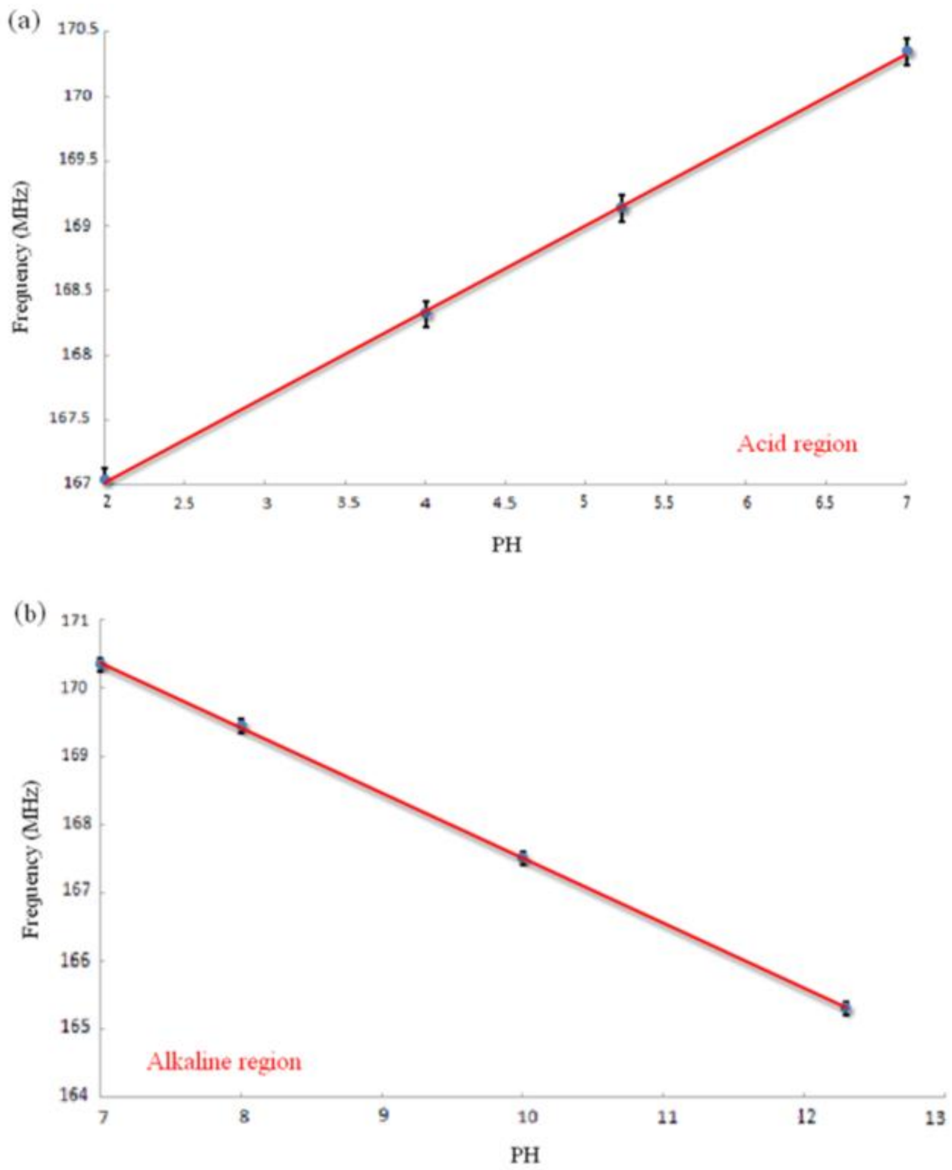

Figure 6.2 The response of the SAW sensor to different *p*H values: (a) In the acid region, the frequency decreased linearly as the *p*H value decreased with a detection limit of 0.03 *p*H change and (b) In the alkaline region, a linear relationship between the frequency and the *p*H values can be identified with a detection limit of 0.02 *p*H change. The frequency decreased as the *p*H value increased.

NaCl solutions with different concentrations were tested using the SAW sensor as comparison samples. No appreciable frequency changes were observed (Fig. 6.3), demonstrating that the response of the sensor was due to the interaction between hydronium or hydroxide and ZnO not the conductivity of the solution.

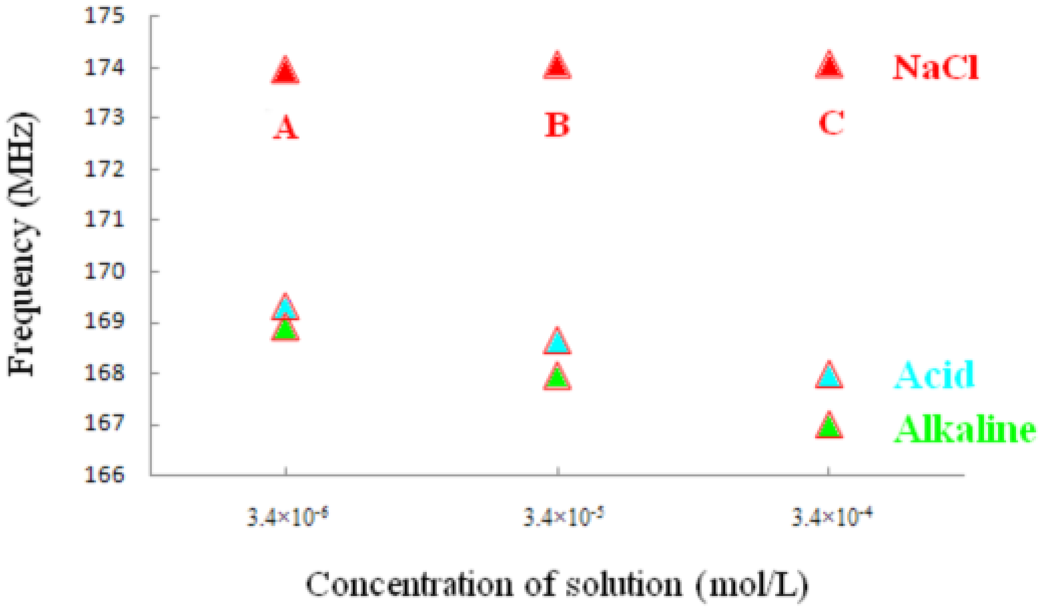

Figure 6.3 The response of the SAW sensor to NaCl solutions with different concentrations (sample A: 3.4×10^{-6}mol/L, sample B: 3.4×10^{-5}mol/L, sample C: 3.4×10^{-4}mol/L). The frequency shift between sample A and C was 0.11MHz. However, for the acid and alkaline solutions with same ion concentrations, the frequency shifts were 1.33MHz and 1.92MHz, respectively. The results demonstrated that the response of the sensor was due to the interaction between hydronium or hydroxide and ZnO not the conductivity of the solution.

6.4 The effect of ultraviolet radiation on the *p*H response of the SAW sensor

Previous studies demonstrated that ultraviolet (UV) can enhance the interaction of water with ZnO film (Sun et al. 2001). Therefore, UV was applied to monitor its effect on the *p*H response of the SAW sensor.

6.4.1 UV response of the SAW sensor

Figure 6.4 shows the frequency response of the SAW sensor under a UV (365nm) intensity of 7.5μW/cm^2. A frequency downshift of 89kHz was observed due to the acoustoelectric effect (Sharma and Sreenivas 2003). It is well established that when UV light is incident, electron-hole pairs are generated inside the ZnO film. The holes produced by light absorption migrate to the surface and discharge the negatively charged adsorbed oxygen ions. When an oxygen ion is discharged by the capture of a hole, it will be thermally desorbed (Melnick 1957; Collins and Thomas 1958; Takahashi et al. 1994). In this way, the conductivity of the ZnO film will increase (due to the increasing number of free electrons and the shrinking of the surface depletion layer), resulting in the decrease of acoustic velocity (Eq. 6.1). Therefore, the resonant frequency of the SAW sensor will decrease. When UV light is absent, oxygen readsorption will occur. Consequently, the conductivity of the ZnO film will decrease and the resonant frequency of SAW will increase.

Different intensities of UV light were applied to monitor the photoresponse of the SAW sensor. The results are shown in Figure 6.5. As the intensity increased, the frequency downshift also increased. At low intensity region (as shown in Figure 6.5), the relationship was almost linear, which made SAW sensor suitable to detect low intensity UV as a potential UV sensor. The lowest detectable intensity was around 2 μW/cm^2, which was comparable to commercial UV power meters available on the market.

6.4.2 *p*H response of the SAW under UV illumination

The *p*H response of the UV illuminated SAW sensor is shown in Figure 6.6 (acid region). UV enhanced the interaction of water with ZnO. Thus, the *p*H response was intensified under UV illumination, resulting in an improved detection limit of 0.02 *p*H change.

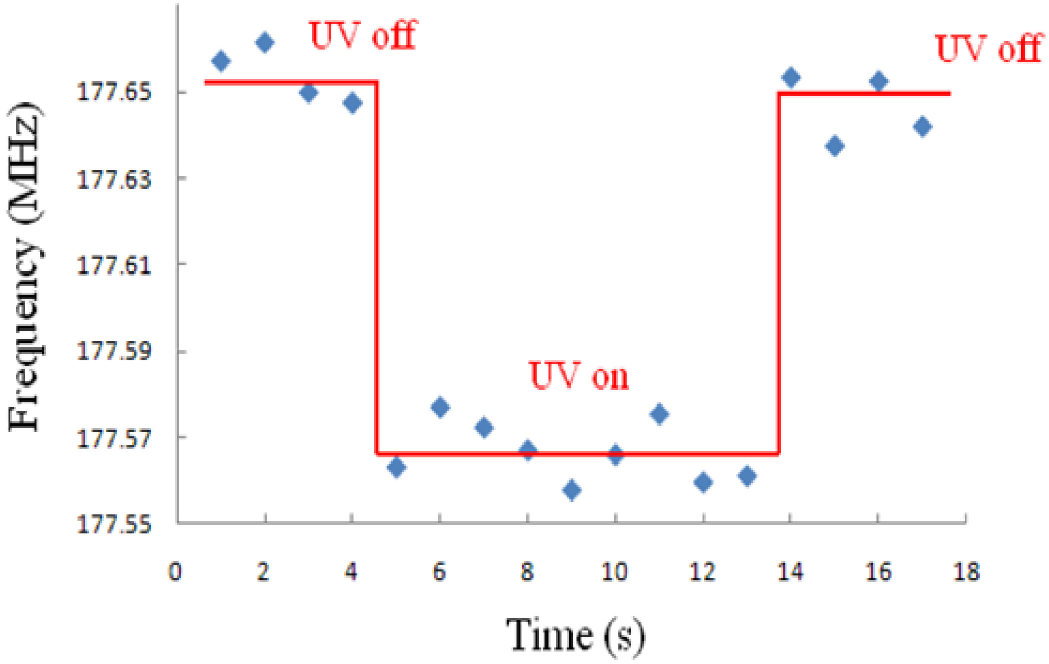

Figure 6.4 The UV (7.5 μW/cm^2) response of the SAW. A frequency downshift of 89kHz was observed due to the acoustoelectric effect. The noise floor was around 20kHz.

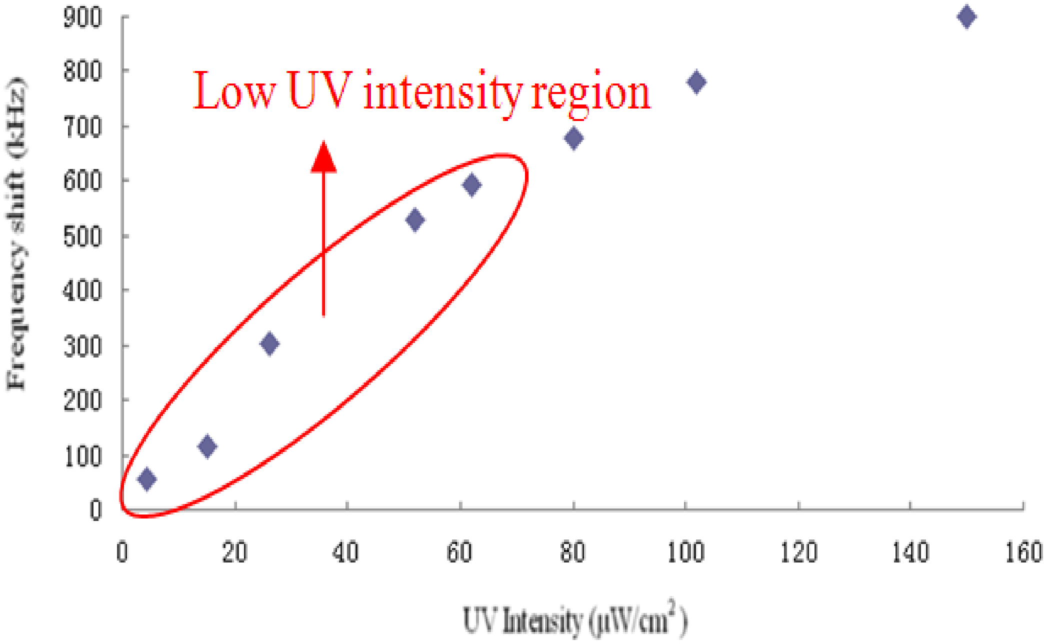

Figure 6.5 SAW's resonant frequency downshift vs. UV intensity, which showed that frequency downshift increased with increasing UV intensity. At low intensity region, the relationship was almost linear.

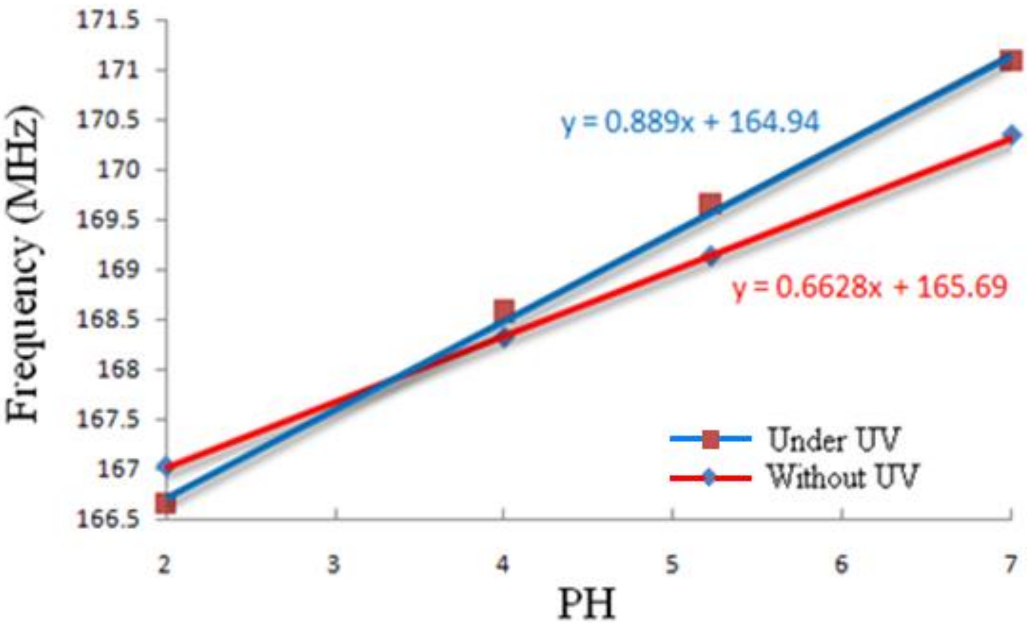

Figure 6.6 The *p*H response of the UV (7.5 μW/cm^2) illuminated SAW sensor (acid region). Under UV, a higher sensitivity was obtained. UV can enhance the interaction of water with ZnO film. Therefore, the *p*H response was intensified under UV illumination. Similar results can be expected in the alkaline region.

6.5 Summary

In this study, a ZnO based surface acoustic wave resonator was investigated as *p*H value monitors. The resonant frequency of the SAW decreased linearly as *p*H value decreased from 7 to 2 in the acid region. While in the alkaline region, the resonant frequency decreased linearly as *p*H value increased from 7 to 12. The detection limits were 0.03 and 0.02 *p*H change, respectively. The interaction between hydronium or hydroxide and ZnO was responsible for the frequency drop. Both of them can increase the conductivity of the ZnO film, resulting in the resonant frequency decrease due to the acoustoelectric effect. NaCl solutions were used as comparison samples in the testing. The results demonstrated that the response of the sensor was due to the interaction between hydronium or hydroxide and ZnO not the conductivity of the solution. UV light was used to illuminate the *p*H sensor. It can improve the sensitivity, resulting in a detection limit of 0.02 *p*H change in the acid region. Similar effects can be expected in the alkaline region.

Chapter 7

CONCLUSION

7.1 Conclusions

This dissertation explored various sensing applications for the ZnO based Film Bulk Acoustic Resonator (FBAR). In its simplest form, FBAR consists of a sputtered piezoelectric thin film (ZnO/AlN) sandwiched between top and bottom electrodes onto which an electric field is then applied. FBAR has been well developed both as filters and as high sensitivity mass sensors in recent years. In the current study, the sensing applications of FBAR were extended to monitor ultraviolet (UV), relative humidity (RH) and reducing gases, such as ethanol and acetone.

Under UV illumination, the resonant frequency of the FBAR upshifted. For 365nm UV light, the frequency upshift was 9.8kHz under an intensity of 600 $\mu W/cm^2$, and the detection limit of the sensor was 6.5nW. The frequency upshift of the FBAR UV sensor was proposed to be due to the density decrease of ZnO film upon UV illumination. When UV was incident on the ZnO film, it can cause oxygen desorption from the ZnO surface, resulting in density decrease of the film. The influence of temperature, relative humidity and reducing gases on the UV response of the FBAR was investigated. As temperature increased, the UV response of the FBAR degraded. Water molecules can replace adsorbed oxygen on the ZnO surface. As RH increased, more oxygen was replaced by water. In this way, the density of the ZnO film increased and less oxygen was left on the surface to be desorbed by UV, both of which contributed to a lower UV response with increasing humidity. Reducing gases, such as acetone, were exposed to FBAR. A smaller UV response was observed. In order to avoid the influence of these enviormental factors, a vacuum package may need to be pursued for the FBAR UV sensor.

Relative humidity was measured with ZnO based FBAR. The resonant frequency of the FBAR decreased linearly in a two-stage manner as the RH increased in the environment. For low RH (RH<50%), a frequency downshift of 2.2kHz per 1% RH change was observed. This effect was attributed to water molecules replacing the adsorbed oxygen on the ZnO surface, thus increasing the density of the film. While for high RH (RH>50%), a frequency downshift of 8.5kHz per 1% RH change was obtained, which was due to the mass loading effect of the water layers formed on the ZnO surface. Based on the theory of power law for semiconductor gas sensors and the mass loading effect of liquid on the FBAR, the mechanism behind this two-stage linear response was investigated. UV light was applied to monitor its effects on the humidity sensing performance of the FBAR. UV can enhance the sensitivity at low RH, while degrading the sensitivity at high RH.

For reducing gases sensing applications, the resonant frequency of the FBAR decreased as the concentration of ethanol increased. With 60ppm ethanol, the frequency shift was -21kHz. As the concentration increased to 720ppm, the frequency shift changed to -34kHz, reaching saturation. Ethanol reacts with the adsorbed oxygen ions on the ZnO surface and generates water which is absorbed by the ZnO consequently. Thus, the density of the film increases, resulting in a frequency decrease. On the other hand, acetone reacts with the surface adsorbed oxygen ions on the ZnO film and releases CO_2 as a reaction product. Thus, the density of the film decreases, resulting in a frequency increase. With 25ppm acetone, the frequency shift was 7 kHz. As the concentration increased to 220ppm, the frequency shift rose to 30kHz.

A potential wafer level packaging method based on localized heating approach using reactive Ni/Al nanofilms was investigated. The Ni/Al reactive films were successfully used as local heat sources to bond Parylene C layers to a Parylene C coated silicon wafer. The parylene layer was torn when the bond was forcefully broken, indicating that a strong bond was achieved. Moreover, leakage testing in IPA showed that the bonds can withstand liquid exposure. Live NIH 3T3 cells were encapsulated in the reactive Ni/Al film formed package and they survived in the bonding process owing to the localization of heating. Numerical simulation results of the temperature evolutions in the bonding assembly were in agreement with the cell encapsulation experiment. They both revealed that localized heating occurred in this bonding approach.

A micro initiator was successfully realized by reactive Ni/Al nanofilms. With a DC voltage of 1.5V, a self-propagating reaction was triggered in the Ni/Al film. The ignition power of the film was 3mW with an ignition delay of around 0.63s. Simulation results showed that the initiator temperature can be altered easily by changing the Ni/Al film thickness. Localized high temperature can be generated on the initiator, which was confirmed by both the experiment and numerical modeling results.

ZnO based surface acoustic wave resonator was investigated as a potential *p*H value monitor. The resonant frequency of the SAW decreased linearly as *p*H value decreased from 7 to 2 in the acid region. While in the alkaline region, the resonant frequency decreased linearly as *p*H value increased from 7 to 12. The detection limits were 0.03 and 0.02 *p*H change, respectively. The interaction between hydronium or hydroxide and ZnO was responsible for the frequency drop. Both of them can increase the conductivity of the ZnO film, resulting in the resonant frequency decrease due to the acoustoelectric effect. NaCl solutions were used as comparison samples in the testing. The results demonstrated that the response of the sensor was due to the interaction between hydronium or hydroxide and ZnO not the conductivity of the solution. UV light was used to illuminate the *p*H sensor. It can improve the sensitivity, resulting in a detection limit of 0.02 *p*H change in the acid region. Similar effects can be expected in the alkaline region.

7.2 Suggestions for future work

7.2.1 SAW UV sensor

As discussed in previous chapters, the stress-free boundary imposed by the surface of a crystal can give rise to a unique acoustic mode whose propagation is confined to the surface and is therefore known as surface acoustic wave. In 1887 Lord Rayleigh discovered this mode of propagation in which acoustic energy is confined very near the surface of an isotropic solid (Rayleigh 1885). Due to its high sensitivity to surface perturbations, SAW has been employed in a variety of sensing applications, such as UV (Sharma and Sreenivas 2003), gas (Wen et al. 2010) and bio-sensing (Sankaranarayanan et al. 2010).

Our preliminary results demonstrated that the SAW UV sensor possessed an improved detection limit (2 μW/cm^2) compared with the FBAR counterpart (25 μW/cm^2), even though the noise floor in the SAW sensor was much higher (20kHz compared to 1kHz). By optimizing the resonator design, we can achieve lower noise level in the SAW sensor. Therefore, an ultra low intensity UV detector can be realized using surface acoustic wave resonators.

Previous studies showed that by changing the thickness of the ZnO film in the SAW sensor, opposite response to UV illumination can be obtained (Sharma et al. 2003). With thin film, the acoustoelectric effect played a dominant role, resulting in decrease of resonant frequency under UV illumination. While with thick film, in which the surface wave was fully confined in the piezoelectric material, the oxygen desorption from the ZnO induced by UV illumination can result in density decrease of the film leading to an increase in resonant frequency. UV sensors can be realized by both of these two sensing mechanisms. And comparison can be performed to determine which mechanism can achieve a higher sensitivity. Based on these results, we can decide which way to go to further our research on low intensity UV monitors.

7.2.2 Lateral field excitation FBAR sensor

Conventional FBAR has been using thickness field excitation (TFE) to excite an acoustic wave in the resonator, and called TFE FBAR (Fig. 7.1). As the thickness of the piezoelectric film is reduced in order to achieve a higher resonant frequency, the electrode layers constitute a greater portion of the resonator. The TFE FBAR suffers reduced Q factors due to the presence of two metal layers in the acoustic path. Lateral field excitation (LFE) FBAR, on the other hand, does not have an electrode in the major acoustic path (Fig. 7.1). Moreover, the shear acoustic wave used in LFE FBAR generally has less acoustic attenuation than the longitudinal acoustic wave used in TFE FBAR.

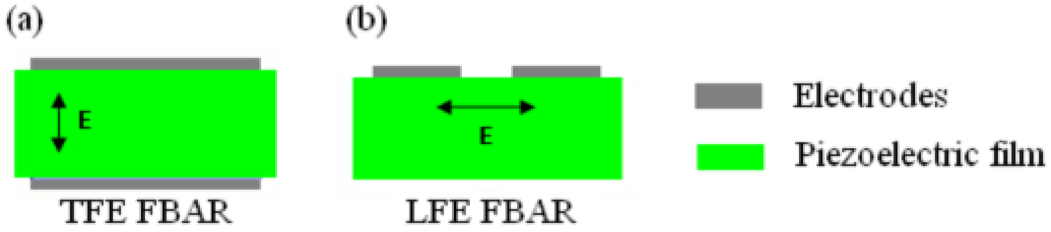

Figure 7.1 The Schematic structure of the film bulk acoustic resonator (FBAR): (a) thickness field excitation (TFE) FBAR and (b) lateral field excitation (LFE) FBAR (the arrows in the drawing indicate the direction of the electrical filed inside the piezoelectric thin film).

The advantages of LFE over TFE are mainly attributed to the fact that in LFE, the electrodes that generate the electric field are not directly in the path of the acoustic wave, as in TFE. Since the metal material that forms the electrode is a source of acoustic wave scattering and damping, its removal from the acoustic path results in higher *Q* values. Other advantages include increased stability at a given harmonic and reduced aging of the crystal since the electrode is absent from the area of largest vibrational motion (Corso et al. 2007). For sensing applications, removing the electrodes from the acoustic path means that sensing target can be in touch with the active region directly, which should result in higher sensitivity of the sensor (Wang et al. in press). Meanwhile, the temperature coefficient of resonant frequency (TCF) of the LFE FBAR is smaller compared with the TFE FBAR, resulting in improved temperature stability for sensing applications.

We designed a LFE FBAR, which is shown in Figure 7.2. It was fabricated on top of a SiN (0.6 µm) diaphragm with a sputtered ZnO film (1.2 µm) used as the piezoelectric actuation layer. The top electrode was made of Al (0.2 µm). The measured resonant frequency was around 860MHz, with a noise floor of 29ppm. The large noise floor was due to the small Q of the LFE FBAR (around 50). The poor quality factor may be a result of weak interaction between the electrical field and the piezoelectric material from the current electrode design (Wathen et al. 2009). Additional efforts to optimize the electrodes need to be pursued in the future. The TCF of the fabricated LFE FBAR was -37.4ppm/^{o}C (Fig. 7.3).

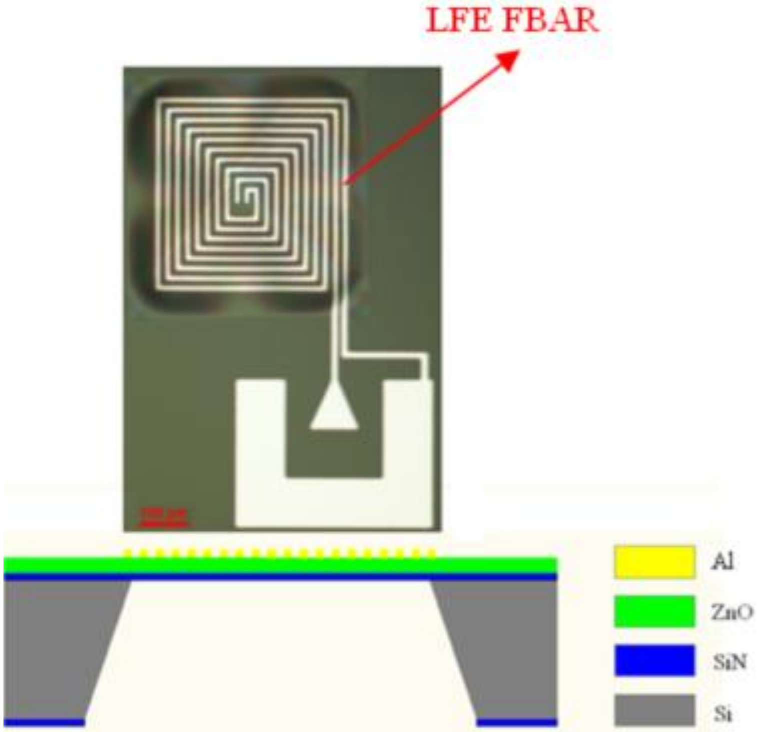

Figure7.2 Schematic cross-sectional view of the LFE FBAR with a photograph of the top view of a fabricated device.

Using carefully designed LFE FBAR, we can replicate the sensing applications accomplished by TFE FBAR, such as UV, RH, ethanol and acetone sensing with potentially higher sensitivity. Another research approach may involve using the LFE FBAR to prove our proposed sensing mechanism for UV response. Since LFE FBAR can be deployed in liquid without significant acoustic attenuation due to the use of shear wave, we can put a water droplet on top of the resonator. Under UV illumination, oxygen can be desorbed from the ZnO film, which increases the resonant frequency. When UV source is off, oxygen cannot be readsorbed to the surface of the resonator due to the water cover. Therefore, a delay in the frequency recovery can be identified and employed as an indirect evidence for our proposed UV sensing mechanism in FBAR sensors.

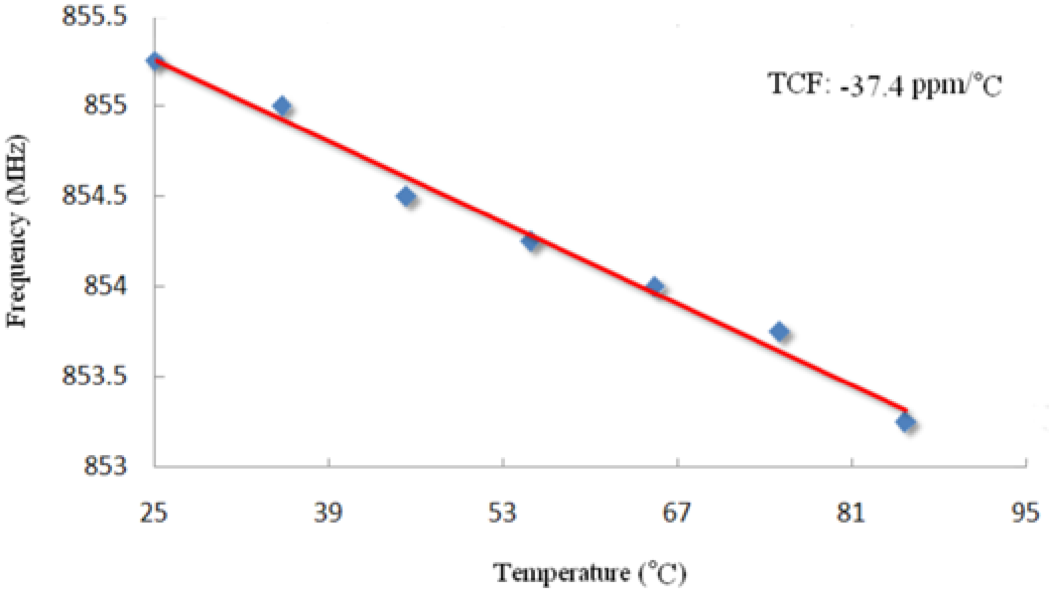

Figure 7.3 The frequency response of the LFE FBAR to temperature.

7.2.3 Patterning Ni/Al nanofilms for wafer level packaging applications

Ni/Al nanofilms were sputtered layer by layer and patterned on the silicon substrate using wet chemical etching (nitric acid and hydrochloric acid). A SiO_2 layer was used to provide thermal insulation between the film and the substrate.

Before sputtering the Ni/Al film, a thin metal layer (Cu/Cr) was deposited to enhance the adhesion of the film to Si. The deposition time for 15 μm thick film (bilayer thickness 40nm) was around 10 hours. The etching time was around 20 minutes.

Figure 7.4 shows the patterned Ni/Al film on the silicon substrate. It can be ignited by a DC voltage of 1.5V. After reaction the film peeled off from the substrate due to the mismatch of coefficient of thermal expansion. This is unacceptable for the bonding applications. In the future, we need to find a solution to prevent the detachment of the film during the exothermic reactions.

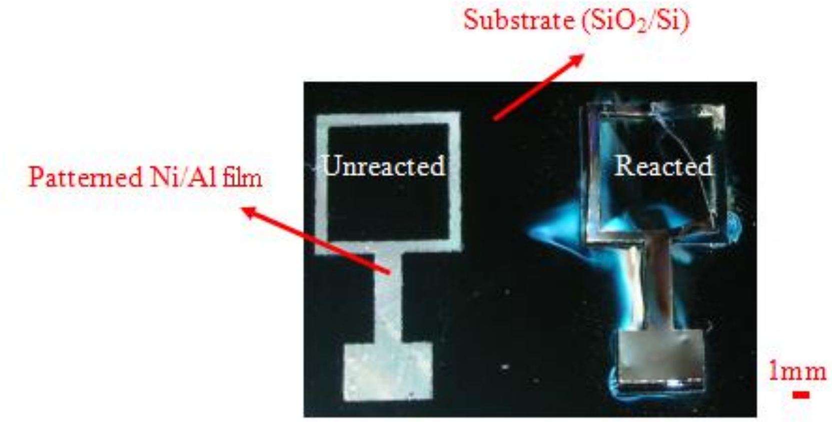

Figure 7.4 Patterned Ni/Al film (before and after reaction).

For hermetic packaging, solder is generally used as the bonding media due to its low permeability to gas and moisture. To effectively melt the solders, huge thickness of the reactive film is required. This will increase the deposition time. For the etching process, uniform pattern is difficult to achieve with thick films due to the prolonged immersion time in the corrosive solution. One alternative approach is using material pairs which possess higher heat of reaction. In this way, the same amount of heat can be generated with thinner films. One candidate worth paying attention to is CuO/Al multilayer (Petrantoni et al. 2010).

REFERENCES

Al-Hilli, S. M., M. Willander, A. Öst, P. Strålfors. 2007. ZnO nanorods as an intracellular sensor for *p*H measurements. *Journal of Applied Physics* 102(8): 084304.

Ashley, G. M., P. B. Kirby, T. P. Bulter, R. Whatmore, J. K. Luo. 2010. Chemically Sensitized Thin-Film Bulk Acoustic Wave Resonators as Humidity Sensors. *Journal of the Electrochemical Society* 157(12): J419-J424.

Baginski, T., S. Taliaferro, W. Fahey. 2001. Novel electroexplosive device incorporating a reactive laminated metallic bridge. *Journal of Propulsion and Power* 17(1): 184-189.

Barth, P. W. 1990. Silicon Fusion Bonding for Fabrication of Sensors, Actuators and Microstructures. *Sensors and Actuators A: Physical* 23(1-3): 919-926.

Benes, E. 1984. Improved Quartz Crystal Microbalance Technique. *Journal of Applied Physics* 56(3): 608-626.

Budraa, N. K., H. W. Jackson, M. Barmatz, W. T. Pike, J. D. Mai. 1999. Low pressure and low temperature hermetic wafer bonding using microwave heating. *Proceedings of IEEE International Conference on Micro Electromechanical Systems* 490-492.

Cao, A., M. Chiao, L. Lin. 2002. Selective and Localized Wafer Bonding Using Induction Heating. *Technical Digest Solid-State Sensors and Actuators Workshop* 153-156.

Cao, W. Q., Y. X. Duan. 2007. Current Status of Methods and Techniques for Breath Analysis. *Critical Reviews in Analytical Chemistry* 37(1): 3-13.

Chatterjee, A. P., P. Mitra, A. K. Mukhopadhyay. 1999. Chemically deposited zinc oxide thin film gas sensor. *Journal of Materials Science* 34(17): 4225-4231.

Cheng, W. H., W. J. Lee. 1999. Technology development in breath microanalysis for clinical diagnosis. *Journal of Laboratory and Clinical Medicine* 133(3): 218-228.

Cheng, Y. T., W. T. Hsu, K. Najafi, T. C. Nguyen, L. Lin. 2002. Vacuum Packaging Technology Using Localized Aluminum/Silicon-to-glass Bonding. *Journal of Microelectromechanical Systems* 11(5): 556-565.

Cheng, Y. T., L. Lin, K. Najafi. 2000. Localized Silicon Fusion and Eutectic Bonding for MEMS Fabrication and Packaging. *Journal of Microelectromechanical Systems* 9(1): 3-8.

Cheng, Y. T., L. Lin, K. Najafi. 2001. A Hermetic Glass-Silicon Package Formed Using Localized Aluminum/Silicon-Glass Bonding. *Journal of Microelectromechanical Systems* 10(3): 392-399.

Cheng, Y. T., L. Lin, K. Najafi. 2001. A Hermetic Glass-Silicon Package Formed Using Localized Aluminum/Silicon-Glass Bonding. *Journal of Microelectromechanical Systems* 10(3): 392-399.

Collins, R. J., D. G. Thomas. 1958. Photoconduction and Surface Effects with Zinc Oxide Crystals. *Physical Review* 112(2): 388-395.

Corso, C. D., A. Dickherber, W. D. Hunt. 2007. Lateral field excitation of thickness shear mode waves in a thin film ZnO solidly mounted resonator. *Journal of Applied Physics* 101(5): 054514.

Craig, R. G. 1993. *Restorative Dental Materials*. Philadelphia: Mosby.

Du, X. Y., Y. Q. Fu, S. C. Tan, J. K. Luo, A. J. Flewitt, W. I. Milne, D. S. Lee, N. M. Park, J. Park, Y. J. Choi, S. H. Kim, S. Maeng. 2008. ZnO film thickness effect on surface acoustic wave modes and acoustic streaming. *Applied Physics Letters* 93(9): 094105.

Duckham, A., S. J. Spey, J. Wang, M. E. Reiss, T. P. Weihs. 2004. Reactive nanostructured foil used as a heat source for joining titanium. *Journal of Applied Physics* 96(4): 2336-2342.

Eranna, G., B. C. Joshi, D. P. Runthala, R. P. Gupta. 2004. Oxide Materials for Development of Integrated Gas Sensors—A Comprehensive Review. *Critical Reviews in Solid State and Materials Sciences* 29(3&4): 111-188.

Faia, P. M., C. S. Furtado, A. J. Ferreira. 2004. Humidity sensing properties of a thick-film titania prepared by a slow spinning process. *Sensors and Actuators B: Chemical* 101(1-2): 183-190.

Feng, X. J., L. Feng, M. H. Jin, J. Zhai, L. Jiang, D. B. Zhu. 2004. Reversible Super-hydrophobicity to Super-hydrophilicity Transition of Aligned ZnO Nanorod Films. *Journal of the American Chemical Society* 126 (1): 62-63.

Fog, A., R. P. Buck. 1984. Electronic semiconducting oxides as *p*H sensors. *Sensors and Actuators* 5(2): 137-146.

Fulati, A., S. M. Usman Ali, M. H. Asif, N. H. Alvi, M. Willander, C. Brännmark, P. Strålfors, S. I. Börjesson, F. Elinder, B. Danielsson. 2010. An intracellular glucose biosensor based on nanoflake ZnO. *Sensors and Actuators B: Chemical* 150(2): 673-680.

Gavens, A. J., D. Van Heerden, A. B. Mann, M. E. Reiss, T. P. Weihs. 2000. Effect of intermixing on self-propagating exothermic reactions in Al/Ni nanolaminate foils. *Journal of Applied Physics* 87(3): 1255-1263.

Goyal, A., J. Cheong, S. Tadigadapa. 2004. Tin-based Solder Bonding for MEMS Fabrication and Packaging Applications. *Journal of Micromechanics and Microengineering* 14(6): 819-825.

Grudkowski, T. W., J. F. Black, T. M. Reeder, D. E. Cullen, R. A. Wagner. 1980. Fundamental - mode VHF/UHF minature acoustic resonators and filters on silicon. *Applied Physics Letters* 37(11): 993-995.

Gullberg, R. G., B. K. Logan. 2006. Results of a Proposed Breath Alcohol Proficiency Test Program. *Journal of Forensic Sciences* 51(1): 168-172.

Han, C., D. W. Hong, S. D. Han, J. Gwak, K. C. Singh. 2007. Catalytic combustion type hydrogen gas sensor using TiO_2 and UV-LED. *Sensors and Actuators B: Chemical* 125(1): 224-228.

Han, J., W. Gao. 2009. Surface Wettability of Nanostructured Zinc Oxide Films. *Journal of Electronic Materials* 38(4): 601-608.

Hanneborg, A., M. Nese, P. Ohlckers. 1991. Silicon-to-silicon Anodic Bonding with a Borosilicate Glass Layer. *Journal of Micromechanics and Microengineering* 1(3): 139-144.

Harendt, C., C. E. Hunt, W. Appel, H. Graf, B. Hofflinger, E. Penteker. 1991. Silicon on Insulator Material by Wafer Bonding. *Journal of Electronic Materials* 20(3): 267-277.

Huang, T., C. Ma. 2008. Characterization of Response of $ZnO/LiNbO_3$-Based Surface Acoustic Wave Delay Line Photodetector. *Japanese Journal of Applied Physics* 47(8): 6507-6512.

Huang, Y., Y. Chen, T. Wu. 2010. A passive wireless hydrogen surface acoustic wave sensor based on Pt-coated ZnO nanorods. *Nanotechnology* 21(9): 095503.

Jeong, I. S., J. H. Kim, S. Im. 2003. Ultraviolet-enhanced photodiode employing n-ZnO/p-Si structure. *Applied Physics Letters* 83(14): 2946-2948.

Jiang, D., J. Zhang, Y. Lu, K. Liu, D. Zhao, Z. Zhang, D. Shen, X. Fan. 2008. Ultraviolet Schottky detector based on epitaxial ZnO thin film. *Solid-State Electronics* 52(5): 679-682.

Johnston M. L., I. Kymissis, K. L. Shepard. 2010. FBAR-CMOS Oscillator Array for Mass-Sensing Applications. *Sensors Journal, IEEE* 10(6): 1042-1047.

Kim, H., K. Najafi. 2005. Characterization of Low-Temperature Wafer Bonding Using Thin-Film Parylene. *Journal of Microelectromechanical Systems* 14(6): 1347-1355.

Kim, J., B. Jeong, M. Chiao, L. Lin. 2009. Ultrasonic Bonding for MEMS Sealing and Packaging. *IEEE Transactions on Advanced Packaging* 32(2): 461-467.

Kim, K., P. Cho, S. Kim, J. Lee, C. Kang, J. Kim, S. Yoon. 2007. The selective detection of C_2H_5OH using SnO_2–ZnO thin film gas sensors prepared by combinatorial solution deposition. *Sensors and Actuators B: Chemical* 123(1): 318-324.

Knechtel, R., M. Wiemer, J. Fromel. 2006. Wafer Level Encapsulation of Microsystems Using Glass Frit Bonding. *Microsystem Technologies* 12(5): 468-472.

Korotchenkov, G., V. Brynzari, S. Dmitriev. 1999. Electrical behavior of SnO_2 thin films in humid atmosphere. *Sensors and Actuators B: Chemical* 54(3): 197-201.

Lakin, K. M., J. Belsick, J. F. McDonald, K. T. McCarron. 2001. Improved bulk wave resonator coupling coefficient for widebandwidth filters. *Proceedings of IEEE International Ultrasonics Symposium* 827-831.

Lakin, K. M., K. T. McCarron, R. E. Rose. 1995. Solidly Mounted Resonators and Filters. *Proceedings of IEEE International Ultrasonics Symposium* 905-908.

Law, J. B. K., J. T. L. Thong. 2006. Simple fabrication of a ZnO nanowire photodetector with a fast photoresponse time. *Applied Physics Letters* 88(13): 133114.

Li, Y., F. D. Valle, M. Simonnet, I. Yamada, J. J. Delaunay. 2009. Competitive surface effects of oxygen and water on UV photoresponse of ZnO nanowires. *Applied Physics Letters* 94(2): 023110.

Liao, Z. M., Y. Lu, J. Xu, J. M. Zhang, D. P. Yu. 2009. Temperature dependence of photoconductivity and persistent photoconductivity of single ZnO nanowires. *Applied Physics A: Materials Science & Processing* 95(3): 363-366.

Lin, A., E. S. Kim. 2009. Selectivity and Long-term Reliability of Resonant Explosive-Vapor-Trace Detection Based on Antigen-Antibody Binding. *Proceedings of IEEE International Conference on Micro Electromechanical Systems* 316-319.

Liu, H., L. Feng, J. Zhai, L. Jiang, D. B. Zhu. 2004. Reversible Wettability of a Chemical Vapor Deposition Prepared ZnO Film between Superhydrophobicity and Superhydrophilicity. *Langmuir* 20(14): 5659-5661.

Lord, H., F. Y. Yu, A. Segal, J. Pawliszyn. 2002. Breath Analysis and Monitoring by Membrane Extraction with Sorbent Interface. *Analytical Chemistry* 74(21): 5650-5657.

Lu, C. S., O. Lewis. 1972. Investigation of Film-thickness Determination by Oscillating Quartz Resonators with Large Mass Load. *Journal of Applied Physics* 43(11): 4385-4390.

Luo, C., L. Lin. 2002. The application of nanosecond-pulsed laser welding technology in MEMS packaging with a shadow mask. *Sensors and Actuators A: Physical* 97–98(1): 398-404.

Martin, S. J., V. E. Granstaff, G. C. Frye. 1991. Characterization of a Quartz Crystal Microbalance with Simultaneous Mass and Liquid Loading. *Analytical Chemistry* 63(20): 2272-2281.

Martines, R., E. Fortunato, P. Nunes, I. Ferreira, A. Marques, M. Bender, N. Katsarakis, V. Cimalla, G. Kiriakidis. 2004. Zinc oxide as an ozone sensor. *Journal of Applied Physics* 96(3): 1398-1408.

Maszara, W. P., G. Goetz, A. Caviglia, J. B. McKittereck. 1988. Bonding of Silicon Wafers for Silicon on Insulator. *Journal of Applied Physics* 64(10): 4943-4950.

Mei, Y., G. R. Lahiji, K. Najafi. 2002. A Robust Gold-Silicon Eutectic Wafer Bonding Technology for Vacuum Packaging. *Technical Digest Solid-State Sensors and Actuators Workshop* 772-774.

Melnick, D. A. 1957. Zinc Oxide Photoconduction, an Oxygen Absorption Process. *Journal of Chemical Physics* 26(5): 1136-1146.

Miyauchi, M., A. Shimai, Y. Tsuru. 2005. Photoinduced Hydrophilicity of Heteroepitaxially Grown ZnO Thin Films. *Journal of Physical Chemistry B* 109(27): 13307-13311.

Mukhopadhyay, R. 2004. Don't Waste Your Breath. *Analytical Chemistry* 76(15): 273A–276A.

Nakamura, K., H. Sasaki, H. Shimizu. 1981. A piezoelectric composite resonator consisting of a ZnO film on an anisotropically etched silicon substrate. *Japanese Journal of Applied Physics* 20 (2): L111-L113.

Nomura, T., R. Takebayashi, A. Saitoh. 1998. Chemical Sensor Based on Surface Acoustic Wave Resonator Using Langmuir-Blodgett Film. *IEEE Transactions on Ultrasonics, Ferroelectrics, and Frequency Control* 45(5): 1261-1265.

Pang, W., H. Yu, H. Zhang, E. S. Kim. 2005. Temperature-compensated film bulk acoustic resonator above 2 GHz. *IEEE Electron Device Letters* 26(6): 369-371.

Pang, W., H. Zhang, E. S. Kim. 2005. Micromachined acoustic wave resonator isolated from substrate. *IEEE Transactions on Ultrasonics, Ferroelectrics, and Frequency Control* 52(8): 1239-1246.

Penza, M., G. Cassano. 2000. Relative humidity sensing by PVA-coated dual resonator SAW oscillator. *Sensors and Actuators B: Chemical* 68(1-3): 300-306.

Petrantoni, M., C. Rossi, L. Salvagnac, V. Conédéra, A. Estève, C. Tenailleau, P. Alphonse, Y. J. Chabal. 2010. Multilayered Al/CuO thermite formation by reactive magnetron sputtering: Nano versus micro. *Journal of Applied Physics* 108(8): 084323.

Pezous, H., C. Rossi, M. Sanchez, F. Mathieu, X. Dollat, S. Charlot, V. Conedera. 2010. Fabrication, assembly and tests of a MEMS-based safe, arm and fire device. *Journal of Physics and Chemistry of Solids* 71(2): 75-79.

Pinelis, M. "TriQuint's MEMS revenues grow to $74.7 million in 2010". MEMS Investor Journal. http://www.memsinvestorjournal.com/2011/02/triquints-mems-revenues-grow-to-747-million-in-2010.html.

Qiu, X. 2009. *Reactive Multilayer Foils: Fabrication, Characterization, Applications.* Saarbrücken: VDM.

Qiu, X., J. Oiler, J. Zhu, Z. Wang, R. Tang, C. Yu, H. Yu. 2010. Film Bulk Acoustic-Wave Resonator Based Relative Humidity Sensor Using ZnO Films. *Electrochemical and Solid-State Letters* 13(5): J65-J67.

Qiu, X., J. Wang. 2008. Bonding silicon wafers with reactive multilayer foils. *Sensors and Actuators A: Physical* 141(2): 476-481.

Qiu, X., Z. Wang, J. Zhu, J. Oiler, R. Tang, C. Yu, H. Yu. 2010. The Effects of Relative Humidity and Reducing Gases on the Temperature Coefficient of Resonant Frequency of ZnO Based Film Bulk Acoustic-wave Resonator. *IEEE Transactions on Ultrasonics, Ferroelectrics, and Frequency Control* 57(9): 1902-1904.

Qiu, X., J. Zhu, J. Oiler, C. Yu, Z. Wang, H. Yu. 2009. Film bulk acoustic-wave resonator based ultraviolet sensor. *Applied Physics Letters* 94(15): 151917.

Qiu, X., J. Zhu, J. Oiler, C. Yu, Z. Wang, H. Yu. 2009. Localized Parylene-C bonding with reactive multilayer foils. *Journal of Physics D: Applied Physics* 42(18): 185411.

Rayleigh, L. 1885. On Waves Propagated along the Plane Surface of an Elastic Solid. *Proceedings London Mathematical Society* 17(1): 4-11.

Righettoni, M., A. Tricoli, S. E. Pratsinis. 2010. Si:WO_3 Sensors for Highly Selective Detection of Acetone for Easy Diagnosis of Diabetes by Breath Analysis. *Analytical Chemistry* 82(9): 3581-3587.

Rittersma, Z. M. 2002. Recent achievements in miniaturised humidity sensors—a review of transduction techniques. *Sensors and Actuators A: Physical* 96(2-3): 196-210.

Rossi, C., T. Do Conto, D. Esteve, B. Larangot, S. Orieux. 2001. Design, fabrication and modelling of MEMS-based microthrusters for space application. *Smart Materials and Structures* 10(6): 1156-1162.

Ruby, R., K. Hashimoto. 2009. *RF Bulk Acoustic Wave Filters for Communications.* Norwood: Artech House.

Ruby, R., P. Merchant. 1994. Micromachined Thin Film Bulk Acoustic Resonators. *Proceedings of IEEE International Ultrasonics Symposium* 135-138.

Sahay, P. P. 2005. Zinc oxide thin film gas sensor for detection of acetone. *Journal of Materials Science* 40(16): 4383-4385.

Sahay, P. P., S. Tewari, S. Jha, M. Shamsuddin. 2005. Sprayed ZnO thin films for ethanol sensors. *Journal of Materials Science* 40(18): 4791-4793.

Sanchez, J. M., R. D. Sacks. 2003. GC Analysis of Human Breath with A Series-Coupled Column Ensemble and A Multibed Sorption Trap. *Analytical Chemistry* 75(10): 2231-2236.

Sankaranarayanan, S., R. Singh, V. Bhethanabotla. 2010. Acoustic streaming induced elimination of nonspecifically bound proteins from a surface acoustic wave biosensor: Mechanism prediction using fluid-structure interaction models. *Journal of Applied Physics* 108(10): 104507.

Sarvar, F., D. A. Hunt, D. C. Whalley. 2002. Application of Adhesives in MEMS and MOEMS Assembly: A Review. *Proceedings of IEEE Polytronic Conference* 22-28.

Scholz, G. 1992. Marktanalyse: Sensoren und Meßgeräte für Gasfeuchte. *Technisches Messen* 59(3): 88-109.

Sharma, P., S. Kumar, K. Sreenivas. 2003. Interaction of surface acoustic waves and ultraviolet light in ZnO films. *Journal of Materials Research* 18(3): 545-548.

Sharma, P., K. Sreenivas. 2003. Highly sensitive ultraviolet detector based on ZnO/$LiNbO_3$ hybrid surface acoustic wave filter. *Applied Physics Letters* 83(17): 3617-3619.

Shuk, P., K. V. Ramanujachary. 1996. New metal-oxide-type *p*H sensors. *Solid State Ionics* 86-88(2): 1115-1120.

Smith, D., P. Spanel. 2005. Selected ion flow tube mass spectrometry (SIFT-MS) for on-line trace gas analysis. *Mass Spectrometry Reviews* 24(5): 661-700.

Sparks, D., G. Queen, R. Weston, G. Woodward, M. Putty, L. Jordan, S. Zarabadi, K. Jayakar. 2001. Wafer-to-wafer Bonding of Nonplanarized MEMS Surfaces Using Solder. *Journal of Micromechanics and Microengineering* 11(6): 630-634.

Sun, R., A. Nakajima, A. Fujishima, T. Watanabe, K. Hashimoto. 2001. Photoinduced Surface Wettability Conversion of ZnO and TiO_2 Thin Films. *Journal of Physical Chemistry B* 105(10): 1984-1990.

Suzuki, Y., Y. C. Tai. 2006. Micromachined High-Aspect-Ratio Parylene Spring and Its Application to Low-Frequency Accelerometers. *Journal of Microelectromechanical Systems* 15(5): 1364-1370.

Swiston, A. J., T. C. Hufnagel, T. P. Weihs. 2003. Joining bulk metallic glass using reactive multilayer foils. *Scripta Materialia* 48(12): 1575-1580.

Takahashi, Y., M. Kanamori, A. Kondoh, H. Minoura, Y. Ohya. 1994. Photoconductivity of Ultrathin Zinc Oxide Films. *Japanese Journal of Applied Physics* 33(12A): 6611-6615.

Takata, M., D. Tsubone, H. Yanagida. 1976. Dependence of electrical conductivity of ZnO on degree of sintering. *Journal of the American Ceramic Society* 59(1-2): 4-8.

Taklo, M. M. V., P. Storas, K. Schjolberg-Henriksen, H. K. Hasting, H. Jakobsen. 2004. Strong, High-yield and Low-temperature Thermocompression Silicon Wafer-level Bonding with Gold. *Journal of Micromechanics and Microengineering* 14(7): 884-890.

Toda, K., J. Li, P. K. Dasgupta. 2006. Measurement of Ammonia in Human Breath with a Liquid-Film Conductivity Sensor. *Analytical Chemistry* 78(20): 7284-7291.

Wallis, G., D. I. Pomerantz. 1969. Field Assisted Glass-Metal Sealing. *Journal of Applied Physics* 40(10): 3946-3949.

Wang, J., E. Besnoin, A. Duckham, S. J. Spey, M. Reiss, O. M. Knio, M. Powers, M. Whitener, T. P. Weihs. 2003. Room-temperature soldering with nanostructured foils. *Applied Physics Letters* 83(19): 3987-3989.

Wang, J., E. Besnoin, A. Duckham, S. J. Spey, M. E. Reiss, O. M. Knio, T. P. Weihs. 2004. Joining of stainless-steel specimens with nanostructured Al/Ni foils. *Journal of Applied Physics* 95(1): 248-256.

Wang, J., E. Besnoin, O. M. Knio, T. P. Weihs. 2004. Investigating the effect of applied pressure on reactive multilayer foil joining. *Acta Materialia* 52(18): 5265-5274.

Wang, J., E. Besnoin, O. M. Knio, T. P. Weihs. 2005. Effects of physical properties of components on reactive nanolayer joining. *Journal of Applied Physics* 97(11): 114307.

Wang, J., K. M. Lakin. 1981. Sputtered AlN Films for Bulk Acoustic Wave Devices. *Proceedings of IEEE International Ultrasonics Symposium* 502-505.

Wang, Z., X. Qiu, S. Chen, W. Pang, H. Zhang, J. Shi, H. Yu. 2011. ZnO based film bulk acoustic resonator as infrared sensor. *Thin Solid Films* in press.

Wathen, A. D., F. Munir, W. D. Hunt. 2009. A high-*Q* hybrid acoustic mode in thin film ZnO solidly mounted resonators. *Applied Physics Letters* 95(12): 123509.

Weichel, S., R. Reus, M. Lindahl. 1998. Silicon-to-silicon Anodic Wafer Bonding Using Evaporated Glass. *Sensors and Actuators A: Physical* 70(1-2): 179-184.

Wen, C., C. Zhu, Y. Ju, H. Xu, Y. Qiu. 2010. A novel NO_2 gas sensor using dual track SAW device. *Sensors and Actuators A: Physical* 159(2): 168-173.

Wenzel, S. W., R. M. White. 1989. Analytic Comparison of the Sensitivities of Bulk-wave, Surface-wave and Flexural Plate-wave Ultrasonic Gravimetric Sensors. *Applied Physics Letters* 54(20): 1976-1978.

Wixforth, A., J. Kotthaus, G. Weimann. 1989. Surface acoustic waves on GaAs/Al_xGa_{1-x}As heterostructures. *Physical Review B* 40(11): 7874-7887.

Wu, T., W. Wang. 2004. An experimental study on the ZnO/sapphire layered surface acoustic wave device. *Journal of Applied Physics* 96(9): 5249-5253.

Xu, B., W. Zhang. 2010. Modification of vertically aligned carbon nanotubes with RuO_2 for a solid-state *p*H sensor. *Electrochimica Acta* 55(8): 2859-2864.

Xu, Q. A., J. W. Zhang, K. R. Ju, X. D. Yang, X. Hou. 2006. ZnO thin film photoconductive ultraviolet detector with fast photoresponse. *Journal of Crystal Growth* 289(1): 44-47.

Yamazoe, N., K. Shimanoe. 2008. Theory of power laws for semiconductor gas sensors. *Sensors and Actuators B: Chemical* 128(2): 566-573.

Yan, Z., X. Y. Zhou, G. K. H. Pang, T. Zhang, W. L. Liu, J. G. Cheng, Z. T. Song, S. L. Feng, L. H. Lai, J. Z. Chen, Y. Wang. 2007. ZnO-based film bulk acoustic resonator for high sensitivity biosensor applications. *Applied Physics Letters* 90(14): 143503.

Yang, H., M. Wu, W. Fang. 2005. Localized Induction Heating Solder Bonding for Wafer Level MEMS Packaging. *Journal of Micromechanics and Microengineering* 15(2): 394-399.

Yu, H., L. Ai, M. Rouhanizadeh, D. Patel, E. S. Kim, T. K. Hsiai. 2008. Flexible Polymer Sensors for In Vivo Intravascular Shear Stress Analysis. *Journal of Microelectromechanical Systems* 17(5): 1178-1186.

Zhang, C., F. Feng, S. Sui. 1998. A New Approach to the Development of Quartz Crystal Sensors Distinguishing Between Mass Loading and Liquid Damping. *IEEE Transacations on Instrumentation and Measurement* 47(5): 1234-1238.

Zhang, H., E. S. Kim. 2005. Micromachined Acoustic Resonant Mass Sensor. *Journal of Microelectromechanical Systems* 14(4): 699-706.

Zhang, K., S. Chou, S. Ang, X. Tang. 2005. A MEMS-based solid propellant microthruster with Au/Ti igniter. *Sensors and Actuators A: Physical* 122(1): 113-123.

Zhang, K., C. Rossi, M. Petrantoni, N. Mauran. 2008. A Nano Initiator Realized by Integrating Al/CuO-Based Nanoenergetic Materials With a Au/Pt/Cr Microheater. *Journal of Microelectromechanical Systems* 17(4): 832-836.

Zhao, R., M. Xu, J. Wang, G. Chen. 2010. A *p*H sensor based on the TiO_2 nanotube array modified Ti electrode. *Electrochimica Acta* 55(20): 5647-5651.

Zhou, J., Y. Gu, Y. Hu, W. Mai, P. H. Yeh, G. Bao, A. K. Sood, D. L. Polla, Z. L. Wang. 2009. Gigantic enhancement in response and reset time of ZnO UV nanosensor by utilizing Schottky contact and surface functionalization. *Applied Physics Letters* 94(19): 191103.